Ultra-Deep Reactive Ion Etching for Silicon Wankel Internal Combustion Engines

by

Aaron Jay Knobloch

B. S. (Bucknell University) 1998
M. S. (University of California, Berkeley) 2001

A dissertation submitted in partial satisfaction

of the requirements for the degree of

Doctor of Philosophy

in

Engineering – Mechanical Engineering

in the

GRADUATE DIVISION

of the

UNIVERSITY OF CALIFORNIA, BERKELEY

Committee in Charge:

Professor Albert P. Pisano, Chair
Professor A. Carlos Fernandez-Pello
Professor Seth Sanders

Fall, 2003

ProQuest Information and Learning Company
300 North Zeeb Road
P.O. Box 1346
Ann Arbor, MI 48106-1346

Ultra-Deep Reactive Ion Etching for Silicon Wankel Internal Combustion Engines

by

Aaron Jay Knobloch

The dissertation of Aaron Jay Knobloch is approved:

Chair Date

Date

Date

University of California, Berkeley

Fall 2003

Abstract

Ultra-Deep Reactive Ion Etching for Silicon Wankel Internal Combustion Engines

by

Aaron Jay Knobloch

Doctor of Philosophy in Mechanical Engineering

University of California, Berkeley

Professor Albert P. Pisano, Chair

A new process is presented for the development of a micro, internal-combustion engine fabricated in a process that achieves 900 μm deep features via deep reactive ion etching (DRIE). A single-sided 900 μm ultra-deep etch process with high mask selectivity is used to generate straight sidewall structures with low sidewall roughness. This research is part of an effort to create an autonomous, portable MEMS-based Rotary Engine Power System (MEMS REPS) capable of producing power on the order of milliwatts with an energy density substantially better than that of a conventional battery. Based on the Wankel-type rotary engine, the design of a 2.4 mm silicon prototype features a planar geometry and self-valving operation and has a displacement of 1.18 mm^3.

The engine consists of four basic components: rotor, epitrochoid housing, spur gear plate, and square shaft. The rotor features 25 μm wide in-plane cantilever beams, electrodeposited NiFe soft magnetic material used for an integrated electrical generator, and highly accurate annular gear teeth used to control the motion of the rotor within the epitrochoid housing. The rotor and epitrochoid housing are co-fabricated in a highly selective and accurate deep reactive ion etching (DRIE) process which produced 900 μm thick MEMS features. Selectivity of this process exceeds 350:1 for low temperature deposited oxide and 150:1 for SPR220 thick resist. This process also features 250 μm wide trenches with a variation of only 6 μm on each side and low sidewall roughness to prevent leakage around the apex seal. While "black silicon" or grass is developed due to the high process pressures of this etch, the grass does not remain in the areas etched entirely through the wafer. Severe undercutting of the apex seals was found to be the result of aspect ratio dependent etch (ARDE) and poor mask design. A modified process is presented which partially eliminates the effect of ARDE on the apex seal trenches. However, work is still necessary to develop a design which prevents the lateral etching of the apex seal tip.

Vertical, accurate spur gear teeth are produced using a low pressure DRIE process. The low pressure DRIE process creates surfaces with an RMS roughness in excess of 4.4 nm as compared to an unetched silicon wafer (3-4 nm). The superior roughness of the trench is important for forming a pre-bond between the epitrochoid housing and the spur gear plate for engine assembly. Silicon square shafts were also microfabricated for use in the engine. A square shaft design is advantageous for MEMS fabrication because the shafts can be fabricated in the plane of the wafer which results in more accurate components. Finally, partial assembly of the engine was realized through the use of a Suss Microtec flip chip bonder. Avenues of optimization for the engine fabrication process are discussed.

Professor Albert P. Pisano Date
Chair, Dissertation Committee

Table of Contents

List of Figures

List of Tables

Nomenclature

a	Epitrochoid offset
A	Channel cross-sectional area
B_{PM}	Strength of the permanent magnet
d	Pitch diameter
D	Displacement
D_c	Diffusion coefficient
e	Rotor eccentricity
E_i	Young's modulus, inner material
E_o	Young's modulus, outer material
f	Actual mass ratio of fuel to air
f_s	Stoichiometric ratio of fuel to air
H	Channel height
k	Ratio of specific heats
l	Characteristic length scale of the engine
L	Channel length
L_w	Trench width at widest point
L_m	Trench width at mask level
LHV	Lower heating value
$\dot{m}_{fuel}$	Mass flow rate of fuel
P_c	Contact pressure
P_{gen}	Power output of the generator
P_{mech}	Mechanical power output of the engine
R	Rotor generating radius
R	Radial Location
R_a	Average Roughness
R_{coil}	Resistance of the coil
R_i	Inner radius
R_o	Outer radius
R_q	Root mean squared
R_t	Ten point height difference
R_z	Maximum height difference
t	Thickness of the engine
t_a	Available time for diffusion
t_d	Diffusion time
T	Temperature
u	Velocity of the rotor
v_i	Poisson's ratio, inner material
v_o	Poisson's ratio, outer material
w	Rotor width
x	x-coordinate
y	y-coordinate

GREEK

α	Angular location
α_i	Coefficient of thermal expansion
δ	Interference
ε_{th}	Theoretical compression ratio
η_{th}	Thermal efficiency
η_{gen}	Generator efficiency
θ	Angle
θ_c	Contact angle
σ_r	Radial stress
σ_t	Tangential stress
τ_{gen}	Torque capacity of the generator
τ_{mech}	Mechanical torque output of the engine
Φ	Equivalence ratio
ϕ	Volumetric fuel to air ratio
ω	Engine Speed

Acknowledgements

After five years of hard work and effort, one of the most important things you gain from the PhD experience is what you learn about yourself in addition to what I have learned from my research. I want these acknowledgements to reflect those who helped me outside as well inside the laboratory. My first thoughts go to my co-advisor, Professor Carlos Ferandez-Pello, for allowing me to be involved in this research area and believing in me during some of the rough times when I joined his group. I had a hard time acclimating to life at Berkeley both inside and outside the classroom. However, Professor Pello kept my spirits and confidence high while at the same time asking me to push myself more. I would also thank my advisor Professor Albert P. Pisano for providing the vision necessary to keep our project going and for personally, pushing me to become a better writer and speaker. In addition, I would like to thank Professor Seth Sanders and Professor Dorian Liepmann for serving me on my PhD and Masters thesis committees respectively.

The funding for my work would not be possible without the faith and contributions from the Defense Advanced Research Projects Agency under grant numbers DABT63-98-0016 and NBCH010060.

The completion of the work in the following pages would not be possible without the contribution of the group of people who worked with me on both the MEMS RICE and MEMS REPS projects. First, I would like to thank Dr. Kelvin Fu who pushed me to work harder and constant source of input. Dr. Fu had the patience enough to train me in the microlab even when I broke his wafers. I would also like to thank Dr. David Walther who did all the little things that allowed me to pursue my research unfettered. I would

like to thank Fabian Martinez, Matt Senesky, and Debbie Jones for contributing their designs to my processes and giving me the input from their analyses which helped guide my designs. I would also like to thank the rest of the graduate students who worked on MEMS REPS and MEMS RICE team for their input in my research and their support throughout my time at Berkeley: Bryan Cooley, Bill Lindsay, Brenda Haendler, Josh Heppner, Bennett Sprague, Dr. Chen Li Sun, John Dirner, Dr. Conrad Stoldt, Jack Yu, Perry Tsao, and Dr. Muthu Wijesundara. In addition, there were many contributions from undergraduates in our laboratory including Miki Yamada and Hyun Jin In.

At UC-Berkeley, I was very lucky to be supported by such people as Maryanne Peters, Scott McCormick, Michael Neufer, John Austin, and the staff of the mechanical engineering department. The MEMS REPS project itself would not be possible without the support of the Berkeley Sensor and Actuator Center including Tom Parsons, Helen Kim, John Huggins, and Bill Flounders. I would like to especially thank Matt Wasilik who taught me everything I know about lithography and DRIE. Special thanks are necessary for Professors Kenji Miyasaka and Kaoru Maruta for spending time visiting our lab pushing this project in the early years.

There were many more people beyond those who worked with me on my research who deserve recognition. These include my labmates: Mark Roslon, Andreja Stevanovic, Shivani Mehta, Mark Mikofski, David Rich, Jeremy Frank, Eric Hobbes, Julian Lippmann, and Alex Papavasiliou. I would also like to thank the staff and community of the microlab including Evan Stateler for maintaining the STS on a sometimes daily basis.

I would finally like to thank the support of my family and friends without whom I would not be in California today. I would like to thank Scott Huxtable for paving the way for Bucknellians at Cal-Berkeley and convincing me that I should pursue graduate school. Finally, I would to thank Audrey for having the faith in me to move to Berkeley and who has been my constant supporter every day since.

1. Introduction

It is evident that portable electronic devices such as cellular phones, mp3 players, PDAs, and laptop computers are becoming a ubiquitous part of today's mobile society. This revolution in portable electronics is increasing the demands put on battery performance despite the continuing progress in lower power electronics. Batteries must last longer and weigh less in order to keep pace with society's demands. In order to increase performance, batteries are relying on unique materials and processes which can be environmentally damaging with limited gains in energy density. However, a method of power generation utilizing chemical reactions from combustion would yield a higher energy density than the best performing battery. This advance would lead to both an increase in the lifetime and a reduction in the weight of portable electronic devices.

1.1 Motivation

The primary advantages and disadvantages of batteries lie in the maturity of the technology. Initially known as Voltaic piles, batteries were invented in 1800 by

Alessandro Volta when he discovered that electricity could be generated by reactions between dissimilar metals. The first batteries consisted of a series of two types of metal disks (zinc and copper) separated by either salt water or acid soaked cardboard slabs. Since then batteries have become a low cost, high volume product. Batteries are generally separated into two categories: primary batteries, which are used only once, and secondary batteries, which can be recharged for multiple uses. In comparison to the battery, a liquid hydrocarbon fuel such as Octane possesses a specific energy density of 12340 W-hr/kg which is 60 times that of the best secondary batteries and 17 times that of state of the art primary batteries. Figure 1-1 shows a comparison between various types of commonly used batteries and a motor-generator set fueled with a liquid hydrocarbon. On the other hand, battery materials compare much more favorably to liquid hydrocarbons when looking at specific density. For example, octane only has a volumetric energy density 6 times that of secondary batteries and equal to or less than that of some primary batteries such as Thionyl Chloride Lithium [1-4]. When comparing liquid hydrocarbon fuels to commercial batteries, it is important to consider efficiency in the conversion of the chemical potential energy of the fuel to electrical energy. For an automobile engine, the efficiency in the conversion of chemical energy of the fuel to mechanical energy or torque is typically between 20-30%. Losses may also arise in the conversion of the mechanical torque generated by combustion to electrical energy. If the overall energy conversion efficiency from combustion to mechanical work to electrical power generation were only as great as 10%, a hydrocarbon-fueled internal combustion engine and generator set would still have a specific power density 10 times greater than secondary batteries and 3 times greater than a primary battery.

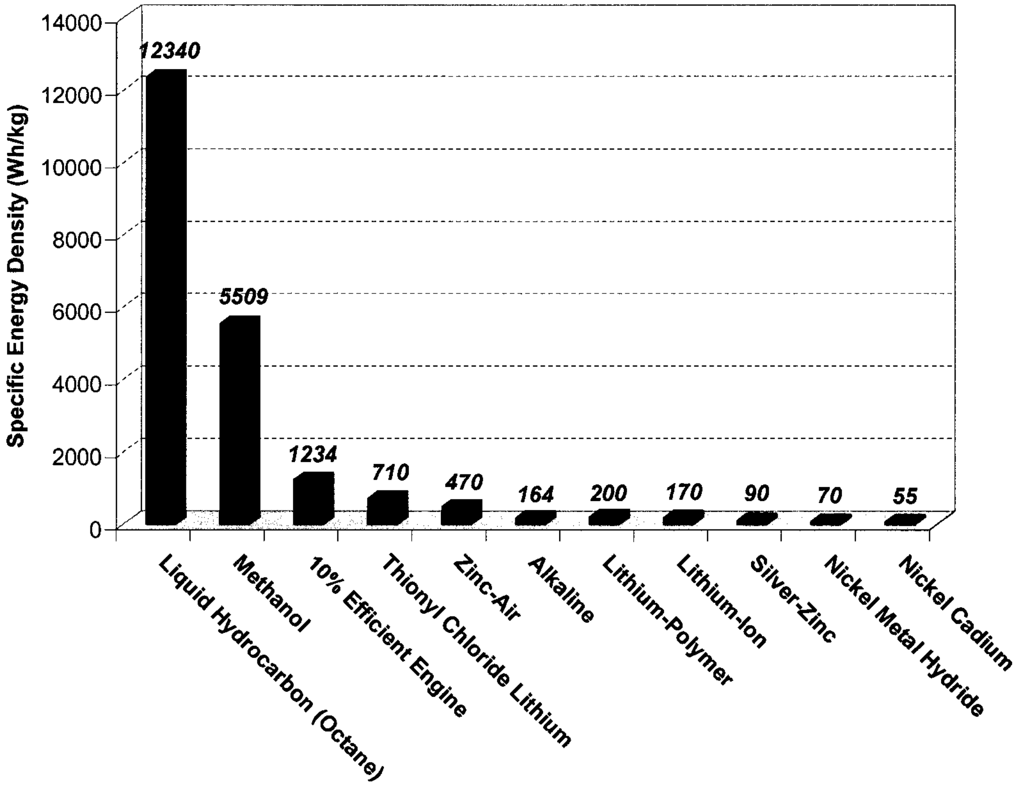

Figure 1-1. Energy density comparison between primary and secondary batteries and liquid hydrocarbon fuels [1-4].

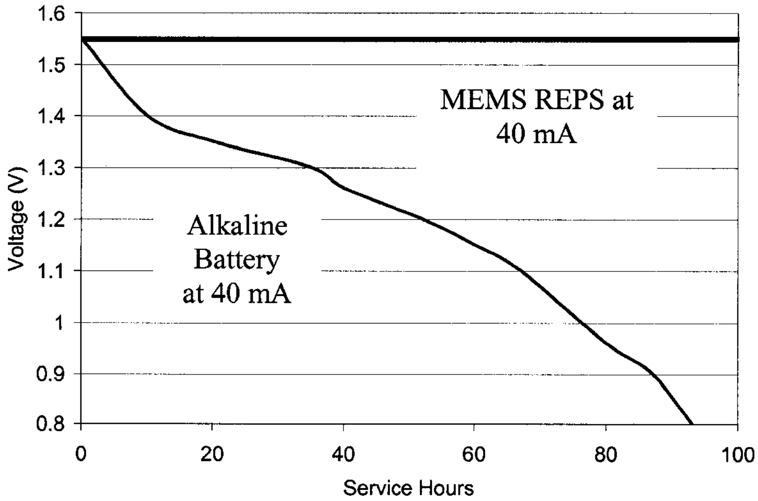

Figure 1-2. MEMS REPS electrical output contrasted with that of a battery [5].

In addition to advantages in specific power to weight ratio, an internal combustion engine is a more flexible power source for a variety of applications. This is evident when looking at voltage output for a constant current draw over the lifetime of a battery as shown in Figure 1-2 [5]. The voltage output declines over battery lifetime which affects the performance of the device being powered. Typically, the total amount of energy stored in the battery is not entirely drained because the voltage output of the battery will drop below the voltage necessary for the device's operation. By varying the speed of the engine or the mixture of the fuel, an engine can provide a wide range of power outputs without degradation in the current supplied to the system. The power of the engine output can then be tuned to the power demands and duty cycle of the application.

Batteries are also a source for environmental concern in terms of disposal. Large scale recycling efforts such as those pursued in Japan have not been successful especially in regards to secondary batteries [6]. For the consumer, the recycling process can be very confusing both due to the multitude of materials (In, Zn, Mn, Li, Ni, Pb, or Hg) used for the battery electrodes as well as the need for each material to be recycled separately [7]. The recycling process is also quite expensive and batteries manufactured with recycled metals do not perform as well as those made from previously unused metal. Batteries can rupture when used improperly, they can explode in a fire, and new environmental regulations stemming from the materials used in batteries could restrict improvements in battery performance.

An internal combustion engine is not without its own environmental concerns, however. In large-scale engines, pollutants such as unburned hydrocarbons, NO_x, CO, and CO_2 have demonstrated deleterious effects on the environment. As engine size is scaled down, the mass flow rate of fuel will be reduced which will result in a corresponding drop in the amount of effluent emitted. It appears that catalytic converters can take advantage of the increased surface-area to volume ratio to remove unburned hydrocarbons and carbon monoxide from the effluent. The reaction which produces NO is only fast at high temperatures. This is due to the high activation energy of the triple bonded N_2 molecule which reacts with Oxygen radicals to generate NO. For a lean or stoichometric burning engine, if the amount of time spent at high temperature is minimized, the combustion products will not spend a sufficient time at an elevated temperature (1500 K) to generate NO thru the thermal mechanism. For a Wankel engine operating at 40000 RPM, the fuel and air mixture will only spend 375 μsec in the engine after ignition takes place. Due to this high operating speed, the residence time is much smaller than the equilibrium time for the thermal NO mechanism which is typically a few milliseconds at high temperatures [8]. Even assuming a worst-case scenario of complete fuel and air conversion to CO_2 and H_2O, the CO_2 production of a micro-engine is minimal when compared to the CO_2 output of human. Typically, 5% of the average human lung output is composed of CO_2. In comparison, the CO_2 output of a combustion based engine with a displacement of 1.2 mm^3 would at least be more than 30 times less than that of an average human [9].

1.2 Background

1.2.1 Small-scale Combustion

Previous and ongoing research in micro-combustion has laid the foundation for the development of a millimeter scale internal combustion engine. Fundamentally combustion on the small scale is limited by an effect called quenching. Flame quenching occurs when heat losses from the combustion reaction exceed the heat generated by that reaction or radical recombination with the wall terminates the combustion reactions. This ultimately leads to the extinguishment of the flame. Quenching is a direct result of the increased surface area to volume ratio as a combustion chamber is reduced in size. Table 1-1 shows the quenching distance for a variety of fuels at standard temperature and pressure [10]. Quenching distance is experimentally measured by examining a stabilized flame on either a tube or slit. The tube method examines a stabilized flame above a tube where the fuel and air mixture is rapidly shut off. If the flame propagates back through the tube (flashback), the tube is larger than the quenching distance. Otherwise, the flame will extinguish and the tube is smaller than the quenching distance. The slit method uses the same principles with a rectangular slit geometry where the quenching distance is width of the slit. Generally, the rectangular slit configuration gives a smaller quenching distance than that of the tube [10].

	Quench Distance $\Phi=1$ (mm)
Acetylene	2.3
Ethane	2.3
Hydrogen	0.64
Methane	2.5
Methanol	1.8
Propane	20

Table 1-1. Quenching distance of various common fuels at STP [4].

Until recently, quenching measurements using tubes and slits were regarded as the fundamental limit on the scale of combustion. However, research by Cooley showed that increasing wall temperature and therefore, reducing the heat losses can have a dramatic impact on quenching distance [11]. By burning methane within various size quartz tubes, it was shown that the quenching distance for methane could be reduced 2.5 times to below 1 mm by limiting the heat losses. Three different methods were explored to reduce heat losses from a flame. First, a nichrome heating wire was used to externally heat the walls of the quartz tubes. This method is useful for quantitatively measuring the heat input to sustain combustion but is impractical for small-scale power generation since the power needed to externally heat the combustion chamber would reduce the power output of the device. A more practical solution is to flow the hot exhaust gases from the combustion reaction over the outside walls of the tube. Another method used to increase the temperature of the walls was to bunch tubes together in a bundle. Combustion in the outer tubes act to insulate the inner tubes thru adiabatic surfaces. This method would be analogous to grouping a set of engines together for increased power output and improved performance due to adiabatic surfaces.

1.2.2 MEMS

In order to develop small scale portable power generation based on a Wankel engine, technology for the precise fabrication of small scale engine components must be available. One such technology is MicroElectromechanical Systems (MEMS) which is a growing field where mechanical elements are manufactured leveraging the techniques developed in the integrated circuit community. Devices currently utilizing MEMS technology include gyroscopes for Global Positioning Systems, accelerometers used in air bag sensors, and inkjet spray nozzles. One of the primary advantages in making small mechanical devices utilizing MEMS is the potential lower per-unit cost of a device from batch fabrication methods. In recent years, new fabrication techniques combined with new materials have opened the door for MEMS-scale thermal-fluid devices to become practical [12]. In addition, work centering on microfluidics has led to the design and fabrication of MEMS valves, pumps, heat exchanges, and micro-mixers. Combustion-related MEMS devices are inherently microfluidic and depend upon some combination MEMS-based sensors, actuators, and microfluidic devices for its operation. Although the MEMS field is a diverse and growing entity, the processes and devices have been limited to planar geometries with limited aspect ratios.

1.2.3 Wankel Engine

A variety of methods for the conversion of the chemical energy of a fuel to mechanical or electrical power are being explored for an autonomous micro-power generation system [13]. However, the methods of energy conversion must be judged in comparison with the battery. Thermoelectrics or photovoltaics do not have a significant advantage in energy density when compared to a battery due to their poor conversion efficiency [13]. While not a combustion device, fuel cells have shown high conversion efficiencies utilizing hydrogen fuel. However, reliable conversion of liquid hydrocarbon fuels to Hydrogen using a reformer must be developed to overcome the storage volatility of Hydrogen in order to compete with the energy density of a battery.

In contrast, the relatively high efficiency of an internal combustion engine gives it the potential to significantly eclipse the energy density of a battery. However, piston-cylinder engine typical of most automobiles do not conform conveniently to the limits of the planar fabrication processes used in MEMS fabrication. One potential design which has a planar geometry is a rotary internal combustion engine such as the Wankel design.

A Wankel engine operates by turning a "triangular" rotor inside an epitrochoidal housing. Typically, a Wankel engine does not use discrete valves to control the flow of intake and exhaust but rather, the sweeping of the rotor by the intake and exhaust ports controls the flow of fuel and air into the engine. The design of the Wankel also utilizes few moving parts. Figure 1-3 shows a 12.9 mm Wankel engine developed at the University of California at Berkeley. The size of the engine (12.9 mm) describes the length of the minor axis of the epitrochoid or the widest portion of the rotor. This engine has only 6 total parts of which, only 2 that are moving.

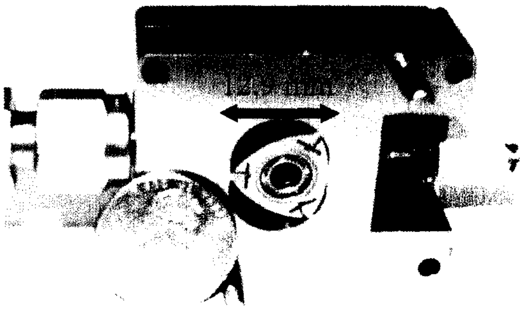

Figure 1-3. 12.9 mm Wankel rotary engine.

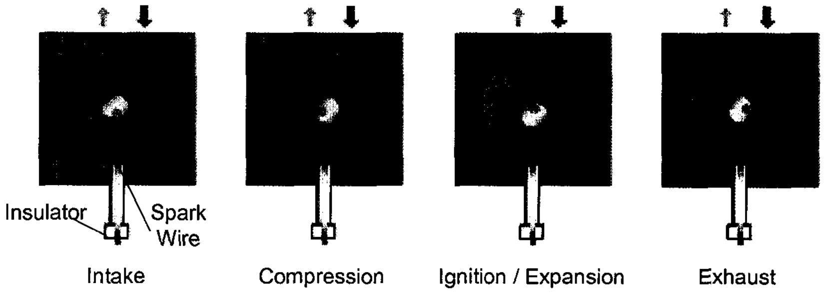

Figure 1-4. Diagram illustrating rotary engine operation.

The rotary engine operates on a four-stroke cycle as shown in Figure 1-4. During one revolution of the rotor, three separate cycles operate simultaneously but 120° out of phase. During the intake stroke, a fresh charge of fuel and air is drawn into the chamber until the following apex closes the intake. As the rotor turns, the fuel and air mixture are compressed until the rotor reaches top dead center. At this point, the charge is ignited with either a spark plug or glowplug. The rapidly expanding gases act thru an eccentric on the rotor generating the output torque of the engine. The combustion products are expelled when the rotor rotates to open the exhaust port. The motion of the engine is controlled by a 3:2 gearing between an annular gear in the rotor and a spur gear located in the housing. The

Wankel design has been used for automobile engines such as in the Mazda RX-7 or for model airplane engines such as those produced by O.S. Graupner.

Historically, one of the primary difficulties in the operation of the Wankel engine is the sealing at the apexes and faces of the rotors. In larger-scale engines such as those produced by Mazda, an elaborate sealing system utilizing leaf springs and steel tabs are used to prevent leakage. Lack of adequate sealing leads to poor engine compression, which degrades engine performance and causes incomplete combustion.

1.3 Proof of Concept: Centimeter-Scale Rotary Engine

In order to examine the feasibility and design issues of small-scale rotary engines, a project was undertaken to examine a centimeter-scale (12.9 mm) rotary engine as a preliminary exercise to the development of MEMS-based rotary engine. The engine was fabricated from stainless steel via Electron Discharge Machining (EDM) and composed of a rear plate, middle housing, top plate, rotor, and shaft (Figure 1-3). Issues such as project feasibility, ignition, apex sealing, and test stand design were examined with this prototype engine. Engine specifications can be found in Table 1-2.

	12.9 mm Engine
Est. Power (W) for 20% Eff.	125
Engine Speed (RPM)	30000
Displacement (mm^3)	348
Fuel Consumption (mL/hr)	62
CO_2 Output (mL/min)	2086
Heat Output (W)	486
Rotor Diameter (mm)	13
Rotor Width (mm)	9

Table 1-2. Specifications for 12.9 mm rotary engine.

At the centimeter-scale, there are no commercially available diagnostic engine test stands. Therefore, a test bench (Figure 1-5) was designed and fabricated to test the mini-engine operation. The test bench consists of an electric motor / dynamometer, optical tachometer, ignition system (for spark plug use), and flywheel. Two different types of ignition systems were used: spark and glow ignition. Spark timing is achieved via a Hall Effect sensor mounted on a rotary dial and a spark ignition system manufactured by CH Electronics, Inc. A spark is then initiated when a magnet on a flywheel attached to the shaft passes the Hall Effect sensor. For testing using a glow plug, a COTS glow plug developed for RC Wankel engines was used. This glow plug consists of a coiled platinum wire which rises in temperature when attached to 1.2 Volt power source. When the platinum wire is hot, catalytic reactions take place on the wire's surface aiding in the combustion of the fuel and air mixture. These reactions also act to maintain the temperature of the wire so that subsequent combustion events can occur without the use of a constant power source to elevate the temperature of the glow plug. This means that power for the glow plug operation is only necessary during initial start-up rather than throughout operation as is the case for the spark ignition system. Engine speed is measured using a Monarch Instruments ACT-3 tachometer with a ROS-5W remote optical sensor. The mini-engine is rigidly coupled to the dynamometer via the engine shaft and flywheel.

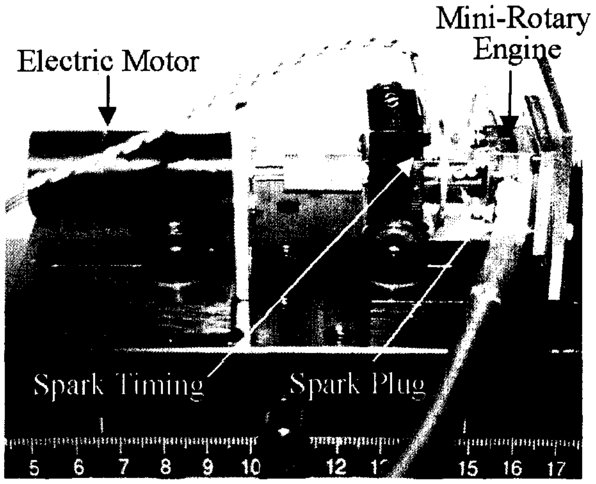

Figure 1-5. Experimental setup for measuring power from a 12.9 mm rotary engine.

For initial combustion testing of this engine, a pre-mixed hydrogen-air mixture is used rather than a liquid hydrocarbon. Hydrogen was chosen as a fuel due to its low ignition energy. A gaseous fuel mixture is advantageous for this study because it does not require the added complexity of a fuel carburetion system. The gaseous fuel and air are premixed upstream of the engine in a T-junction. The fuel flow is metered using valves and rotameters upstream of the T-junction.

To measure engine power, a dynamometer has been developed using a Maxon^{TM} brushless electronically commutated motor and a rectifier circuit. Power generated by the mini-rotary engine spins the dynamometer, which acts as a generator and produces electrical power. The rectifier circuit converts the three-phase output of the dynamometer to a DC voltage potential. Rheostats are used to apply a load to the dynamometer. The rheostats can be adjusted to produce the appropriate load, based on the rotary engine being tested. To calibrate the voltage across the dynamometer load to mechanical power output, the dynamometer is driven by an electric motor while connected to a torque arm and load cell. Temperature measurements were also made upstream of the engine and at the housing near the combustion chamber using thermocouple or infrared imaging. Pressure measurements upstream of the engine were also made to accurately measure fuel and air flow rates.

Based on testing of preliminary designs, the following design features were incorporated into the initial prototype rotary engine:

- Integrated flexure apex seal system to test the applicability of the system in MEMS fabrication
- Exhaust gas recirculation to pre-heat the incoming fuel-air mixture and heat the

combustion chamber with exhaust gases

- Increased size for better manufacturing tolerance

The displacement of the engine was increased from 78 mm^3 to 348 mm^3 to reduce the effects of manufacturing tolerance. The epitrochoid major and minor axes were increased by a factor of 1.33, while the width of the mini-engine was increased from 3.6 mm to 9 mm to reduce axial heat losses. The increase in width also allows for the use of commercial off the shelf (COTS) small-scale glow and spark plugs. Manufacturing tolerance of the 12.9 mm engine was improved from ±0.2 mm to ±0.02 mm.

The 12.9 mm engine generated positive output power operating on H_2-air and using two different ignition sources: 1) a COTS spark plug and 2) a COTS glow plug. The experimental results of tests with the spark ignition will be discussed first. The test procedure typically consists of the following: the engine is initially brought up to speed through the use of pressurized air to overcome friction. The spark system is energized and H_2 introduced into the flow until sustained combustion is obtained. The power generated by combustion results in an increase in engine speed and voltage across the dynamometer load. When the spark is energized, the voltage across the dynamometer load, engine speed, and housing temperature all increase.

During the experiment shown in Figure 1-6, the spark is turned off at three separate times for 5-10 seconds to achieve steady, non-combustion conditions. Without combustion, there is a decrease in engine speed, measured power, and a 1°C/sec decrease in housing temperature due to heat loss to the engine stand and convection.

This difference in power output immediately before the spark is terminated and after the engine reaches a steady state without combustion (spark off) is the net power output

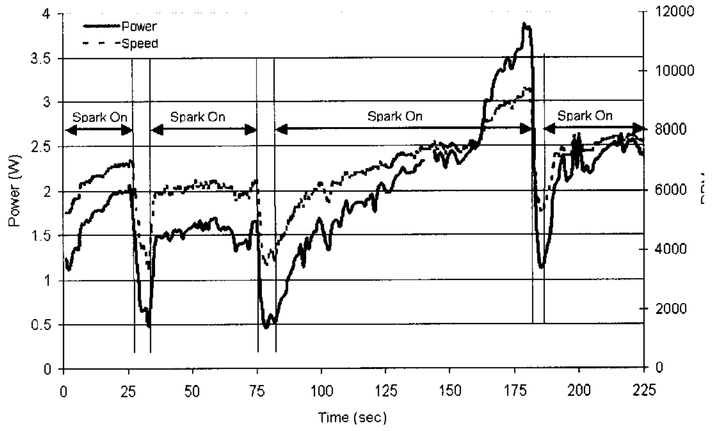

Figure 1-6. Engine power output and engine speed of a 12.9 mm rotary engine operating on H_2-air using a spark ignition.

of the 12.9 mm mini-engine. Figure 1-6 shows a plot of engine power and engine speed. For this particular experiment, the net power output at 25 and 75 seconds is 1.5 W and 1.2 W, respectively. Measurements and control of the fuel and air flow rates were made prior to mixing in the engine chamber. The equivalence ratio, Φ, is defined as

$$\Phi = \frac{f}{f_s} \qquad (1\text{-}1)$$

where f is the measured fuel to air mass ratio and f_s is the stoichiometric fuel to air mass ratio. Between 25 and 75 seconds, the equivalence ratio was determined to be 0.42. At equivalence ratios closer to stoichometric, flashback of the flame occurred into the pre-mixed intake. This prevented the experiment from reaching higher equivalence ratios and higher power outputs. At 100 seconds, air flow is increased to measure power output at higher engine speeds. This leads to an increase in engine power output to 2.7 W with an equivalence ratio of 0.37 due to the increased air flow rate. Spark timing for all three power measurements is 0 degrees BTDC. The experiment was terminated because of lubrication breakdown due to elevated engine temperature. In a separate test, the breakdown temperature of the lubricant was measured to be 275°C.

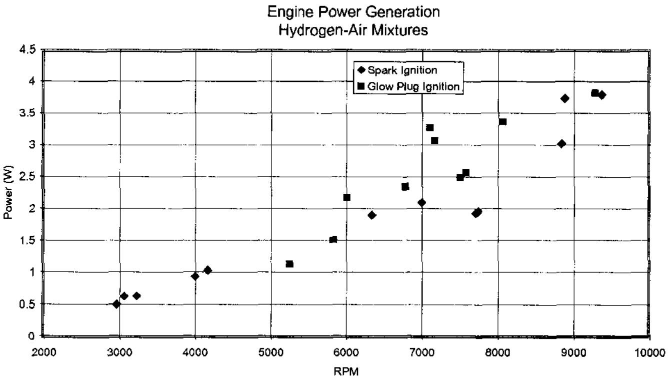

Figure 1-7. Net power output of 12.9 mm mini-rotary engine operating on H_2-air and using spark ignition ($\Phi = 0.4 \pm 0.04$).

The net power output as a function of the peak engine speed for a 12.9 mm mini-engine is compiled in Figure 1-7. The plot indicates a linear rise in power with engine speed consistent with a relatively constant torque output. This indicates the residence time, the time available for combustion within the engine, is greater than the reaction time, the amount of time needed for combustion to occur. The scatter in the data is due to slightly different operating conditions during each test. Equivalence ratios for these tests varied between 0.4 ± 0.04 while the spark timing was maintained at 0 degrees BTDC. The maximum power achieved by the engine is 3.9 W at 9300 RPM with an overall thermal energy efficiency of less than 0.5%. Tests were also conducted using an O.S. Engines Type RE glow plug as the ignition source. Figure 1-8 shows that power output using a glow plug is comparable to that of spark ignition. The glow plug uses platinum or a platinum-composite for the heater coil. Since the platinum acts as a catalyst during engine operation, power is only applied during initial engine startup to provide the initial heat to the platinum. Continual application of power during engine operation is not necessary for combustion to be maintained. This result is critical for implementation of a smaller size rotary engine since a spark ignition system would draw too much energy from the overall system output.

Testing of the 12.9 mm engine proved that power could be generated from a small scale combustion engine with a Wankel design. Positive power output using a glow plug ignition system showed that ignition could be obtained with a minimal amount of power consumed. This work laid the groundwork for the exploration of smaller scale engines fabricated using MEMS.

1.4 MEMS Rotary Engine Power System

1.4.1 MEMS Rotary Engine Power System: Objective

The development of a MEMS-based Rotary Internal Combustion Engine is part of an effort to create a portable, MEMS-based Rotary Engine Power System (MEMS REPS) capable of producing power on the order of milliwatts with an energy density better than

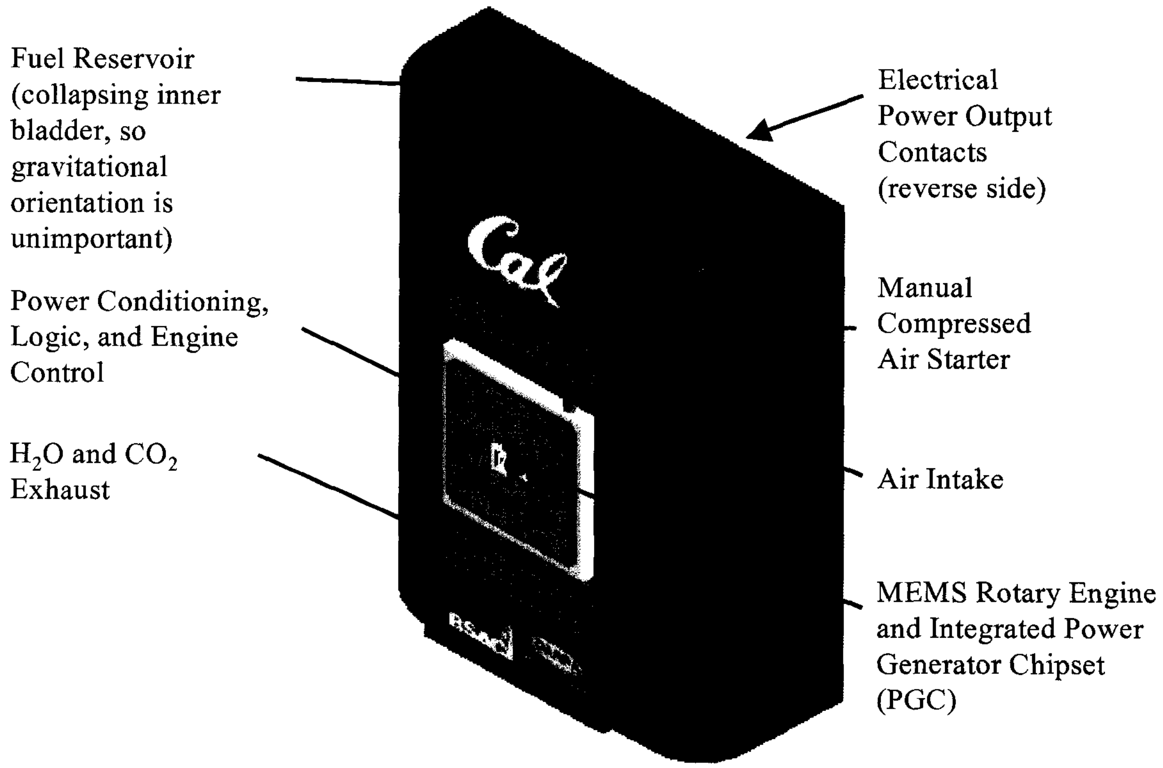

Figure 1-8. MEMS Rotary Engine Power System concept artwork.

that of a conventional battery. The goal of the MEMS REPS is the development of an autonomous portable power system similar to that of a lantern cell or 4 D-cell batteries as shown in Figure 1-8.

1.4.2 MEMS Rotary Engine Power System: Overview

In order for the successful operation of a fully autonomous portable power generation system, efforts are underway to fabricate the sub-systems necessary for system operation. Central to the success of the MEMS REPS is a 2.4 mm rotary engine with an integrated electrical generator and apex sealing discussed in subsequent chapters. As part of this package, the rotary engine will lie at the end of a stalk fixed at the center of a metal container filled with aerogel insulation and a flexible fuel bladder system. The stalk will consist of electrical and fluidic connections between the engine and the surrounding subsystems. Fuel will be driven to the engine thru an evaporation process which scavenges the waste heat generated via combustion. The engine is surrounded by an efficient electrical generator system which does not utilize a coupled shaft to extract

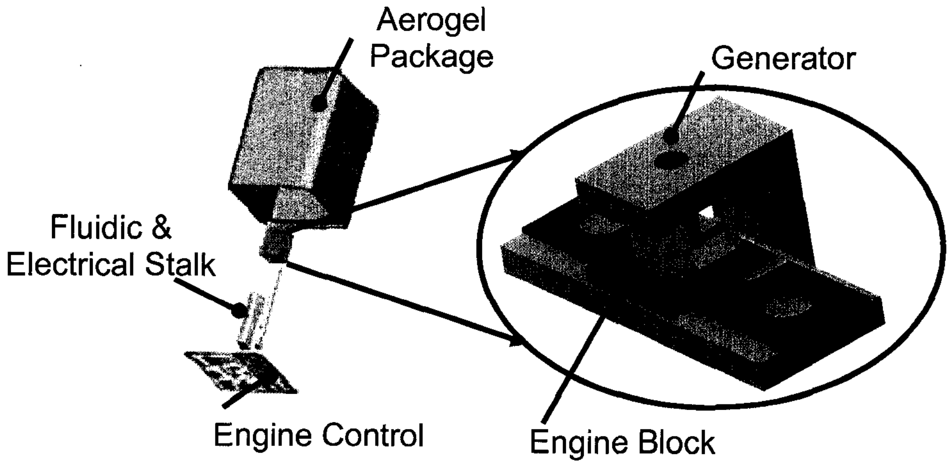

Figure 1-9. Overview of the power generation chipset with electrical generator and engine block.

power from engine. Instead, soft magnetic material will be integrated into the rotor itself via high thickness electrodeposition. The rotor becomes the active component of the generator system. The motion of the rotor generates a voltage difference thru a stator coil located in close proximity to the engine. In addition to the soft magnetic material, in-plane, cantilever apex seals is integrated into the engine. A first step in the demonstration of the MEMS REPS will be an expander design powered by compressed air which will show rotation of the engine in addition to integration of the electrical generator into the engine.

1.5 Dissertation Overview

The overall objective of this thesis is the design and fabrication of a silicon rotary internal combustion engine. Chapter one has laid out the motivation of this work, background, and previous work on a centimeter-scale working prototype engine.

Chapter two details the specifics of the engine design including engine sizing. Design tradeoffs and constraints necessary for the engine's operation within the context of the MEMS REPS and its sub-systems are discussed. Special attention is given to the integration of the electrical generator within the engine housing and rotor and the integration of the apex seals within the rotor itself. The ultimate result of the engine design is a 2.4 mm size scale engine that is 900 μm in thickness.

Chapter three describes the fabrication process necessary to produce the engine components which make up the 2.4 mm rotary engine. Included among these processes is a three-mask single sided DRIE process for the co-fabrication of 900 μm thick engine rotors and epitrochoid housings on the same wafer. Fabrication methods for the spur gear plate and square shaft are also discussed.

Chapter four contains the analysis and characterization necessary for the optimization of the fabrication processes. A detailed examination is made of DRIE for ultra-high thickness etching with an emphasis on vertical sidewalls, low roughness, and high selectivity. In addition, a low pressure etch process is discussed which can be used for wafer-to-wafer bonding. Finally, a partially assembled silicon rotary engine is demonstrated through the use of pick and place assembly.

The final chapter summarizes the results of this work and discusses future improvements to the overall design and fabrication process.

2. Engine Design

Previously, engine components for a 1 mm scale Wankel rotary engine have been successfully designed and fabricated from Silicon using MEMS-based fabrication techniques [2]. However, this design did not focus on how to make this engine within the context of a portable power generation system. Ancillary systems for fuel delivery, electrical power generation, sealing, engine control, and packaging are necessary for the engine's successful operation. This chapter describes the design of a MEMS-based Wankel engine within the context of a MEMS-based power generation system and designed to incorporate an integrated generator and integrated apex tip seals. In order to properly accommodate the subsystems of the engine, tradeoffs must be made between the performance of various components and subsystems of the MEMS REPS.

2.1 Design Goals

The ultimate goal of the MEMS Rotary Engine Power System is to produce a high efficiency system which generates power on the order of milliwatts with an energy density better than that of a battery. An internal combustion engine is a suitable candidate for this system because it can provide a high efficiency and energy density when operating on a liquid fuel due to the high power to weight ratio of a liquid hydrocarbon. The planar geometry of the Wankel rotary engine design allow for MEMS-based batch fabrication techniques to be used in the engine's construction.

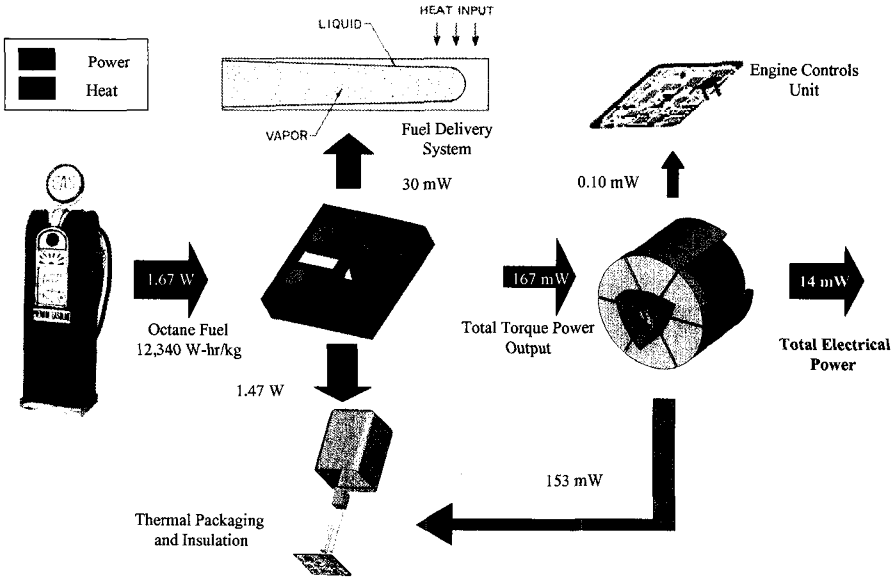

Figure 2-1. Energy budget flow chart for the MEMS REPS.

In order to generate net power from the Rotary Engine Power System (REPS), all subcomponents or ancillary systems must operate with a minimal or ideally, zero amount of electrical power input. With this in mind, a system-wide energy balance is shown Figure 2-1. Electrical energy is only consumed for the purpose of engine control and for initial engine startup. Fuel evaporation and injection is accomplished through scavenging of the waste heat of combustion. For ignition of the fuel mixture, a spark system is not optimal due to its excessive power draw throughout operation. Assuming a mimimum ignition energy of 0.3 mJ per spark event which typical for many common fuels, an engine running at 40,000 RPM will require 200 mW of energy to maintain combustion [3]. Instead, a catalytic glowplug is used which only requires an estimated 50 mW of electrical power during initial engine startup [4].

The MEMS REPS design must also minimize the number of parts and assembly steps required for fabrication. In comparison with traditional large-scale Wankel engine design, a micro-Wankel engine must have even fewer components. This is accomplished by eliminating the small metal springs and tabs used in large scale Wankel engines for face and apex sealing. Instead, microfabricated in-plane, cantilever apex seals are integrated into the rotor of the Wankel engine to avoid tedious assembly. Another example is the co-location of the electrical generator within the engine rotor. This integrated generator design eliminates the need for assembly of external shafts or couplings which would be necessary for an external generator design. In addition, any external coupling system could have been a source of leakage from the engine. A complicated engine sealing system would be necessary to prevent leakage from reducing the compression ratio of the engine.

Finally, engine performance must be maximized in order to obtain the highest possible energy output. Engine performance could be compromised by poor manifold performance, reduced compression, quenching of combustion, surface wear, and frictional losses. Critical to the stability of the combustion reaction is consistent, reliable fuel flow to the engine. Since the engine rotor can decelerate from 40,000 RPM to 0 RPM in as little as 6.5 revolutions from engine friction, a significant misfire could bring the engine to a halt. Not only must the fuel be evaporated and injected into the engine consistently, the flow into and out of the engine ports must be maximized.

Research in larger-scale Wankel engines has shown that combustion stability is decreased if combustion gases are incompletely exhausted to the environment or if the intake stroke does not bring in a completely fresh charge [5]. These difficulties can be overcome through proper port design.

Inadequate engine sealing leads to poor engine compression and therefore, decreased performance. In part, compression ratios depend on the precision of the construction of the engine components. However, experimental testing of the 12.9 mm engine has shown that higher compression can also be achieved thru apex seal performance [2]. Proper control of rotor motion within the epitrochoid can also improve the engine's compression by allowing the rotor apexes to better track the sidewalls of the epitrochoid. This can be accomplished through high precision involute gear teeth and by increasing the number of teeth utilized in the spur and annular gears.

In order to maintain combustion within the engine, the effect of flame quenching must be minimized. Flame quenching occurs when the amount of heat losses from the combustion zone exceeds the amount of heat generated by the chemical reaction. As any internal combustion engine is reduced in size, the surface area to volume ratio increases which leads to an increased role for in engine performance surface effects such as quenching and friction. Proper engine packaging can minimize the amount of heat lost from the combustion chamber. Maintaining high temperature engine walls reduces heat losses and prevents flame extinction [6]. Increased surface wear and friction can degrade overall performance and engine lifetime. However, a surface coating such as SiC has shown improved wear and frictional properties over that of Silicon. Silicon Carbide coated engine would also be more resistant to harsh chemical environments (such as those found in combustion) and allow for higher temperature engine operation [7, 8].

2.2 Engine Sizing

In order to properly design the engine, an engine size must be chosen which produces the amount of mechanical torque compatible with the electrical generator. The following two sections detail the proposed generator system and the relationship between torque output of the engine and the torque capacity of the generator as scaled with engine size.

2.2.1 Generator Overview

Traditional macroscale engine-generator systems usually involve coupled shafts to transfer the mechanical torque generated via combustion to rotation of magnetic rotor with attached stator. This versatile configuration allows for larger stator elements, separation of the magnetic components from the engine, and a variety of approaches for electrical power extraction. When the engine-generator system is reduced in size, alignment between the shaft of the generator and that of the engine becomes difficult to maintain. A slight misalignment of the shafts could generate stress resulting in the catastrophical failure of the engine shaft. An elaborate sealing system would also be necessary to prevent leakage through the output shaft. Coupling of a shaft this size would also require bearings which would complicate the design and fabrication of the engine.

An alternative approach to the engine-generator system is to design the generator and rotor of the rotary engine to be co-located. If the rotor is the rotating component of the generator itself, there is no need for an output shaft to be coupled which eliminates the complexities associated with shaft alignment. By eliminating the rotating components of an external generator, the friction of the entire machine is reduced thereby increasing output power of the system. The disadvantages of this design lie in merging the magnetic components and material into the rotor in terms of fabrication, thermal, and mechanical design.

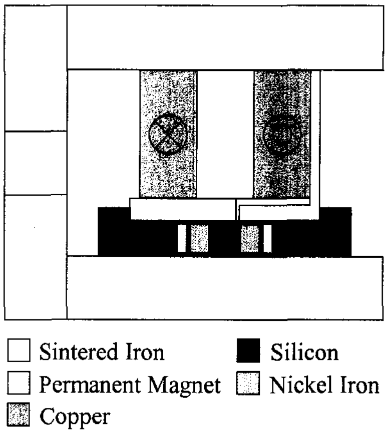

Figure 2-2. Cross-section of the engine-generator system [9].

A schematic picture of a generator mounted on one side of the engine is shown in Figure 2-2 developed by Senesky [9]. The generator consists of a stator formed by coiled copper wire around a magnetically permeable pole, magnetically permeable powdered iron plates located above and below the engine to complete the flux path, and a permanent magnet. The generator operates by imposing an axial flux field on the rotor using a permanent magnet in the stator system. Within the engine rotor are three soft magnetic poles with high permeability which vary the flux through the conductive coil as the rotor turns generating a voltage. The high permeability teeth and pole faces in the stator concentrate the magnet flux through the conductive coil. Figure 2-3 shows an exploded view of magnetically permeable post and teeth system highlighting the flux path arrangement. The teeth of the stator are separated into two sets. One set of teeth directs the flux through the central pole of the stator while the other shunts the flux around the coil to the top plate. As the rotor rotates, the voltage output of the generator is proportional to the absolute value of the difference in area of magnet underneath one set of teeth decreased by the area under the other. The voltage, V, can then be described as

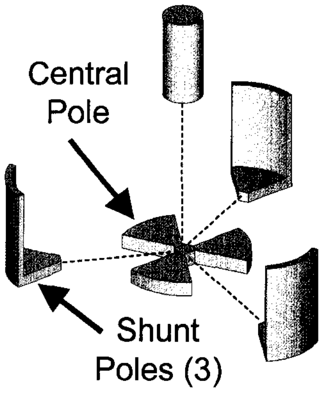

Figure 2-3. Exploded view of generator stator [9].

$$V = \frac{d}{dt}\left(B_{PM} A\right) \tag{2-1}$$

where B_{PM} is the saturation magnetization of the permanent magnet and A is the area of the soft magnetic pole underneath the stator teeth. Since voltage and torque of the generator are proportional to one another, power output of the generator is proportional to the area of the soft magnetic pole squared. Limiting the area overlap between adjacent stator poles thereby increasing the voltage difference between non-corresponding poles and maximizing the soft magnetic pole area are important factors in improving generator performance.

2.3.2 Engine-Generator Scaling

One important aspect of the generator design is to be able to match the output torque of the engine to the input torque absorbed by the generator. The mechanical output of the engine is a function of its geometry, input fuel, and conversion efficiency. The displacement of a rotary engine is defined by the geometry of the engine and can written as:

$$D = 3\sqrt{3}Rwe \tag{2-2}$$

where R is the rotor generating radius, w is the rotor width, and e is the rotor eccentricity.

The mechanical power output of the engine can be written as:

$$P_{mech} = LHV \times \eta_{th} \times \dot{m}_{fuel} \tag{2-3}$$

where LHV is the lower heating value of the fuel used, η_{th} is the thermal efficiency, and $\dot{m}_{fuel}$ can be written as:

$$\dot{m}_{fuel} = D\omega\phi \tag{2-4}$$

where ω is the engine speed and ϕ is the volumetric ratio of fuel.

Mechanical torque from the engine can be written as:

$$\tau_{mech} = \frac{P_{mech}}{\omega}. \tag{2-5}$$

Fundamentally, the performance or torque from the generator is dependent on the geometry of the rotary engine, the efficiency of the stator coil, and the surface area of the magnet. Thus, the power produced by the generator may be written as:

$$P_{gen} = \left(\frac{9}{2} A B_{PM} \omega\right)^2 \frac{(1-\eta_{gen})\eta_{gen}}{R_{coil}} \tag{2-6}$$

where A characterizes the area of magnetic material in the rotor, B_{PM} is the saturation magnetization of the permanent magnet, ω is the rotational speed of the rotor, η_{gen} is the efficiency of the electrical generator, and R_{coil} is the resistance of the stator coil [9]. Similarly to Equation 2-5, the input torque absorbed by the generator can be written as:

$$\tau_{gen} = \frac{P_{gen}}{\omega}. \tag{2-7}$$

By comparing the equations for mechanical output torque of the engine to the electrical output torque of the generator, the size of the engine where the capacity of generator would be drastically exceeded by the mechanical power of the engine can be determined. Figure 2-4 shows a plot where a desired operation point of the engine and generator is located. This point assumes a conservative engine efficiency of 4% and the efficiency of the generator for this point is low (50%) in order to improve the power output of the system. The efficiency of the generator and the degree to which the generator matches the engine output torque could be improved by reducing the fuel flow to the engine. A leaner mixture would reduce the engine's overall torque output. An engine with this configuration would have a thickness of approximately 900 μm and a triangular area of magnetic material located at the apex.

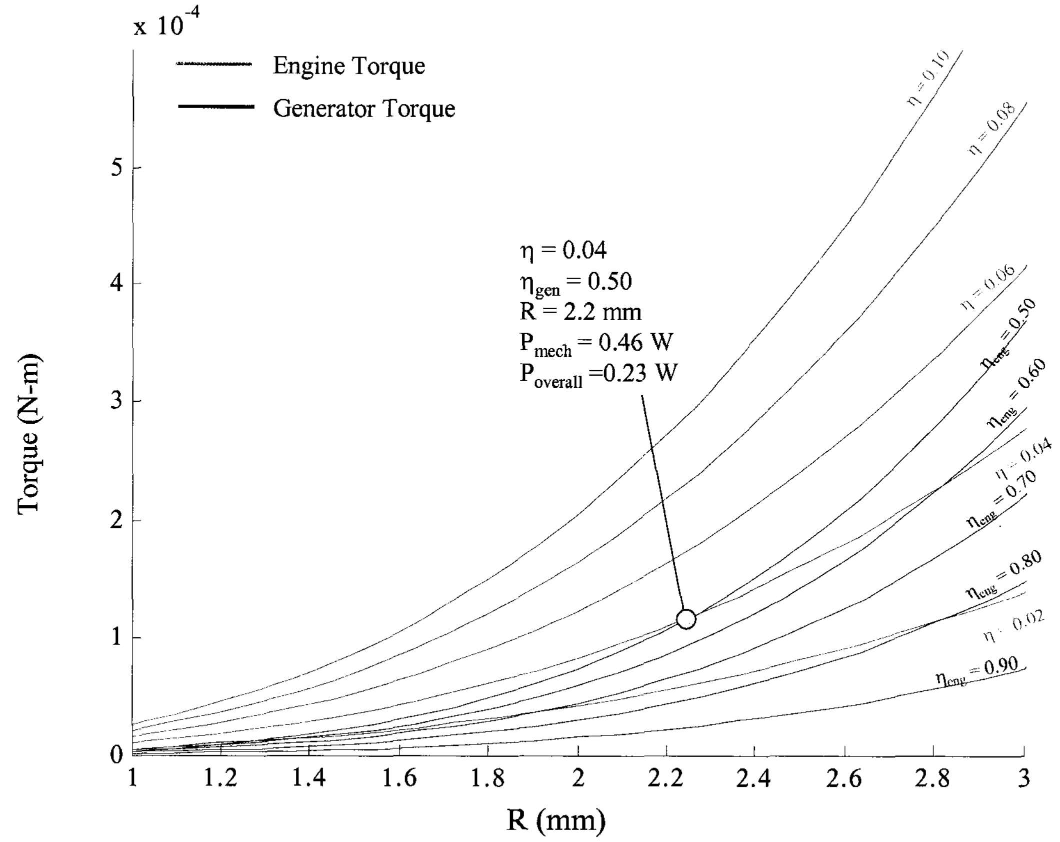

Figure 2-4. Comparison of the torque generated by the engine to the torque accepted by the generator in relation to size and component efficiencies.

2.3 Design of a 2.4 mm Wankel Engine

2.3.1 Engine Design Overview

The design of the 2.4 mm engine is primarily influenced by three factors: proper sizing with respect to the generator, constraints of MEMS fabrication, and fundamental issues of combustion such as quenching. The previous discussion of the generator design showed that ideally the engine would be between 2 and 8 mm in size in order to maximize the amount of torque that the generator would be able to absorb. A larger size engine would be advantageous in allowing the generator to absorb a larger percentage of torque, since generator capacity increases strongly with size. However, the engine size is limited by MEMS fabrication techniques. In MEMS fabrication, Deep Reactive Ion Etching (DRIE) is used to define the engine housing and rotor. An important consideration in the feasibility of the engine design and fabrication using DRIE will be the aspect ratio (ratio of rotor generating radius, R, to the engine thickness, w). The limit in aspect ratio that DRIE can generate will govern the upper limit of engine size that can be fabricated. In addition to engine aspect ratio, the total engine thickness is also a limiting factor. Most MEMS processes are limited to a single sided etch depth of 500 μm. Larger thickness MEMS devices require better plasma resistant photoresists and have difficulty maintaining a vertical sidewall profile.

Table 2-1 summarizes the design specifications of the 2.4 mm engine. Table 2-2 shows a comparison of rotary engines ranging from the 2.4 mm to the Mazda RX-7. As engine size scale is reduced, aspect ratio is also important in considering the effect of quenching. An engine with the same displacement but a larger ratio of rotor generating radius to width will suffer from flame extinguish due to quenching. Ideally, this ratio should be as close to one as possible because the minimum flame size is determined by the smallest

Generating Radius, R (mm)	1.36
Rotor Width, w (mm)	0.90
Eccentricity, e (mm)	0.185
Displacement, D (mm^3)	1.18
Engine Speed (RPM)	40000 (est.)
Power Output (W)	0.24 (est.)
Fuel Consumption (ml/hr)	0.28

Table 2-1. 2.4 mm Engine specifications.

dimension. The lower limit in size is also governed by the energy budget of the entire system including fuel delivery and engine control.

Engine	Displacement, D (mm^3)	Generating Radius, R (mm)	Rotor Width, w (mm)	Eccentricity, e (mm)	R:e	R:w
NSU/KKM 502	497000	102	67	14	7.3	1.5
O.S. Graupner	4973	22	14.5	3	7.3	1.5
12.9 mm Engine	348	7.4	9	1	7.4	0.8
2.4 mm Engine	1.2	1.4	0.9	0.185	7.4	1.5

Table 2-2. Geometric comparison of Wankel engines of various sizes.

2.3.2 Epitrochoid Housing Design

Figures 2-5 and 2-6 show the epitrochoid housing designed for the 2.4 mm engine. The die size for the engine is 8 mm by 8 mm to give adequate room for tubing for the intake and exhaust.

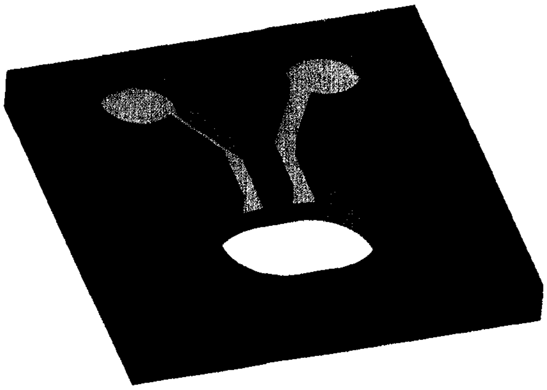

Figure 2-5. Picture of epitrochoid housing.

From the engine parameters listed in Table 2-1, the x and y coordinates of the epitrochoid can be calculated using the parametric equations for the periphery [10]:

$$x = e \cos 3\alpha + R \cos \alpha + a \cos \left(\alpha + \theta_c\right) \tag{2-8}$$

$$y = e \sin 3\alpha + R \sin \alpha + a \sin \left(\alpha + \theta_c\right) \tag{2-9}$$

where e is the rotor eccentricity, R is the rotor generating radius, a is the epitrochoid offset, α is the angular location, and the contact angle, θ_c, is defined as:

$$\cos\theta_c = \frac{R + 3e\cos 2\alpha}{9e^2 + R^2 + 6eR\cos 2\alpha}. \tag{2-10}$$

The epitrochoid offset, a, is necessary for control of the seal lifetime and sizing the epitrochoid with respect to the rotor. Larger epitrochoid offsets will decrease the movement of the apex seal radially which reduces seal wear.

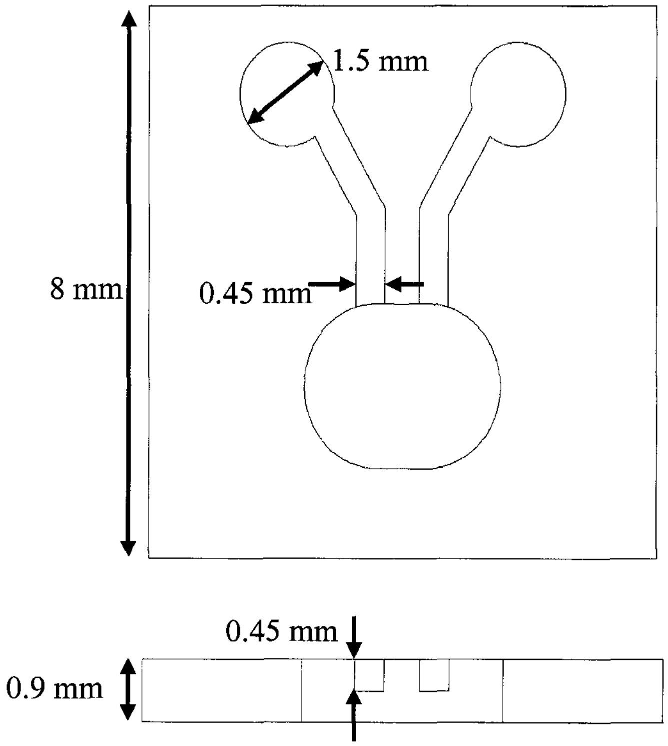

Figure 2-6. Dimensions of epitrochoid housing for a 2.4 mm engine.

2.3.3 Engine Port Design

Traditionally, larger scale Wankel engines are configured such that the intake port is parallel to the axis of the shaft while the exhaust port enters the epitrochoid radially. Figure 2-7 shows this configuration [5]. Recent research into improving Wankel engine performance has focused on improved fuel efficiency and reducing emissions of unburned hydrocarbons through changes in engine porting. During the late 1990s, new automobiles featuring Wankel engines were not available in the United States due to instituted stringent emission controls. Recent advancements in Wankel engine design involving side porting the engine for both the intake and the exhaust have allowed Mazda to reenter the US market with the Mazda RX-8 in 2003 (Figure 2-8). This configuration improves both engine emissions and fuel economy.

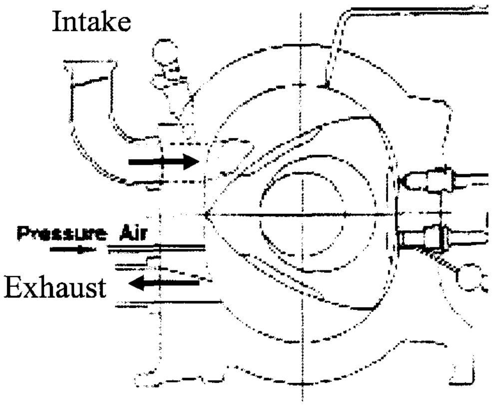

Figure 2-7. Drawing of Wankel engine using side and peripheral porting scheme [11].

When the exhaust is ported peripherally, there is an overlap region where both the intake and exhaust are open at the same time. This tends to draw in already burned gases into the next combustion cycle. These unburned gases reduce the stability of combustion and increase the air-fuel ratio necessary for stable combustion. In addition, gases in areas of the combustion chamber that are not completely burned are sent back through the engine

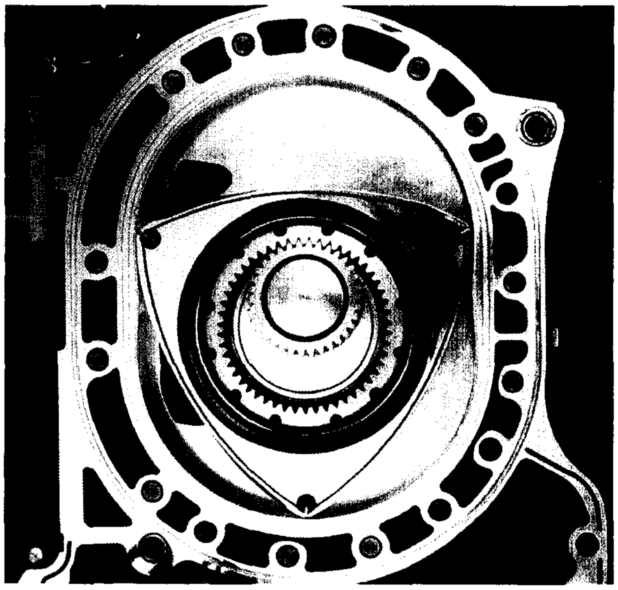

Figure 2-8. Mazda's redesigned Renesis engine with dual side porting scheme [1].

instead of exiting the engine thru the radial port. This reduces the unburned hydrocarbons released by the engine.

These design changes are important as the engine size is scaled down. Since the volume of the chamber is so small, control of the intake and exhaust is important so that a fresh combustion charge enters the chamber during each stroke and combustion is maintained without any misfire. In addition, an axial intake and exhaust allows the engine designer better control of the compression stroke which is important considering the impact even a small leak will have on the compression ratio. One source of leakage that will be reduced by axial porting will be leakage past the apex of the rotor when it passes by a radial port. Axial ports also increase the reliability of the engine rotation since rotary engines have "dead spots" where the rotor does not turn given a pressurized radial air source. In this configuration, the flow into the intake goes directly out the exhaust without rotor rotation.

2.3.4 Rotor Design

The dimensions of the rotor are related to the generating radius, eccentricity, and offset of the epitrochoid. The rotor can be described by a circle of diameter twice that of the generating radius. Within this circle, three arcs can be drawn which intersect each other and the outside boundary of the circle at their endpoints. The distance from the point of intersection between two of the arcs (the vertex of the apex seal) and the opposite arc must equal the minor axis of the epitrochoid. The minor axis of the epitrochoid or the characteristic length scale of the engine (l) is defined as the distance from the vertex of one apex to the center of opposite side of the rotor so that at top dead center (TDC) the side of the rotor touches the housing wall or:

$$l = 2R - 2e \tag{2-11}$$

where R is the rotor generating radius and e is the rotor eccentricity. The center points for the arcs which make up the rotor are not at the vertex of the two adjoining sides but rather slightly outside the rotor. This means that each side of the apex seal has an angle of less than 60° and a radius larger than that of the minor axis of the epitrochoid.

One of the most important aspects of the engine design is to maximize the compression generated in the combustion chamber prior to ignition. The engine thermal efficiency is related to compression thru the following relation:

$$\eta_{th} = \left(1 - \frac{1}{\varepsilon_{th}^{k-1}}\right) - losses \tag{2-12}$$

where ε_{th} is the theoretical compression ratio and k is the ratio of specific heats of the mixture. Losses from the thermal efficiency can be attributed to heat losses from the combustion chamber, inefficiency of combustion, or leakage around the apex seal reducing the compression ratio. There are two modes of leakage within the engine that will decrease the compression. Leakage can occur over the faces of rotor or across the apex of the rotor. In engines developed by Mazda, a complex system of sealing is employed where leaf springs push steel tabs across the gaps at the apexes and the faces of the rotor (Figure 2-9) [11]. In the OS Graupner engine, a 1.3 hp model airplane engine, leaf springs and steel tabs are only utilized at the apexes of the rotor and face seals are not employed.

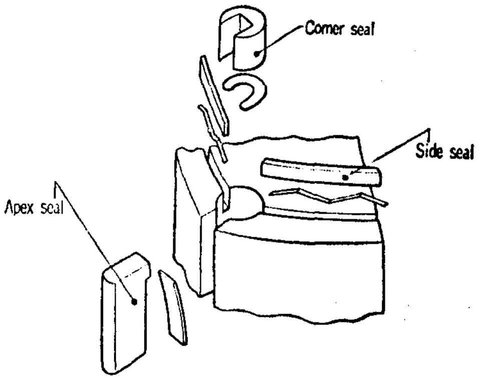

Figure 2-9. Conventional sealing system for large-scale engines (courtesy Yamamoto [11]).

Leakage across the rotor apex or rotor face is generated via large pressure gradients between different sections of the engine. A simplified flow model has shown that gap sizes must be less than 1 μm between the engine housing and the rotor apexes [12]. However, fabrication of MEMS devices with that degree of accuracy for the thickness of the rotary engine would be impossible. Testing conducted with 12.9 mm rotary engine has shown that most engine leakage arises from blow-by around the rotor apexes rather than across the rotor faces [2]. In order to maintain compression and minimize the assembly, an apex sealing system consisting of pre-compressed in-plane cantilever beams are integrated into the rotor apex. Face seals were not developed for the 2.4 mm Wankel engine.

There are three objectives in the design of apex seals for the MEMS REPS. First, the apex sealing system must be capable of high compression ratios in order for the engine to operate efficiently. Leakage around the apex seals must be minimized. Second, the apex seal must be fabricated as part of the rotor. Reducing the size of the apex seal design used by the 12.9 mm engine would not be appropriate since the individual components would be tens of microns in size. Assembly and handling of such small components is not feasible. Finally, the footprint of the apex seal design used for the rotary engine must be minimized. The pole area for electrodeposition of soft magnetic material in the rotor directly corresponds to torque capacity of the electrical generator. Therefore, maximizing the area for the soft magnetic material will improve the generator performance. Figure 2-10 shows an in-plane cantilever apex seal design chosen for use in the 2.4 mm Wankel engine. The in-plane cantilever apex seal leaves a generous area for the poles by occupying only the area along the perimeter of the rotor. In addition, the cantilever beam design does not require any additional assembly or handling.

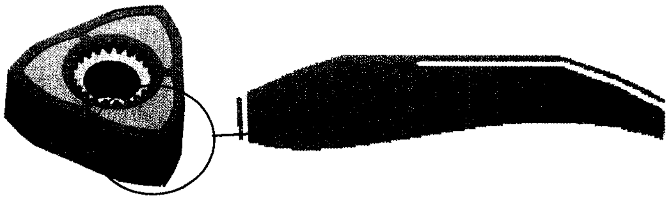

Figure 2-10. Typical in-plane cantilever apex seal.

The apex seal design constraints are separated into 2 distinct categories: performance requirements and geometrical limitations. An ANSYS analysis examined four different performance criteria: resonant frequency, strain, pressure, and power dissipation. Resonance of the apex seal would result in "galloping" which would open leakage paths around the rotor. The seal must also be

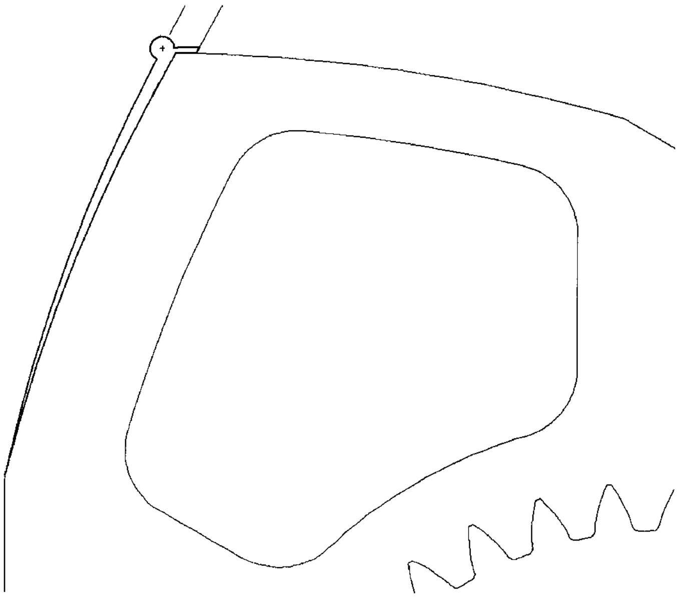

Figure 2-11. Drawing of the rotor with increased outer edge for pre-compression highlighted in dark blue.

designed in order to not fail due to excessive strain. Pre-compressed apex seals are used to counteract forces generated by the pressure differential between two adjacent chambers. Finally, the power dissipated as friction due to force exerted by the apex seal on the wall must be minimized in order to maximize the power output of the engine. The geometric limitations arise from the precision of the DRIE process and are discussed in preceding chapters [13].

Figure 2-11 shows the resulting design of the apex seal in comparison with the exterior wall of the rotor. The apex seal tips are offset by 10 μm in order to obtain pre-compression of the flexure. The tip is rounded in order to maintain the 24° contact angle with the outer wall of the epitrochoid. The apex seals are designed for a pressure differential of 2 atm which would be characteristic of an air expander. Revisions to the design would be necessary to maintain the pressure difference found during combustion.

2.3.4.1 Rotor Pole Shape

The geometry and operation of the electrical generator set constraints on the shape and size of the soft magnetic poles within the rotor. The output of the generator is equal to the absolute value of the difference in voltage generated by the two sets of stator poles (Shunt and Central) shown in Figure 2-3. Therefore, the geometry of the poles should maximize this difference. Figure 2-12 shows an early design of the magnet holes which maximized the amount of rotor area available for soft magnetic material. It is important to note that the stator pole shown in Figure 2-3 is composed of a series of pie wedges which split the circular stator into 60° sections. Superimposing this stator design on top of the rotor, it becomes evident that magnet area which extends under the non-corresponding stator pole will decrease the voltage output of the generator. This is due to the fact that soft magnetic pole area located underneath the non-corresponding stator pole will increase the voltage output of that pole. Since the majority of the soft magnetic pole is underneath the corresponding stator pole, a voltage increase in the non-corresponding pole will reduce voltage output of the generator due to a decrease in the absolute difference of the voltages between the corresponding and non-corresponding poles. Figure 2-13 shows an improved design for the rotor soft magnetic poles which constrains the magnet area to 60° area centered on the apexes of the rotor. This design also prevents fringe fields from the poles from entering the non-corresponding stator teeth by offsetting the edge of the poles by 114 μm [9].

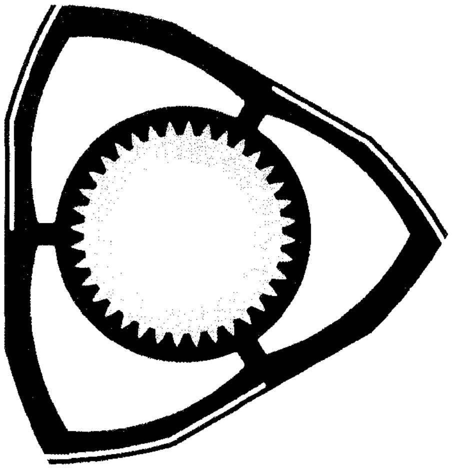

Figure 2-12. Initial design of integrated soft magnetic poles.

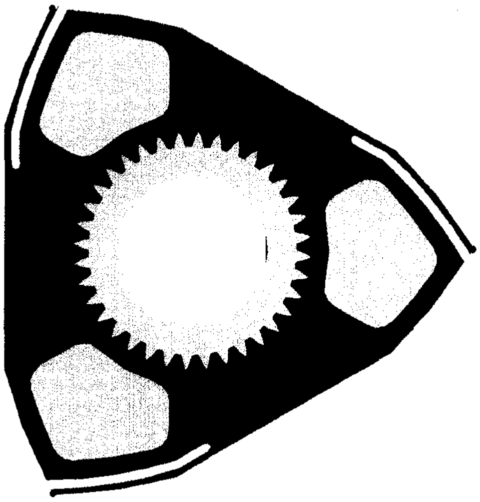

Figure 2-13. Soft magnetic pole design optimized for better generator performance. No changes in overall rotor dimensions were made.

2.3.4.2 Rotor-Soft Magnet Integration

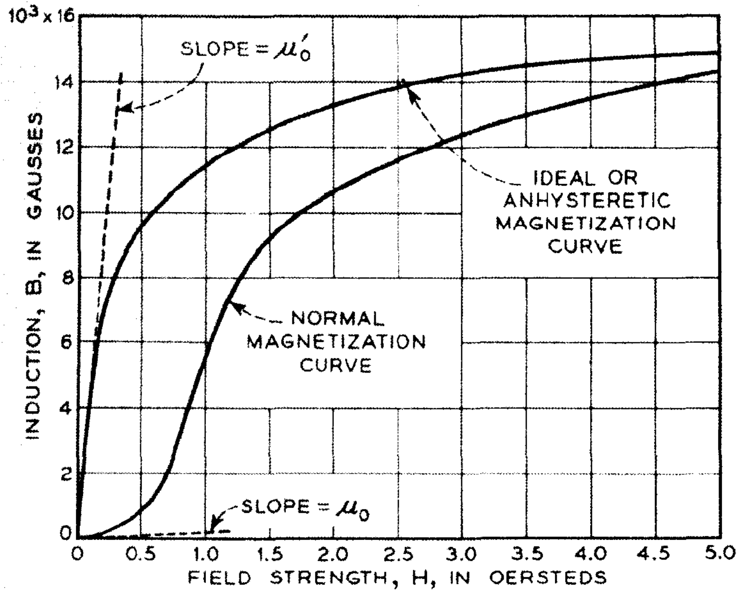

Figure 2-14. Normal and ideal magnetization curves for iron (courtesy Bozorth) [14].

The material selection and design process for the integration of soft magnetic poles into the Wankel engine rotor seeks to optimize the magnetic properties of poles within a high temperature environment. The important magnetic properties for the output power of the engine are the saturation magnetization and the relative permeability of the soft magnetic pole material. Typically, ferromagnetic magnetic materials are characterized by a magnetization curves as shown in Figure 2-14 where magnetic induction is plotted against magnetic force. The saturation magnetization is defined as the maximum value of flux density as the magnetic induction goes to infinity. As applied to the generator design, an increase in the saturation magnetization will result in an increase in the maximum magnetic flux absorbed by the system without overwhelming the material's capacity for magnetic flux. If the material's capacity for magnetic flux is exceeded, this causes the relative permeability to fall to zero and failure of the generator system. Increasing the maximum flux capacity of the system is important since voltage is proportional to rate of change of the absolute magnetic flux. While not equally important, increasing the permeability will also help to increase the maximum flux capacity of the generator by preventing the fall-off of permeability at high saturation magnetization.

Combinations of Cobalt, Iron, and Nickel make up the range of ferromagnetic materials available for use in the engine-generator system. Table 2-3 shows a sample set of soft magnetic materials considered and their material properties. Since the generator output goes as saturation magnetization squared, ideally the rotor poles would be fabricated entirely of Iron. However, an important constraint in this design is the operating temperature of the engine. High rotor temperatures can have two adverse effects. First, high temperature within the rotor can cause rotor structural failure due the difference in the thermal coefficient of expansion between the Silicon and soft magnetic pole material. For example, the thermal expansion coefficient of Iron is 6 times that of Silicon. Secondly, high temperatures can result in failure of the soft magnetic material by approaching the allowable Curie temperature of the material.

	Coeff of Thermal Expansion (1/°C) @ 20°C	Saturation Magnetization (Tesla)	Curie Temperature (°C)
Pure Iron	11.7e-6	10	770
Pure Nickel	13e-6	6	360
Pure Cobalt	14e-6	18	1000
Permalloy (80Ni:20Fe)	12e-6	11	580

Table 2-3. Material properties of common soft magnetic materials [14].

In addition to engine operating conditions, the practicality of fabrication and integration of the soft magnetic materials must also be considered. There are two possible methods for fabrication of the soft magnetic poles: assembly of machined soft magnetic parts into the rotor or electodeposition of soft magnetic material directly into poles within the rotor. Assembly of the soft magnetic material would be a painstaking, impractical task but could possibly allow a wider variety of materials to be used in the engine than electrodeposition. The advantages of electrodeposition lie in the maturity of specific electroplating processes such as NiFe and the minimization of assembly. The difficulty of electroplating would lie in the integration of that technology into the fabrication process of the engine and extremely high thickness of NiFe that would be required.

An additional advantage of NiFe electrodeposition is that some alloys of NiFe have coefficient of thermal expansion as low as that of Silicon. Figure 2-15 shows the

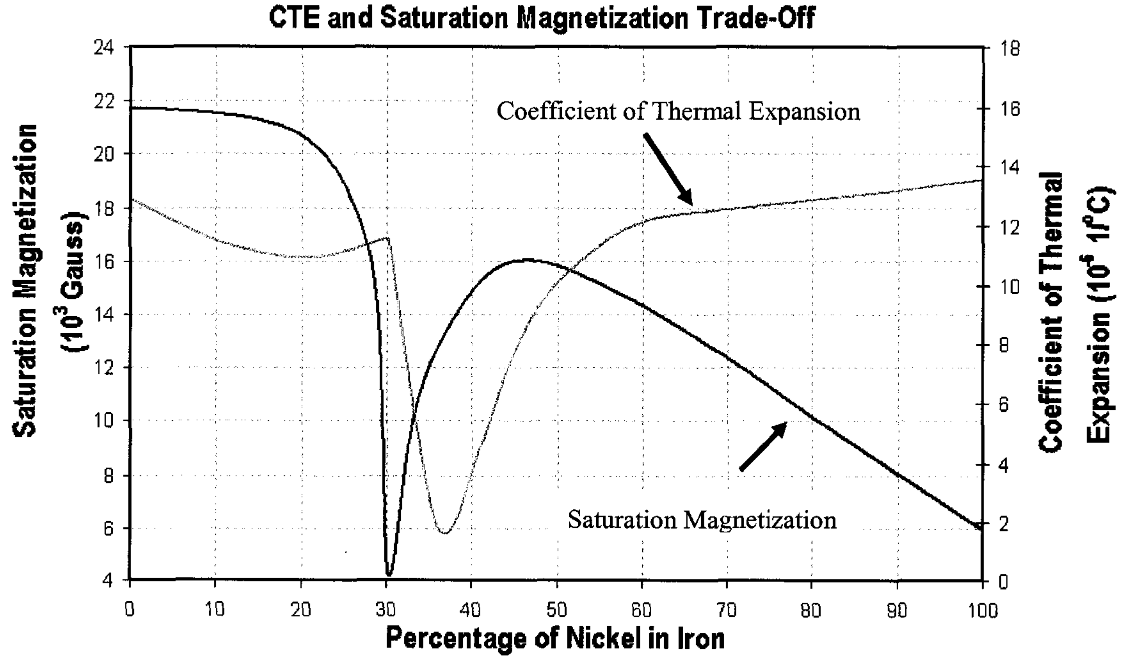

Figure 2-15. The tradeoff between saturation magnetization and coefficient of thermal expansion for various compositions of NiFe [14].

relationship between NiFe composition and the thermal expansion coefficient and saturation magnetization. Due to a martensitic phase change in the material between 30-40 % Ni, the NiFe exhibits a very low coefficient of thermal expansion but unfortunately a very low saturation magnetization.

Therefore, one important consideration in the rotor design is what difference in coefficient of thermal expansion is acceptable in terms of a mechanical design. A range of compositions can then be identified within which the saturation magnetization can be maximized. Finite element models using ANSYS were developed to explore both the geometrical design and the composition constraints for the NiFe pole material. Figure 2-16 shows the rotor model used to determine stresses developed due to thermal coefficient mismatch.

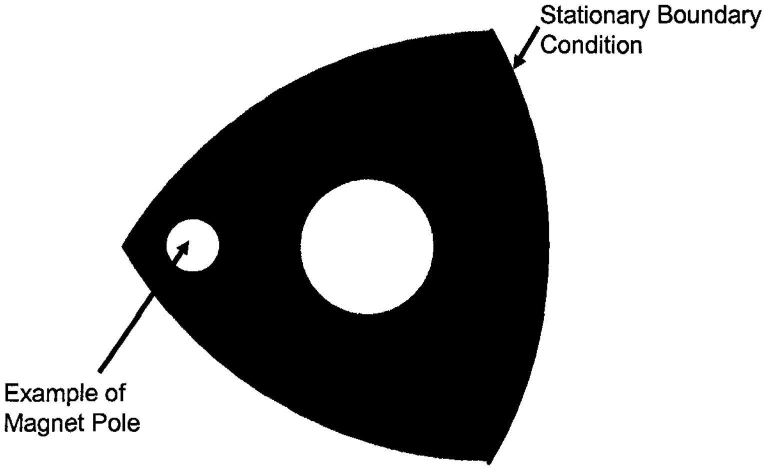

Figure 2-16. ANSYS model used to analyze stress generated by thermal material mismatch.

Initially, a simple geometry such as a circular magnetic pole located at the apex of each rotor was explored to examine the effect of composition on the stress generated by thermal mismatch. Magnetic poles located at one apex were examined with a stationary boundary condition applied to the opposite side of the rotor. The stationary boundary is sufficiently away as to not generate any stress in the area of interest. The temperature of the rotor is set to a constant elevated value of 1000°C. The expansion was modeled by using the room temperature values for the thermal coefficient of expansion to give a simple first order analysis.

In order to validate the results of any FEM modeling of the stresses generated by thermal mismatch, a simple analytical model of the stress in the rotor was developed. The rotor can be assumed to be a simple 2-D cylinder with a radius, R_o filled with a material with elastic modulus, E_0 and Poisson's ratio, ν_0. The center of the cylinder can be filled with a dissimilar material with radius, R_i and material properties, E_i and ν_i. The tangential and radial stress components generated by a temperature rise R_o and a coefficient of thermal expansion, α_i can be written as:

$$\sigma_t = \frac{R_i^2 P_c}{R_o^2 - R_i^2}\left(1 + \frac{R_0^2}{R^2}\right) \tag{2-13}$$

and

$$\sigma_r = \frac{R_i^2 P_c}{R_o^2 - R_i^2}\left(1 - \frac{R_0^2}{R^2}\right) \tag{2-14}$$

where R is the radial location of interest and the contact pressure, P_c, is defined as:

$$P_c = \left[\frac{R_i^2}{\delta E_o}\left(\frac{R_o^2 + R_i^2}{R_o^2 - R_i^2}\right) + \nu_o + \frac{R_i^2}{\delta E_i} - \nu_i\right]^{-1} \tag{2-15}$$

where the interference, δ, is a function of the temperature difference, ΔT, and defined as:

$$\delta = \alpha_i \Delta T R_i . \qquad (2\text{-}16)$$

Figure 2-17 shows the ANSYS FEM stress results for some very simple soft magnetic pole geometry. This stress indicated in this figure corresponds to the anticipated stresses calculated through the analytical solutions given in Equations 2-13 and 2-14. These results show a range of thermal expansion coefficients where rotor stress is within the yield stress of Silicon (7 GPa) [27]. This analysis proved that low thermal expansion soft magnetic poles would not cause catastrophic failure of the rotor. In addition, very rounded designs are favorable in order to minimize stress

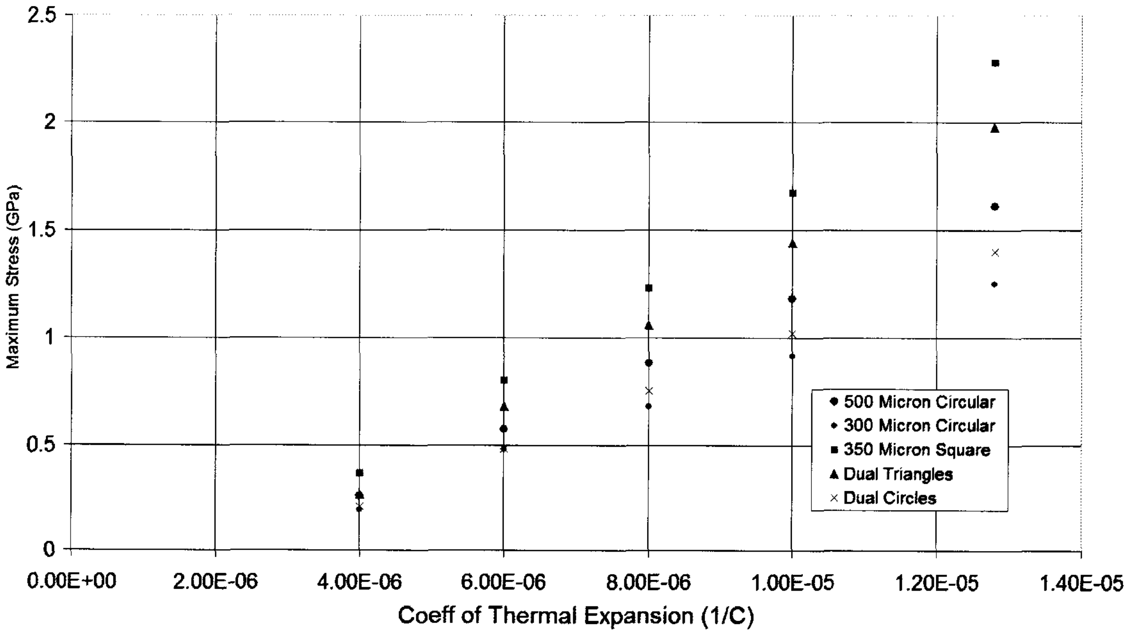

Figure 2-17. Summary of ANSYS FEM stress analysis for simple rotor pole geometries.

concentrations. However, this analysis was somewhat limited because the test geometries did not seek to maximize the pole area which is important for maximizing generator output. In addition, a more exact definition of the thermal expansion as it varies with temperature should be employed.

In addition to thermal and mechanical considerations, NiFe alloys have been historically used in magnetic applications in MEMS. Most applications of NiFe plating in MEMS involve micro-actuation or as a structural material using LIGA [15, 16]. For applications in microactuation, the NiFe layers are usually only a few microns and utilize a photoresist mold. However, the generator design for the micro-rotary engine requires ultra thick electrodeposition thru 900 μm within a silicon mold. However, work by Leith and Schwartz has shown that ultra-thick electrodeposition of $Ni_{80}Fe_{20}$ through 200 μm tall PMMA molds is possible [17]. The deposition was made using a uniform injection cell (UIC) where the mass transfer at the device scale is controlled in order to get a uniform deposition, high yield, and rapid growth rate. For the integrated generator application, it is important that the NiFe layer is uniform across the rotor as well as uniform in composition thru the thickness of the deposited layer in order to get consistent magnetic properties. The integration of the electrodeposition into the fabrication of the rotor will be important consideration in the determination of the rotor fabrication process.

2.3.5 Spur Gear Plate Design

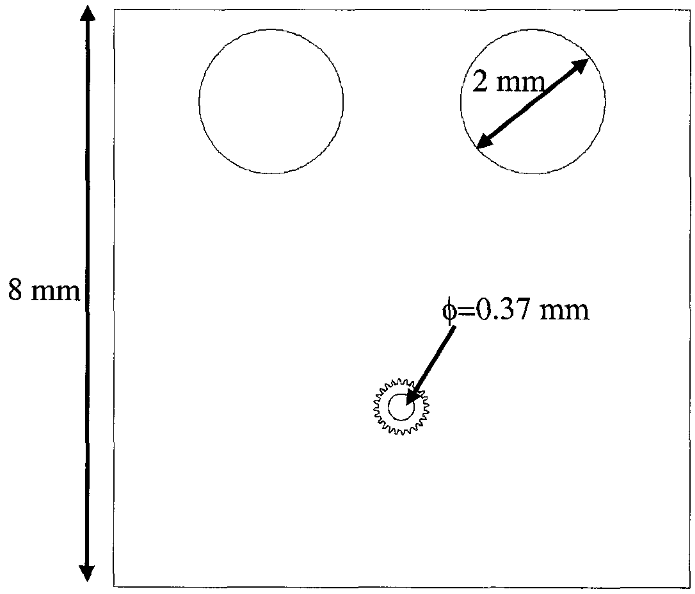

Figure 2-18. Drawing of the spur gear plate.

In this design, the spur gear plate serves three different purposes. First, the plate serves as a porting plate for the intake and exhaust gas flows. Secondly, a spur gear located on the top surface of the plate. The purpose of the gear teeth system in the rotary engine is twofold. First, the gearing system transmits the power generated by the engine to the shaft. Secondly, the gearing controls the motion of the rotor with respect to the epitrochoid. This insures that the rotor apexes and apex seals remain in contact with the outside walls of the epitrochoid at all times. In addition, the spur gear plate acts as the mounting bracket for the stator used for the electrical generator. Figure 2-18 shows the design of the spur gear plate.

The universal method for producing conjugate action or constant angular velocity ratio (rolling without slipping) between two sets of gear teeth is an involute profile. The x and y coordinates for the involute profile were generated with the following parametric equations [18]:

$$x = d(\cos\theta + \theta\sin\theta) \tag{2-17}$$

$$y = d(\sin\theta + \theta\cos\theta) \tag{2-18}$$

where d is the pitch diameter and θ ranges from 0 to 45 degrees for one flank of one gear tooth.

2.3.5.1 Spur Gear Plate-Stator Spacing

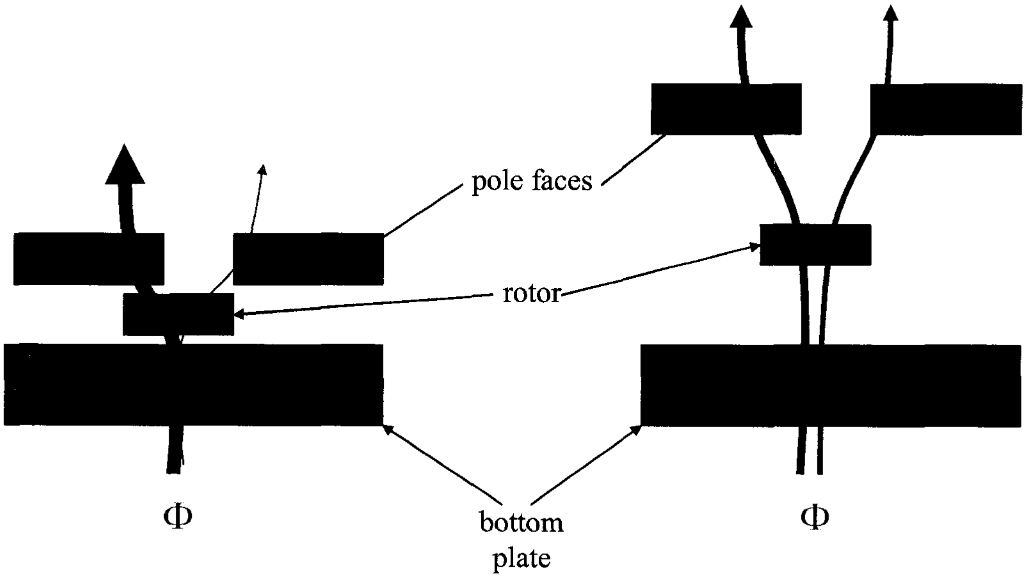

Figure 2-19. Illustration of the effect of rotor-stator spacing on flux [9].

An important factor in the efficient operation of the generator is the spacing between the stator face and the rotating soft magnetic material. Figure 2-19 shows graphically the effect of spacing between the rotor and stator on the flux path. As the gap increases between the rotor and stator, the fraction of flux that passes through the stator pole faces decreases. This trend is due to the fact that to a first order, the engine-generator system is analogous to a circuit with two resistors representing the resistance to magnetic flux of the gap between the stator pole face and the rotor and the stator bottom plate and the rotor. There are no resistors representing the rotor poles, stator, and permanent magnet since they are all composed of magnetically permeable material. Since power generated is proportional to voltage squared, higher resistance due to larger non-conductive or "air" gaps will lead to lower voltages and consequently, lower generator output. Modeling gives a relationship between the "air" gap and the flux which passes through the stator as shown in Figure 2-20 [9]. This plot shows that the stator pole face must be within 200 μm of the rotor which constrains the design of any mounting assembly for the stator. It is important to note that this value only constrains the spacing between the stator and the rotor. Modeling results indicate that the spacing between the powdered iron magnetically permeable plate located on the opposite side of the system is less sensitive to its location with respect

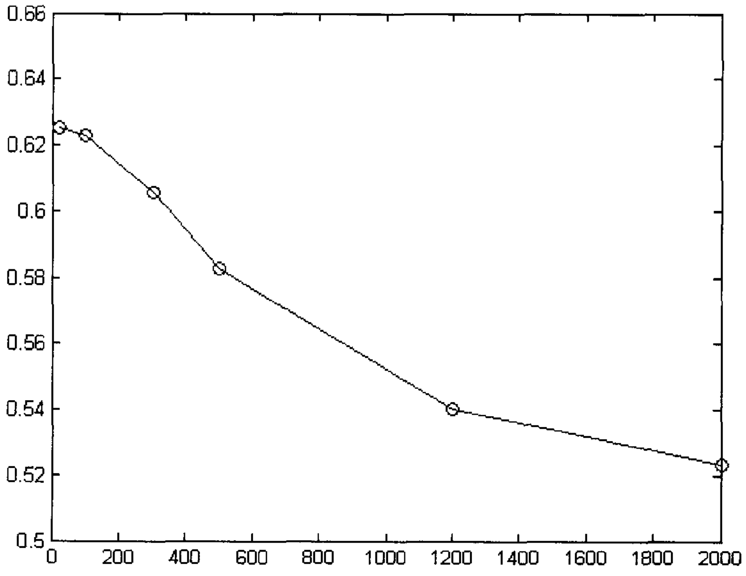

Figure 2-20. Plot of fraction of flux through the pole face versus the gap (μm) between the rotor and stator [9].

to the rotor.

2.3.6 Shaft Design

The shaft of the rotary engine serves two major functions. First, the shaft transmits the torque generated by combustion forces acting on the rotor. Second, the shaft keeps the gear on the rotor in mesh with the gear on the rear plate, thereby ensuring the proper kinematic motion of the rotor is guaranteed. Figure 2-21 shows an example of a shaft used for a large-scale rotary engine. The shaft is separated into three sections: an output shaft, an offset cam, and a rear shaft. One possible shaft design configuration can be seen in Figure 2-22. The geometry of the shaft is dictated by the rotor eccentricity, *e*. The radius of the rear shaft is equal to twice the eccentricity. The radius of the offset cam is equal to four times the eccentricity and offset from the

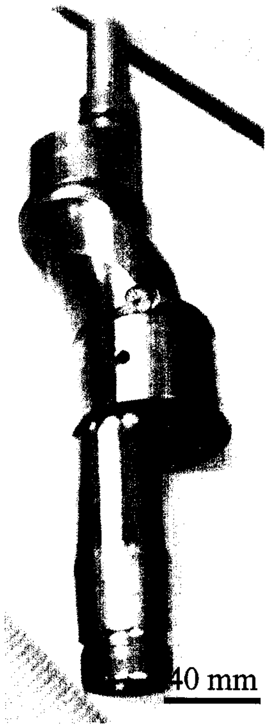

Figure 2-21. Metal shaft used for a dual rotor Mazda engine.

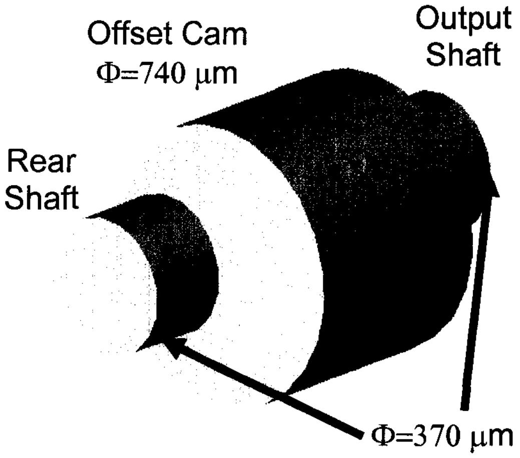

Figure 2-22. Sketch of round shaft design for the 2.4 mm engine.

centerline of the output and rear shaft by a distance equal to the eccentricity. This configuration results in a shaft where the outer wall of the cam, output, and rear shaft coincide at one point. This type of shaft design will be important for simplifying the fabrication process. The offset cam of the 2.4 mm engine is 740 μm in diameter while the output and rear shaft portions are 370 μm in diameter.

2.4 Fuel Delivery

The goal of the fuel delivery system is to evaporate and pump liquid fuel mixed into the intake charge to the engine in a consistent, reliable manner. An emphasis in the system analysis of the MEMS REPS is the minimization of power consumed by ancillary equipment. Since the output power of the system is less than 100 mW, the use of pumps or valves to control the fuel or air flow into the engine is not practical. Similarly, electrical heaters cannot be used to evaporate the fuel. A passive method for the evaporation and pumping of the fuel is necessary. During combustion of a 10% efficient 2.4 mm engine on gasoline, 1.47 W of heat is dissipated (Figure 2-1). If the engine is operating at 40000 RPM, only 2.4 mW of total heat dissipated is necessary to evaporate fuel such as octane. Over a 250 by 250 μm square, this corresponds to a heat flux from the engine of 3.9 W/cm^2. This heat flux does not appear to be excessive since a micro-cooler developed at the University of California at Berkeley has demonstrated operation above 200 W/cm^2 [19]. Since the vapor pressure of the gasoline at 200°C is 5 atm, the evaporation process can be used to pump the fuel to the engine. The channels containing the vaporized fuel can be routed underneath the engine to prevent re-condensation.

In addition to pumping and evaporating the fuel, the fuel manifold also mixes the fuel with an air stream. For the intake port geometry shown in Figure 2-15, the Reynolds Number of the airflow will be on the order of 40 assuming a fully developed laminar flow. With the assumption of a steady, laminar flow, the mixing of the fuel will be difficult because the fuel will require a long length of channel to adequately mix with the air prior to intake into the engine. Assuming a diffusion coefficient of 0.2 cm^2/sec, the necessary time for molecular diffusion can be written as:

$$t_d = \frac{H^2}{D_c} \tag{2-19}$$

where H is the height of the channel and D_c is the diffusion coefficient. The available time for mixing in the intake manifold can be written as:

$$t_a = \frac{3LA}{D\omega} \tag{2-20}$$

where L is the length of the channel, A is the cross-sectional area of the channel, D is the engine displacement, and ω is the engine speed. According to this worst-case scenario, 13 mm of channel length is necessary for mixing of the fuel and air prior to entry into the engine.

Several strategies can be used to promote mixing within the intake manifold. One important consideration of any manifold design is the pressure drop that would be incurred. Another important design factor is to minimize the area where mixing occurs so that there will be less preheating of the fuel-air mixture. Preheating of the fuel air mixture can cause pre-ignition of the fuel in the intake and also lead to poorer volumetric efficiency due to lower density. One method of mixing on the microscale that can reduce the length scale necessary for mixing is pulsatile flow. This method mixes two liquids through alternating, pulsed flow. The distortion of the alternating packets of fluid into the mixing channel increases the interface between the fluids where diffusion can occur [20]. One application of this method to enhance mixing between the fuel and air mixture is to use a series of 180° turns prior to the intake port. The flow patterns of the fuel and air thru the turns caused by the momentum of the fluid will increase the diffusion interface similar to the pulsatile micropumps developed by Deshmukh [20]. This configuration would still have a high pressure drop because the bends in the channel will increase the flow resistance. A more compact approach would be to inject the fuel at different heights within the channel rather than from one side. Initially, the fuel would be better dispersed within the air flow and would more rapidly diffuse to areas of low fuel concentration. A conceptual idea of this approach would involve flowing the air thru a porous region where the fuel is injected at each pore. The intake manifold would still have a high pressure drop but the fuel-air mixture would take place within a smaller space.

2.5 Ignition

Minimization of energy consumed by the engine is the central goal of the MEMS REPS. Ignition is one system necessary for engine operation which requires energy input. In typical automotive engines using a Wankel design, ignition is performed by one or two spark plugs per rotor. However, the majority of small-scale engines, such as those used in model airplanes, use glowplugs for timing simplicity, electrical simplicity, reduced weight, and higher engine speeds and power output. Table 2-4 shows a comparison of power consumptions of microfabricated spark plugs to glowplugs [4, 21]. With an anticipated power output of 10-100 mW, a spark ignition requires an excessive amount of external energy to operate. Glowplugs, on the other hand, only require heat to reach their initial temperature and do not need energy input to maintain combustion.

	Glowplug	Spark Plug
Start-up	50 mW	830 mW
Continuous Operation	0	3.3 W

Table 2-4. Energy consumption comparison between spark and glowplug ignition.

The most important aspect of a micro-glowplug design is to reduce the heat losses from the heater. Heat losses from the heater will reduce surface temperature leading to higher energy consumption to obtain the necessary surface temperature. One means to accomplish this is to insulate the heater from its surroundings. A possible configuration for heater insulation is to use a low thermal conductivity membrane over a large cavity. A membrane composed Silicon Nitride or Silicon Dioxide would have 10-100 times

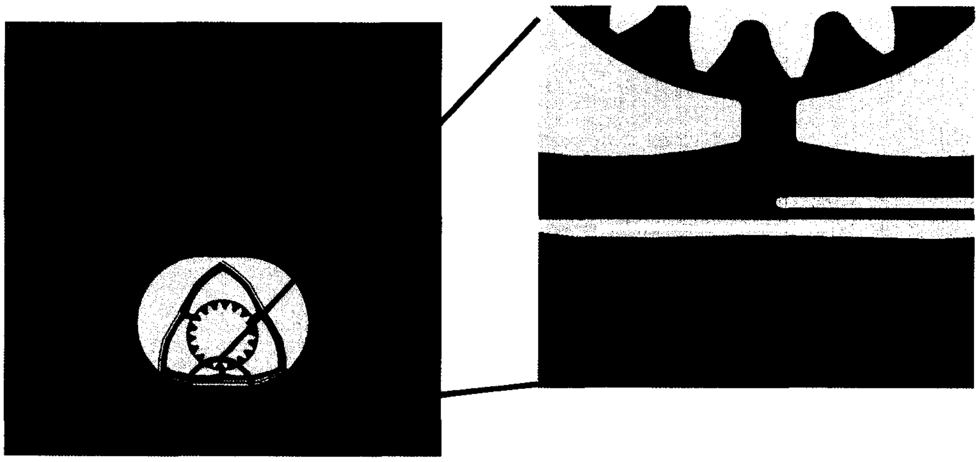

Figure 2-23. Top view of a 10 μm wide platinum heater when the engine is at top dead center.

lower thermal conductivity than Silicon. The cavity and the thin layer of insulating material will reduce conductive losses from the heated area. Experimental and theoretical modeling of microheaters utilizing polysilicon resistors has shown that temperatures of 230°C can be obtained with heat input on the order of 50 mW [4, 22]. The area used for the heaters was quite larger (1.6 mm by 1.6 mm) when compared to the size of the TDC region.

One possible configuration of the ignition system is shown in Figures 2-23 and 2-24. The platinum heaters must be inset above and below the combustion chamber in order to keep the microfabrication process planar. Behind the heaters, the silicon can be etched away using a wet etch to further insulate the heaters from their surroundings.

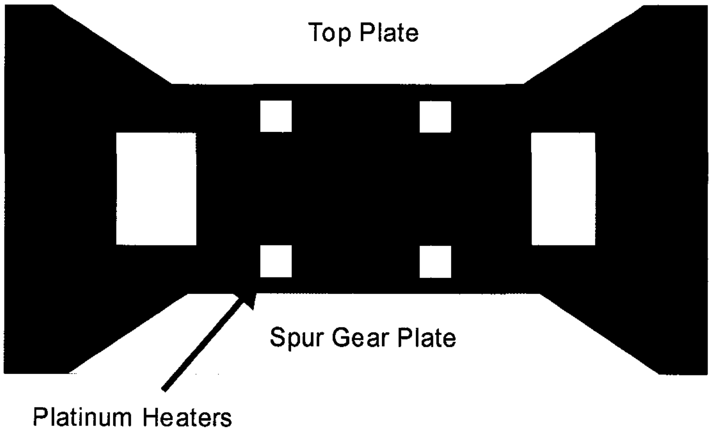

Figure 2-24. Cross-section of engine with dual igniters in both the top and spur gear plates of the engine.

2.6 Thermal Issues

Typically, most automobile engines have water or air-cooling systems to prevent failure of engine components due to excessive temperature. In direct opposition to most large-scale engine design, the combustion chamber of a MEMS-based engine must be kept at an elevated temperature in order to prevent flame extinguishment due to quenching. Previous work in microscale combustion by Cooley showed that flame extinguishment could be prevented through minimization of heat losses. In experiments with methane flames in small tubes, Cooley used electrical heaters, adiabatic walls created by tube bundling, and exhaust gas recirculation to heat the tube walls and decrease the quenching distance further [23].

For the design of a MEMS-based engine, electrical heaters are not practical choice to heat the engine walls because the energy consumed by the heaters would surpass the energy output of the engine. However, a better approach is to channel the hot exhaust gases from the engine around the outside of the chamber. Figure 2-25 shows a possible channel design for combustion chamber fed by radial porting with reheat by exhaust gases. It is important that the exhaust gases do not flow around the intake and compression sides of the engine. Increasing the temperature of the intake gases will reduce the compression thereby reducing the efficiency of the engine. For an axial ported design, the reheat channels can be co-located on the manifold plate directly above the engine.

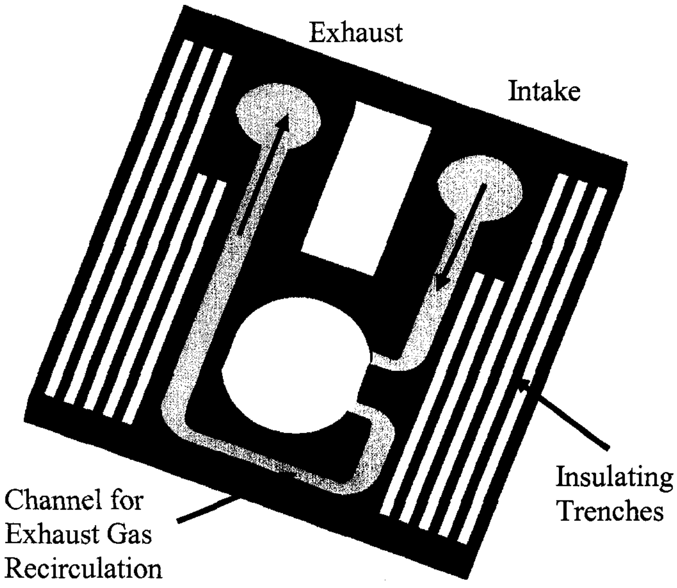

Figure 2-25. Design for exhaust gas recirculation and thermal management.

In addition to locally heating the engine chamber with exhaust gases, the heat losses from the entire system to the surroundings must be minimized in order for engine bloc to remain at an elevated temperature. This can be accomplished by encapsulating the engine with a low conductivity material such as an aerogel. Commercially available vacuum-pulled aerogel can have thermal conductivities as low as 0.003 W/mK. Then, the intake and exhaust gas streams along with the electrical wiring necessary for the generator are the only high conductivity paths for heat transfer to the environment.

2.7 Materials of Construction

In order to make a MEMS rotary internal combustion engine and generator into a competitive alternative to the traditional battery, advanced manufacturing methods must be utilized to lower the per-unit cost of the device. Leveraging the batch fabrication technology pioneered in the semiconductor industry, MEMS fabrication using Silicon as the material of construction provides a method of construction that might be able to compete with existing battery technology. Unlike most typical MEMS devices, this engine will be exposed to a harsh chemical environment, high temperatures, and rotating components. In larger scale engines such as those found in automobiles are constructed using metal exclusively. The temperature of these larger scale engines is controlled thru cooling systems such as a radiator which prevents the metal components of the engine from failing or binding. In contrast, the engine block temperature of the 2.4 mm engine must be elevated in order to prevent quenching of the combustion flame. Table 2-5 shows the material properties for typical MEMS as compared to automotive ductile iron

(D5506) used for engine crankshafts. This comparison illustrates that materials used in MEMS processing can sustain a much higher engine temperature than their metal counterparts. An equally significant benefit is the fact that thermodynamic efficiency of the engine scales favorably with the engine operation temperature.

Material	Hardness (GPa)	Modulus (GPa)	Oxidation Rate (nm/hr) @ 850°C	Coefficient of Thermal Expansion (°C^{-1})	Melting Point (°C)
Iron (D5506)	1.8-2.5	152	46	12 x 10-6	1539
Si (100)	9.6	190	2.9	3 x 10-6	1440
3C-SiC	24	440	0.5	5 x 10-6	2830

Table 2-5. Comparison of semiconductor materials to typical engine block materials [7, 8, 24, 25].

In addition to temperature, it is important to consider other properties of the engine's operating environment. As the size of the engine is scaled down, surface effects will become more dominant than volumetric effects due to the increased surface area to volume ratio. Therefore, engine friction will increase with decreasing engine size. The engine material will need to be resilient to scratches and operating wear. This is another advantage of using metal or metal coatings in large-scale automotive engines. Metals are also durable in the presence of harsh chemical environment produced from combustion. Previous research has shown that Silicon by itself is not an adequate material for the corrosive chemical environment or the wear conditions expected in the engine [26]. However, Silicon Carbide (SiC) shows a 2.5 times improvement in wear resistance and improved chemical inertness in comparison to Silicon. A thin layer of SiC can be deposited conformally over the engine at low temperature with high feature detail transfer [8].

3. 2.4 mm Engine Fabrication

3.1 Fabrication Objectives

There are three key parameters which influence the design of the Wankel rotary engine used in the MEMS REPS: system integration, fabrication, and assembly. First, the engine must allow for the integration of the electrical generator with the rotor of the engine and the stator's integration with the engine housing. In addition, the fabrication process must allow for the co-location of apex sealing components into the rotor. Precision fabrication processes must be identified such that leakage from the engine and around the apexes and rotor faces is minimized. The fabrication process must also be simple and easy to implement. The precision and simplicity of the fabrication must be balanced with engine assembly.

3.2 Design for Fabrication

Two different approaches can be undertaken in the design of the rotary engine for MEMS fabrication. In one approach, the spur gear plate and the epitrochoid housing can be combined into one piece in order to minimize leakage from the engine chamber. One difficulty in extending this design to MEMS fabrication is its reliance on timed DRIE etches and the "beaching" effect. Figure 3-1 shows the floor of an epitrochoid rising up to the epitrochoid wall like a sandy beach due to a non-uniform etch of the trench bottom near the sidewall [1]. Beaching can cause the rotor to seat improperly which will open up wider leakage paths across the rotor faces. Beaching can be minimized by lowering etch cycle pressure in the DRIE process. Unfortunately, these more uniform etches incur both low selectivity to masking materials and low etch rates which would limit engine thickness. Another difficulty in this configuration is that the fabrication process would require a self-masking fabrication process. Lateral etching of the outer walls of gear teeth would limit tooth involute resolution such that high spur gear teeth counts would not be possible [1]. The number of spur gear teeth used is important since fewer teeth will lead to less accurate rotational control of the rotor within the epitrochoid. Subsequently, the apexes of the rotor would track the outer wall of the housing less accurately.

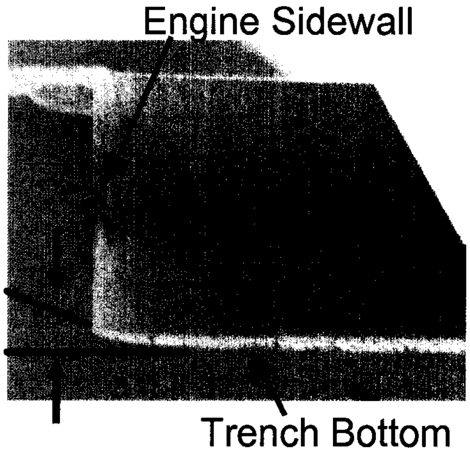

Figure 3-1. An example of beaching near the epitrochoid and trench bottom interface [1].

From a fabrication standpoint, a simpler approach is to separate the fabrication of the spur gear from the epitrochoid housing by making them separate components. The spur gear can then be fabricated in a one-mask process. The epitrochoid can be fabricated via a through wafer etch without the effect of beaching. However, this engine configuration would require assembly of the spur gear plate, epitrochoid housing, and coverplate along with the rotor and shaft. Figure 3-2 shows the cross-section of the rotary engine implemented in this design.

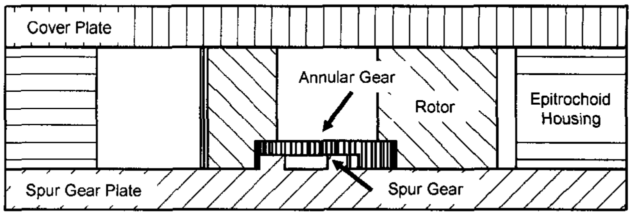

Figure 3-2. Cross-section of the MEMS rotary engine design (shaft not shown).

3.3 Housing-Rotor Fabrication

In this section, the fabrication process used to make the rotor and epitrochoid housing is described. The rotor has 3 important features: integrated in-plane cantilever apex seals, high accuracy annular gear teeth, and holes for electrodeposition of soft magnetic material. The epitrochoid housing features the intake and exhaust channels and epitrochoid.

The objective of this fabrication process is produce highly accurate engine components which will minimize leakage. A variety of different methods for fabrication were examined in order to obtain this objective. One large constraint on the fabrication process is the relatively large thickness and high aspect ratio of the engine in comparison to typical MEMS devices fabricated from Deep Reactive Ion Etching.

Instead of utilizing wafer bonding, the rotor and epitrochoid housing are fabricated using a single-sided deep reactive ion etch through a 900 μm. Misalignment of a bonded rotor by 1 μm or more would adversely affect compression and increase leakage. Two different strategies could be employed in order to etch through an entire 900 μm wafer. One method would be to etch half way through the wafer from the frontside. Subsequently, the backside of the wafer is patterned and etched until the rotors and housings are released. A similar approach was taken in the fabrication of a 1 mm thick combustor for a microfabricated gas turbine with one of the etches being isotropic [2]. The advantage of this strategy is that the vertical sidewalls of the DRIE would only need to be maintained through 450 μm rather than the entire 900 μm. However, frontside to backside lithography steps suffer from at least 1 μm of misalignment which could cause similar alignment difficulties as discussed with respect to wafer bonding. The technique employed to fabricate the rotor and engine housing was a frontside 900 μm deep silicon etch because it gave the most accurate pattern with a minimal amount of misalignment.

The rotors and epitrochoid housings are co-fabricated on the same wafer as shown in Figure 3-3. The mask layout consists of 72 8 mm by 8 mm alternating rotor and epitrochoid housing dies. Within each rotor die, nine rotors of various configurations are patterned. The nine rotors are divided evenly among 3 different annular teeth configurations: 18, 24, and 36. In addition to annular teeth variations, rotors with and without apex tip seals and holes for soft magnetic pole integration were patterned. The apex seals had three lengths (1400,

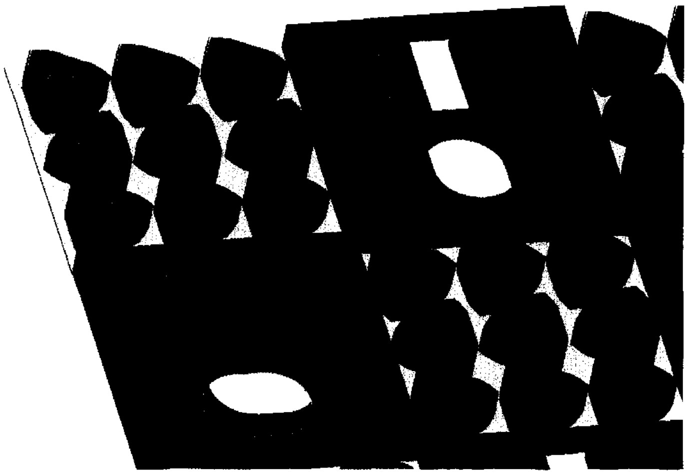

Figure 3-3. Illustration of the mask layout for the housing and rotor fabrication process.

1600, and 1800 μm) and were 25 μm wide. There were two variations in epitrochoid housings on this mask. One design consisted of a plain epitrochoid and intake/exhaust ports while the other design used exhaust recirculation and thermal isolation designs similar to those seen in Figure 2-25.

The fabrication process begins with 925±25 μm thick double-side polished 4 inch Silicon wafers. The first masking step is performed using 2.0 μm g-line photoresist. Labeling and die-scale flip chip alignment crosses and verniers for a FC150 die bonder are patterned on the wafer using a short (1-3 min) SF_6 plasma etch.

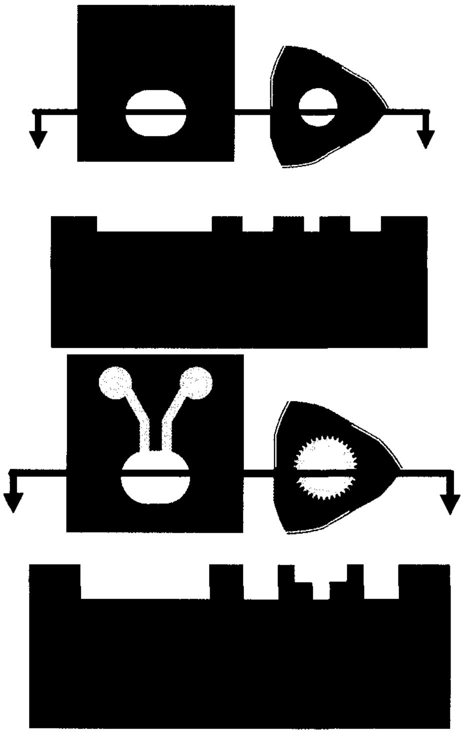

Figure 3-4. Summary of the oxide and photoresist lithography
Top. Oxide patterned for thru wafer features.
Bottom. Photoresist patterned for both thru wafer and non-thru wafer features (such as annular gear).

After stripping and cleaning the wafer, a 1.5 μm thick LPCVD SiO_2 is deposited on the wafer. The oxide layer serves as part of a dual mask etching process and as a release layer. The oxide layer is patterned using a 2.0 μm thick g-line photoresist and an anisotropic, dry oxide etch. This lithography step patterns the features which will be etched through the entire wafer as seen in Figure 3-4. After the photoresist is stripped, a 10 μm thick layer of Shipley SPR220 photoresist is coated on the wafer. The wafer is soft-baked for 10 minutes and hard baked for 2 hours at 80°C. This type of resist was chosen due to its superior selectivity during plasma etching. The resist is exposed to a pattern that includes both the through wafer features and the features which are only partially etched through the wafer such as the annular gear.

The 925 μm wafer is then attached to an oxide encapsulated handle wafer for the subsequent DRIE steps. Prior to performing any etching, a short chamber clean was performed on the STS chamber to improve run to run etch profile and rate consistency. A timed etch via DRIE of approximately 320 μm in depth is performed to define the depth of the intake and exhaust ports without removing the exposed oxide regions entirely (Figure 3-5). The wafer is then exposed to an anisotropic oxide etch which removes the remaining exposed oxide. The exposed oxide is the difference between the hard oxide mask and the photoresist mask.

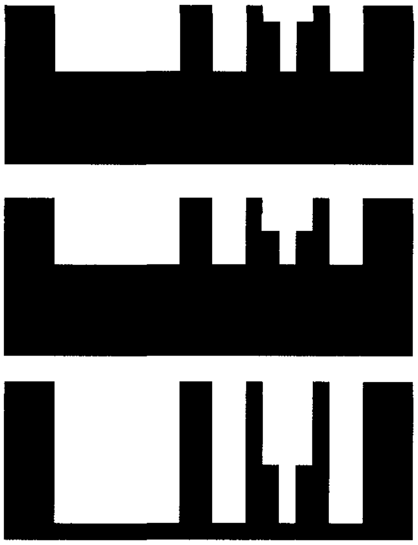

Figure 3-5. Wafer cross-section during DRIE process
Top. A 250 μm deep DRIE drives the through wafer features down
Middle. Dry oxide etch removing the exposed oxide not covered by SPR220 around the annular gear and the intake and exhaust ports
Bottom. A second DRIE drives both patterns down to the backside oxide layer.

The anisotropic oxide etch does not significantly attack the exposed photoresist. Finally, the photoresist pattern is driven down through the rest of the wafer thickness via DRIE.

The rotors and housings are released from the handle wafer by an acetone dip. The wafer is then cleaned in piranha to remove any residual adhesive that remains from the handle wafer attachment. A 1-2 minute dip in concentrated HF releases the rotors and housings from the underlying oxide layer. Figure 3-6 shows a released rotor with in-plane cantilever apex seals and holes for integrated soft magnetic material deposition placed on top of a penny.

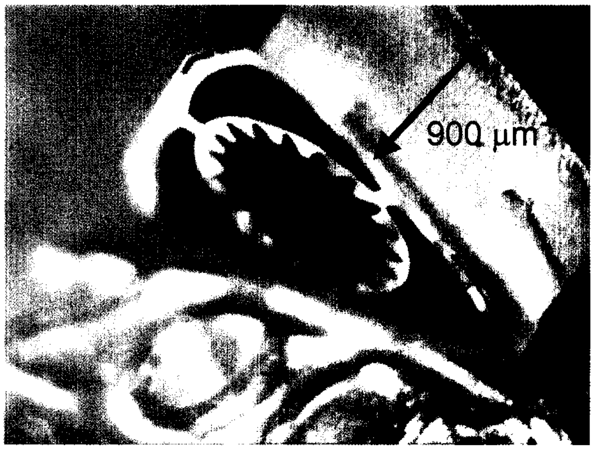

Figure 3-6. Released ~900 μm thick rotor placed upon a penny.

3.4 Spur Gear Plate Fabrication

The spur gear plate is fabricated from 4 inch 400 μm thick double side polished Silicon wafers. The first masking step is performed on the frontside of the wafer using 2.0 μm thick G-line photoresist. This mask patterns the baseline wafer-scale alignment marks used to align subsequent layers to one another. A short 1-3 minute SF_6 plasma is used to etch these features into the wafer. The photoresist is then stripped in PRS-3000 solution. Thick photoresist (SPR220) is spun on the backside of the wafer to pattern either the thru holes for intake and exhaust ports or the mounting holes for the stator

(Figure 3-7). This resist is soft baked at 115°C for 10 min and hard baked for 2 hours at 80°C. A 200-300 μm DRIE Silicon etch is performed using this masking layer.

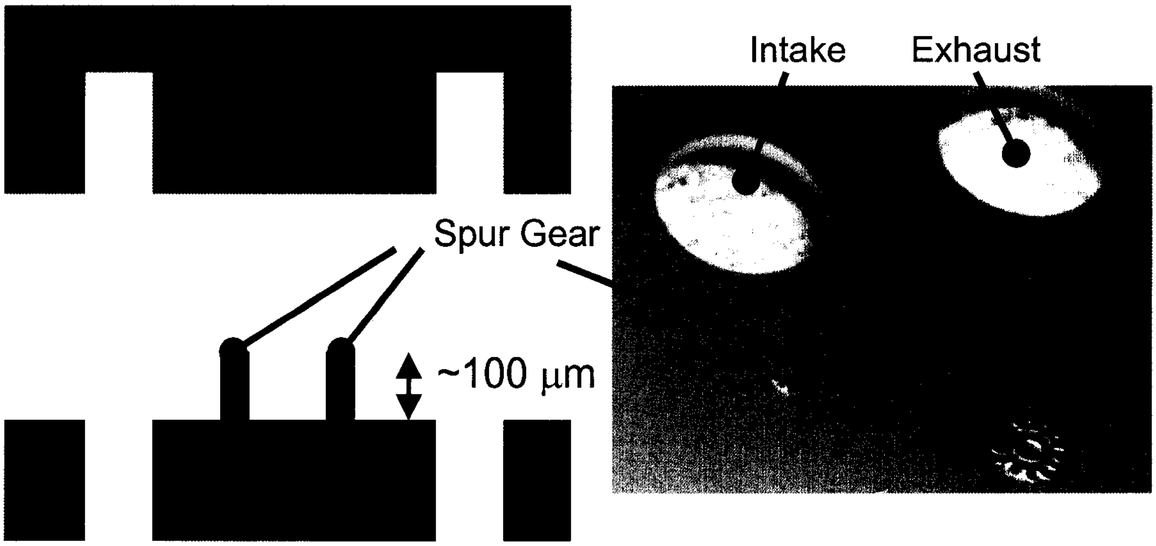

Figure 3-7. Detailed view at the two step etch process used in fabricating the spur gear plate.

The spur gear of the rotary engine is defined in the third mask of this process. 2 μm (or 4 μm) G-line photoresist is spun on the frontside of the wafer with the array of spur gears with 12, 16, or 24 teeth. A low pressure Silicon etch is used to drive the spur gear pattern into the frontside of the spur gear plate. This type of etch is necessary because this engine component must be Silicon fusion bonded (pre-bond) to the epitrochoid housing. This type of bonding is impossible without two very low roughness surfaces. The most ideal surface for this bond would be a polished wafer surface devoid of any defects or scratches. The height of the spur gear achieved in this process is limited by the selectivity of the photoresist used as the masking material. Prior to the performing frontside etching on the wafer, a handle wafer must be bonded to the backside of the wafer to prevent etching damage to the chuck from the intake and exhaust holes. Typically, an adhesive material such as photoresist, tape, or conductive glues is used to bond handle wafers to device wafers prior to DRIE process. However, redeposition of the bonding materials onto the frontside of the wafer could adversely affect the roughness of the wafer. Another less common way of handle wafer bonding is to physically bond the wafers together using a prebond. A plane Silicon wafer is bonded to the backside of the device wafer prior to the lithography steps used to define the spur gears. A piranha clean is done prior to the prebond of the wafers which cannot be performed when photoresist is on the wafer.

The final mask of this process defines the die scale alignment marks used to flip chip bond this component to the epitrochoid housing. These marks must be placed on the bonding surface which is the smooth floor defined by the previous etch. Figure 3-7 shows that the frontside of the wafer is not of a uniform height because tall spur gears and holes from the intake and exhaust ports have been defined. These features make it very difficult to conventionally spin photoresist on the wafer and have even coverage across the wafer and especially near DRIE structures. Typically, "stars" are formed from the wakes of the photoresist around DRIE features as they are spun at elevated speeds. Large pillars such as the spur gear in this case can shelter regions from being coated at all from a centrally dispensed photoresist system. It is important to note that the aspect ratio of the structures in this process have a very small aspect ratio with the majority of the exposed area not in proximity to spur gear.

A variety of methods have been explored to spin photoresist over DRIE structures. A common approach is to purchase a spray photoresist station which, when tuned properly with the correct distance from the wafer, can conformally coat the wafer with a specified thickness of photoresist. A simpler, less elegant solution is to use a pipette to add a large amount of photoresist on the wafer, entirely coating the front of the wafer. Let the resist reflow and coat the wafer completely. The I-line resist can be spun at a low speed to remove the excess photoresist and at a more elevated speed to evenly distribute the resist across the wafer (See Appendix A for details on the process). This procedure lacks a consistent, uniform thickness across the wafer that would be found in a typical dispense system. However, it does coat the wafer evenly without any uncoated areas and also protects the top surface of the gear with a thin layer of photoresist.

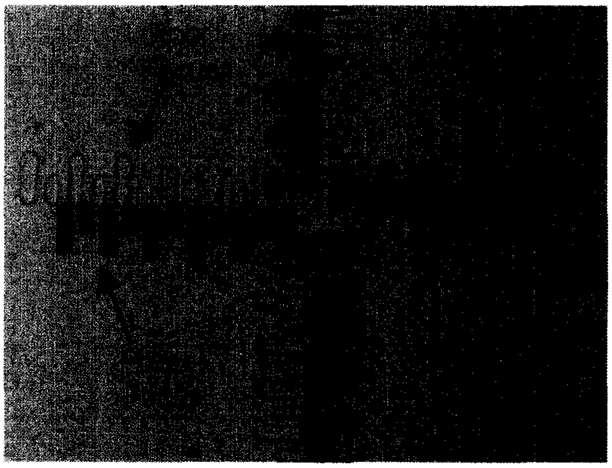

Figure 3-8. SEM of vernier scales with poor focus (outlines) as compared to vernier scales with proper focus (dark black).

The marks recommended by Suss Micotec to precisely align two dies together are a combination of crosses and precision vernier scales (Appendix C). The set of crosses is used for coarse alignment of the features while the vernier scale allows for accuracy to be reduced below a micron. Figure 3-8 shows the vernier scales exposed using 1:1 lithography and proximity mode of the Suss Microtec mask aligner with an exposure gap of 150 μm as compared to a vernier scale exposed in soft contact mode without the impediment of a spur gear. The depth of the etch which defines the spur gear results in a loss

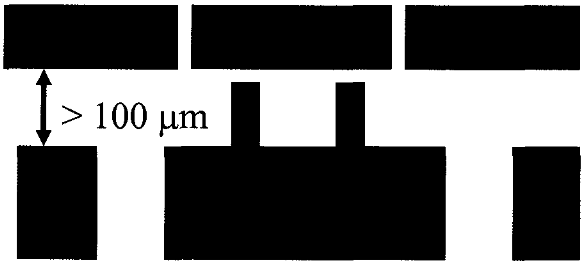

Figure 3-9. Illustration showing the focus problems with exposure of the spur gear plate after DRIE.

of focus for the subsequent mask for features at the bottom of the trench. Figure 3-9 illustrates this point with a cross-section of the wafer when it is exposed by the mask in the Suss Microtec mask aligner. The focus for this configuration is approximately at the top of the spur gear and cannot be changed for this machine. The larger features of the course alignment cross are reproduced accurately since the cross is tens of microns in size as compared to the vernier scales which are 5 μm wide. Therefore, a more accurate method of exposing the wafers can be implemented by using the GCA 10:1 wafer stepper. This machine allows for array of focus and exposures so that better resolution can be achieved at the bottom of the trench.

Once the photoresist is exposed and developed, a 1-3 minute long SF_6 plasma can be used to etch the marks into the top surface of the dies. The wafer is then coated with another layer of photoresist to protect the smooth top surface from contamination due to the dicing process. In order to dice the wafer without generating any spurs on the top surface of the spur gear plate, the wafer is placed upside down on a piece of dicing tape. The wafer is cut upside down through ¾ of its thickness. The individual dies are broken away from the wafer along the lines cut by the disco saw.

3.5 Shaft Fabrication

Fabrication of a round shaft with a length in excess of 1 mm would be difficult to fabricate. First, maintaining the vertical sidewall profile for proper seating of the cam within the rotor would be challenging. Secondly, fabrication of the cam offset to the output and rear shaft portions would require both frontside and backside etch processes. This would lead to a large amount of error in alignment.

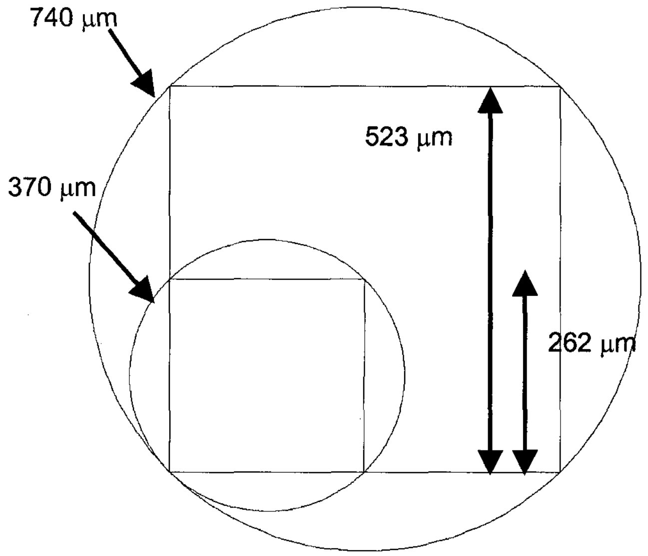

Figure 3-10. Geometry of the square shaft design as compared to a circular shaft.

Another alternative which would ease the fabrication requirements of the process would be a square shaft design. These shafts would be fabricated in the plane of the rotor instead of perpendicular to the rotor. The dimensions of the square cross-section would be dictated by circumscribing squares within the round shaft design as shown in Figure 3-10. Instead of a complex 2 side etch process thru 900 µm thickness, the shaft can be fabricated using a two-step frontside etch process thru only 523 µm which is very similar to the process used to fabricate the epitrochoid housings and rotors.

The shafts are fabricated from double-side polished 523 µm thick 4 inch Silicon wafers. The square shaft fabrication process is illustrated in Figure 3-11. Initially, 2 mm thick g-line photoresist is spun and patterned on the frontside of the wafer. This mask is used to align subsequent masks to one another as well as to label each rotor with its dimensions. These alignment marks are etched into the wafer using a short (1-3 min) SF_6 plasma.

Next, 1.5 µm of LPCVD oxides is deposited on the wafer. This oxide layer is used as a mask during the subsequent DRIE process and as a release layer after etching is completed. The oxide is patterned with an emulsion mask with features defining the

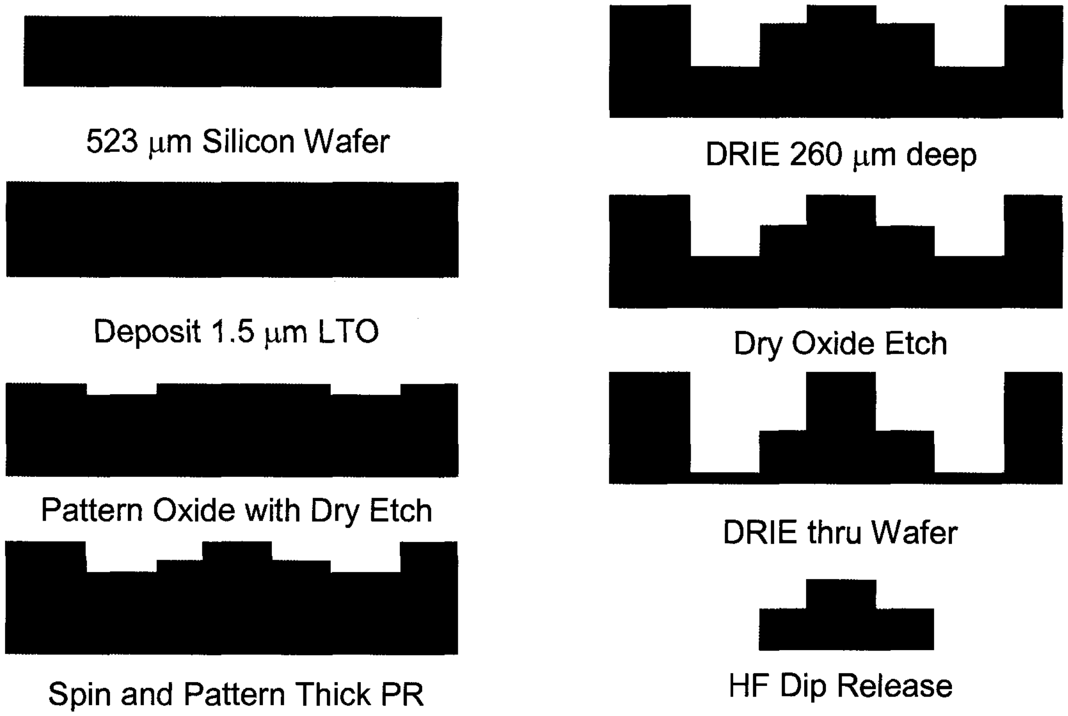

523 μm Silicon Wafer

Deposit 1.5 μm LTO

Pattern Oxide with Dry Etch

Spin and Pattern Thick PR

DRIE 260 μm deep

Dry Oxide Etch

DRIE thru Wafer

HF Dip Release

Figure 3-11. Process flow for square shaft fabrication.

entire shaft (cam, output and input) using a 2.0 μm thick g-line UV baked photoresist. The oxide is etched using an anisotropic, dry oxide etch process. The photoresist is stripped and the wafers are cleaned with piranha.

The final mask of the process defines the cam of the shaft. 10.0 μm thick SPR220 photoresist is spun and patterned. The photoresist is soft baked for 10 minutes at 115°C and hard baked for 2 hours at 80°C. Thick photoresist is used for its superior resistance to plasma and its additional thickness which is important for thru wafer etches. The device wafer is then attached to an oxide encapsulated handle wafer which is mandatory for thru wafer processes performed in the deep reactive ion etcher. Similar to the DRIE process used for the epitrochoid housings and rotors, the wafer is etched down until the remaining thickness of the wafer approximates the thickness of the output and input shafts (1/2 the wafer depth). This etch defines the exterior of the shaft. An anisotropic oxide etch is used to remove the oxide layer which protects the input and output shaft areas from the first etch. A second DRIE drives both the features defined by the oxide and the photoresist down until the underlying oxide layer is reached. This etch defines the thickness of the input and output portions of the shaft as well as the exterior portion of the eccentric cam.

A 50% CMOS grade HF solution is used to remove the shafts from the underlying oxide layer and thereby, releasing them from the wafer. A piranha clean is performed to remove any residual adhesive used in the handle wafer bonding process. The shafts are rinsed and gathered by using filter paper.

4. Fabrication Analysis

This chapter illustrates the results and highlights fabrication optimization necessary for the development of a 2.4 mm Wankel engine with integrated generator and apex seals. Particular attention is paid to the accuracy of the components fabricated including profiles generated from the deep reactive ion etching (DRIE) the rotor and epitrochoid housing, spur and annular teeth involute profiles, and surface roughness.

4.1 Housing Rotor Fabrication Analysis

The characterization of the housing rotor fabrication process can be separated into three distinct problems: development of high selectivity mask material process, development of a DRIE process with high etch rate and vertical sidewall profile, and an optimized mask layout. High selectivity mask material such SPR220 is necessary to prevent premature mask loss through the extremely long etch process necessary for 900 μm deep etch process. In conjunction with a high selectivity mask material, the etch process itself must be optimized for high selectivity to the masking material while maintaining vertical sidewall profile, and low sidewall roughness. Finally, the mask layout can have a significant impact on the local sidewall profile in areas such as the tip of the apex seal.

4.1.1 Thick Resist Characterization

In order to successfully transfer a pattern through an entire 900 μm thick silicon wafer, the masking material must be spun at a sufficient thickness and have sufficient selectivity to plasma etch processing. Research by Shipley has resulted in the development of a highly resilient photoresist material called SPR220 which was developed to have the capability for a selectivity in excess of 100:1 during plasma processing [1]. SPR220 can be spun with a thickness ranging from 1 to 10 μm. The product specifications dictate an exposure dose of 380 mJ/cm^2 when used with an I-line stepper (5 μm photoresist film thickness) and a dose of 470 mJ/cm^2 when used with a G-line stepper (7 μm photoresist film thickness). However, these particular types of lithography tools are not used for a 2.4 mm Wankel engine due to their small die size. A Suss Microtec mask aligner (MA6) tool is the primary tool used for 1:1 contact lithography. In contrast to the typical I-line stepper, the Suss Microtec MA6 tool is a broadband tool with intensity peaks at the I, G, and H wavelengths. A set of I-line filters was used to attempt to generate a pure G-line wavelength so that the specified dose could be applied. Testing with this filter resulted in underexposed photoresist even at very high exposure times.

Instead, a design of experiments was initiated in order to determine the proper exposure dose for SPR220 photoresist for this set of wavelengths. Besides exposure dose, the DOE also examined the role of time and temperature for the soft bake and the

Soft Bake Temperature (°C)	110, 115, 120
Soft Bake Time (min)	5, 7.5, 10
Exposure Time (sec)	8, 13, 18
Post-Exposure Bake Temperature (°C)	110, 115, 120
Post-Exposure Bake Time (min)	5, 7.5, 10

Table 4-1. Summary of parameters examined in the characterization of SPR220 lithography.

post-exposure bake. Proper soft bake time and temperature is important to drive off water from the photoresist prior to exposure. After exposure, a hold time of at least 35 minutes is recommended so that water can diffuse back into the thick photoresist so the photo-reaction can be completed [1]. A post-exposure bake is performed after exposure to improve the resist profile by removing any ringing of the exposed light. Table 4-1 summarizes the range of values examined by the 32 wafer DOE. The DOE sought to minimize difference in line width between the top of the photoresist and bottom of the photoresist for 10 μm lines in order to generate photoresist patterns with straight sidewalls.

Soft Bake Temperature (°C)	120
Soft Bake Time (min)	10
Exposure Dose (mJ/cm2)	222
Post-Exposure Bake Temperature (°C)	120
Post-Exposure Bake Time (min)	6.5

Table 4-2. Optimal process parameters for ~10 μm thick SPR220.

Figure 4-1. Wafer topography causes focus and exposure issues for SPR220 on patterned oxide.

Table 4-2 summarizes the optimum parameters for the generation straight sidewall 10 μm thick photoresist. Full results of the DOE can be found in Appendix B. Table 4-2 differs somewhat from the DOE indicated values due to the effect of focus which could not be examined by the DOE. However, the actual substrates used for patterning device wafers have topography due to an oxide etch. Typically, 1.0-1.5 μm oxide is used as a masking layer. Thick photoresist located above the exposed silicon is at an entirely different focal plane than the photoresist on the oxide layer (Figure 4-1). The result of the height difference in these two areas of the wafer is incomplete exposure of the photoresist located on top of the exposed silicon substrate. Focus of the mask aligner is fixed so this difference can only be adjusted through an increase in exposure time. As a result, photoresist above the oxide layer appear to be slightly overexposed.

4.1.2 DRIE Characterization for 900 μm Deep Structures

The most common method utilized for deep anisotropic etching of Silicon for MEMS devices is based on a patented process developed by Robert Bosch [2]. The Deep Reactive Ion Etching process relies on fluorine radicals generated in a Sulfur Hexaflouride (SF_6) plasma to remove silicon. High density SF_6 plasma is provided via Inductively Coupled Plasma in order to obtain a sufficient number of free radicals for etching. Sidewall passivation is provided by a conformal deposition of a fluorocarbon generated by a Octofluorocyclobutane (C_4F_8) plasma. Cycling of etch and passivation steps generates high rate, anisotropic etching of a silicon substrate. The ability to use silicon oxide, silicon nitride and photoresist as masking materials for this etch process gives compatibility with typical MEMS processes.

The UC Berkeley microfabrication laboratory uses a Surface Technology Systems (STS) Advance Silicon Etch (ASE) machine for deep silicon etch processing. The STS DRIE tool features inductively coupled plasma at 13.56 MHz with impedance matching and power control on a coil above the chuck. An electrostatic chuck is used to secure a

4 inch substrate within the chamber after loading through a manual loadlock. Independent energy control is provided a 13.56 MHz biasing of the platen via impedance matching and automatic power control. Wafer cooling is provided by a chiller and aided by a helium flow across the backside of the wafer. The chamber lid temperature is maintained at 45°C.

Three parameters are examined for the characterization of the STS ASE machine for 900 µm thick etching are a vertical sidewall profile, trench wall roughness, and mask selectivity. As discussed earlier, a vertical sidewall profile is necessary to minimize leakage paths around the apex seal. For the purposes of this analysis, sidewall profile is defined as the difference between the widest portion (L_w) of the trench width and the trench width at the mask level (L_m) as seen in Figure 4-2. Similarly, large scallops on vertical sidewalls could also act as a leakage path. A high selectivity process is necessary to prevent significant erosion of the oxide and photoresist during the long duration of the etch. A number of previous studies have indicated that four process parameters control these effects: platen power, pressure, process gas flows, and etch and passivation cycle times [3, 4].

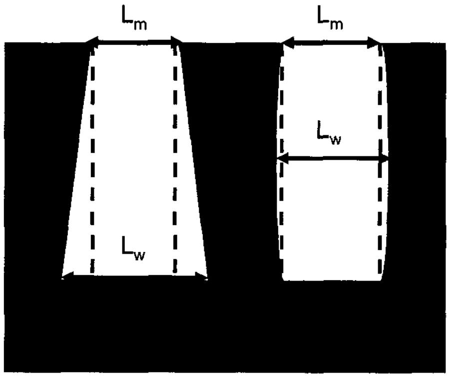

Figure 4-2. Sidewall profile definition for a reentrant trench profile (left) and a bowed trench profile (right).

This study examined the effect of three parameters: pressure of the etch step, platen power, and etch and passivation cycle times. These are the ideal parameters to examine for vertical, 900 µm deep trenches with low sidewall roughness. Process pressures ranged between 25 mT and 45 mT and were controlled by a fixed pressure control valve angle (APC). Previous studies indicate that high process pressures improve mask selectivity [9]. Platen powers were varied between 10 and 15 Watts. Platen power was used to adjust the sidewall profile to improve verticality. Sidewall surface roughness is highly dependent on the ratio of etch to passivation cycle times. Table 4-3 summarizes the DRIE process parameters used for this study.

	Passivation	Etch
Coil Power (W)	600	600
Platen Power (W)	5	10-15
SF6 Flow (sccm)	0	90
O2 Flow (sccm)	0	8
C4F8 Flow (sccm)	52	0
APC Angle	68-77	68-77
Cycle Time (sec)	6-7.2	10-12

Table 4-3. General gas flow and RF power parameters.

Table 4-4 shows a summary of the primary effects of these parameters on the goals of the 900 μm DRIE. It should be noted that uniformity is improved with increasing platen power at high process gas flows. This is a second order effect [4].

Parameters	**Pressure ↑**	**Platen Power ↑**	**Time Ratio ↑**
Selectivity	+	-	-
Etch Rate	+	+	+
Sidewall profile	less reentrant	more reentrant	more reentrant
Scallop size	0	0	+
Uniformity	-	-	0
Grass Formation	+	-	-

Table 4-4. Summary of observed effects for high thickness etching.

4.1.3 Results of 900 μm DRIE Characterization

The first objective of the 900 μm etch characterization is to obtain etch parameters which would have a sufficient mask selectivity. An analysis of the effect of pressure on selectivity was performed and the results are shown in Figure 4-3. High pressure DRIE recipes produced a maximum oxide selectivity in excess of 350:1 and photoresist selectivity greater than 150:1. Resist and oxide thickness were measured optically while trench depths were measured using a white light inferometer. These results indicate pressures greater than 35 mT are necessary for 900 µm deep etches with sufficient mask selectivity. Scanning Electron Micrographs (SEMs) were performed on cross-sections of each wafer which showed that high pressure recipes gave a more vertical sidewall profile. Low pressure recipes resulted in trapezoidal shaped, reentrant cross-sections and extreme undercuts of the surrounding structures (Figure 4-4). A high process pressure caused a bowed sidewall profile which is typically widest at a trench depth

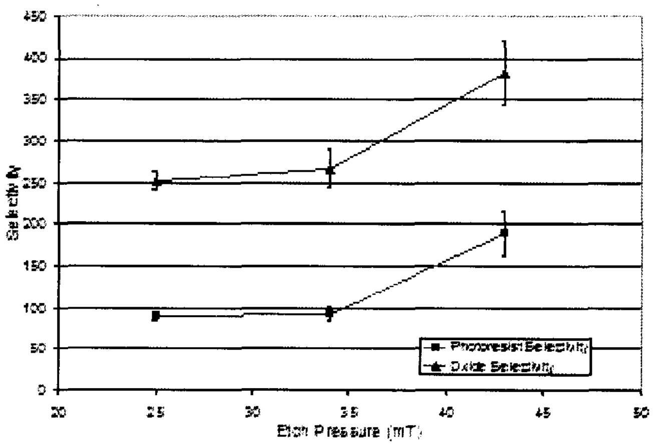

Figure 4-3. Effect of pressure on selectivity with a platen power of 12 W, 10 second etch cycle time, and 6 second passivation cycle time.

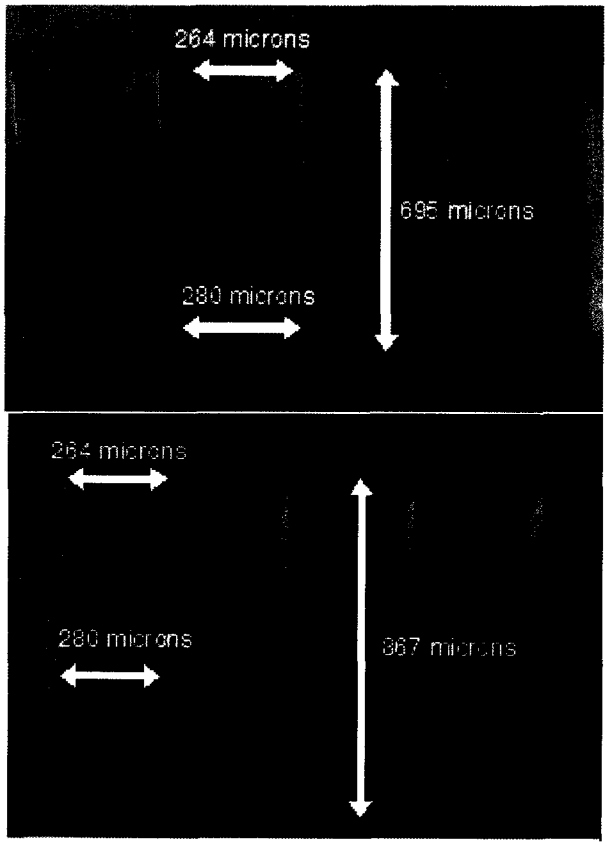

Figure 4-4. Examples of two different sidewall profiles due to variable etch pressure. Above, a reentrant profile results from an etch performed at 25 mT. Below, a slightly bowed trench results from a high etch pressure of 43 mT.

of approximately 450 μm. Results for sidewall profile are summarized in Figure 4-5.

One effect that can be seen clearly in Figure 4-4 is the phenomenon is "grass" or black silicon. The term, "grass", is used to define thin stalagmites of silicon which are located on the bottom of an etched trench. It has been established previously that the phenomenon of grass is dependent on pressure due to the re-deposition of masking material within trenches causing local micromasking. Some previous research indicates a cutoff in APC angle of 75° above which grass is formed [3]. However, an absolute cutoff in APC may not accurately define the process space within which grass is developed. Since grass is dependent on pressure, process gas flow will also affect grass growth. In addition, grass growth has

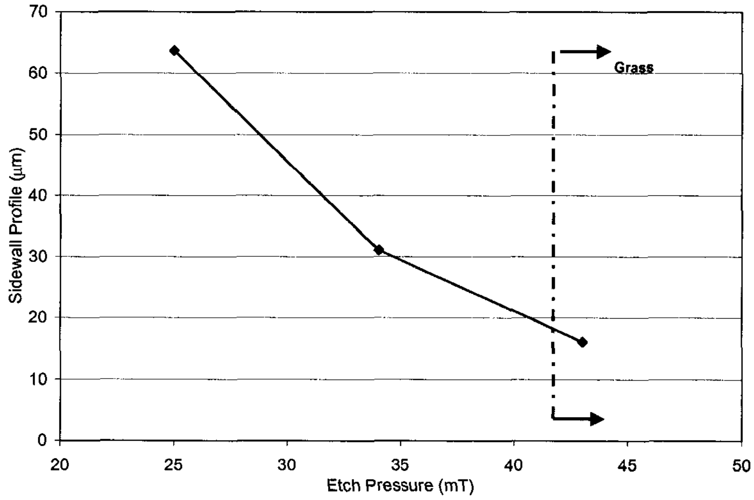

Figure 4-5. Effect of pressure on sidewall profile with a platen power of 12 W, 10 second etch cycle time, and 6 second passivation cycle time.

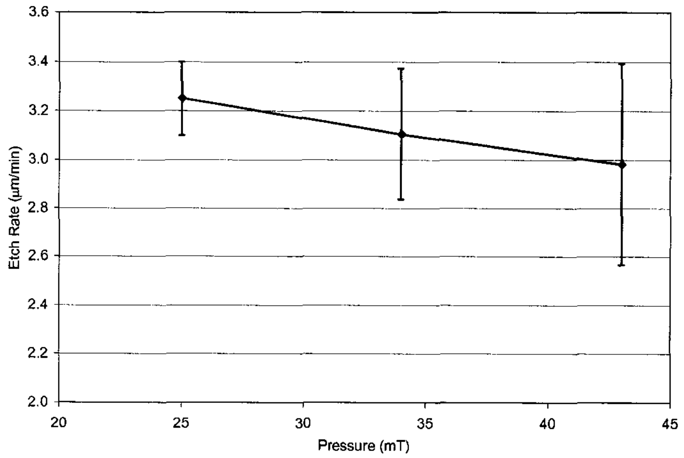

Figure 4-6. Etch rate analysis showing uniformity for a platen power of 12 W, 10 second etch cycle time, and 6 second passivation cycle time.

been observed to increase with platen power, and cycle time ratio. The pressure of a particular recipe can vary with the amount of Teflon and other deposits on the sidewall of the chamber. The formation of grass was found to be most significant in the center of the wafer and generally moved out radially due to etch rate non-uniformity called the "bullseye effect". The bullseye effect is characterized by outer portions of the wafer etching at a faster rate than the wafer center due to a higher concentration of available ions. For features etched through the entire wafer thickness, grass formation at the bottom of a trench is not a significant issue. However, some grass that forms near the sidewalls can develop into large wall growths. The grass formed on the features such as the annular gear or the intake and exhaust ports could be a potential source of silicon debris inside the engine. This is due to the fact that these trenches are not etched through the entire wafer so the grass is not eliminated.

	Reduced Cycle Time	Reduced Platen
Sidewall Profile (μm)	15	11
Oxide Selectivity	303	368
Selectivity	124	125

Table 4-5. Summary of the effect of platen power and cycle time on sidewall profile and selectivity.

Another effect of increasing pressure is an increase in the non-uniformity across the wafer. Figure 4-6 shows etch rate as a function of pressure with non-uniformity. Etch rate was measured during the first 300 μm of the etch. Accurate measurements of trench depth during the later portions of the etch process were not possible with the white light inferometer. Scattering by the grass at the bottom of the trench resulted in a minimal amount of reflected light from which to perform a measurement.

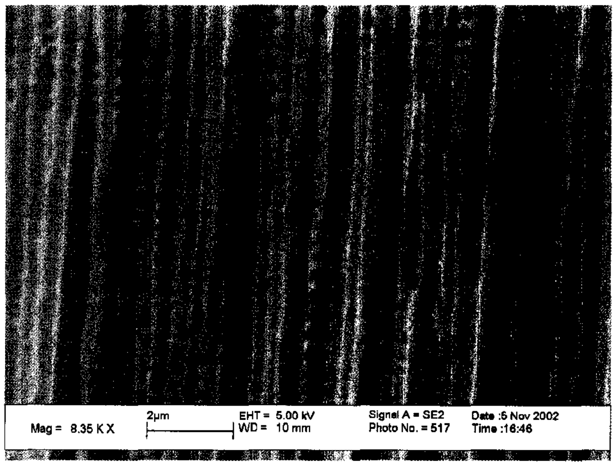

Figure 4-7. Wall roughness of engine housing etched at 43 mT etch pressure, 12 W etch platen power, 10 second etch cycle time, and 6 second passivation cycle time.

	Passivation	Etch
Coil Power (W)	600	600
Platen Power (W)	5	10
SF6 Flow (sccm)	0	90
O2 Flow (sccm)	0	8
C4F8 Flow (sccm)	52	0
APC Angle	77	77
Cycle Time (sec)	7.2	12

Table 4-6. Final process parameters for ultra-thick DRIE.

In order to remove the slight bowing of the vertical profile, adjustments to the platen power and cycle time ratio were made. Table 4-5 shows that a 2 W reduction in platen power resulted in a 38% improvement in sidewall profile over the results shown in Figure 4-3. Reduction in the cycle time ratio did not produce a marked effect on the sidewall profile. The final objective for this process optimization is improved surface roughness. Figure 4-7 shows the sidewall of the epitrochoid etched. Scallops formed on the sidewall of the trench were well less than a 1 µm in size. Table 4-6 shows the optimum parameters for ultra-thick DRIE etching.

4.1.4 Apex Seals

Initial fabrication of 900 µm thick Silicon rotors only yielded apex seals with total thickness of 400-500 µm. Process parameters which resulted more reentrant profiles limited the apex seal thicknesses to 100 µm. Figure 4-8 shows a SEM of two different rotors with undercut apex seals located on the same die. Figure 4-9 shows a head-on

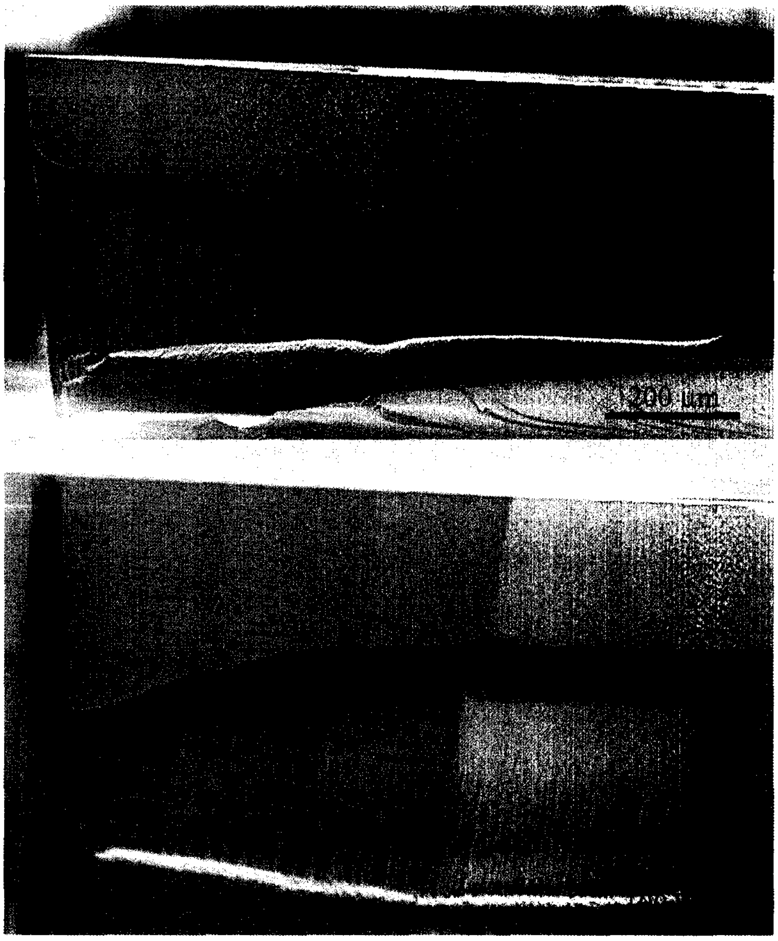

Figure 4-8. Undercut apex seals for two different rotors located on the same die.

view of the cross-section of one of these apex seals. From the characterization of the DRIE process, it would be expected that none of the 25 μm apex seals would have been undercut because the maximum undercut developed from the bowed trenches would be approximately 16 μm. Throughout the characterization process, apex seals even on the same dies would not look identical. These unexpected variations in the apex seals are the result of two effects: Aspect Ratio Dependent Etch (ARDE) and mask design.

As trench width is increased, the sidewall profile of the trench becomes more reentrant. Figure 4-10 shows this effect for a variety of trenches with widths varying from 25 to 300 μm. All trenches measured exhibited a bowed sidewall profile. This effect becomes especially relevant when examining the large (500 μm), uneven trenches adjacent to the apex seal or on the sidewall of the epitrochoid when etched as a large hole (see Figure 3-3). The fact that the trenches adjacent to each rotor are not standardized results in difference in apex seal profiles seen in Figure 4-8.

An equally important impact in successful fabrication of the integrated apex seal is effect of ARDE on etch rate. ARDE is characterized by wider trenches etching at a higher rate than narrower trenches. This effect is even more pronounced at higher pressures where lag between trenches has been measured to be as much as 100 µm. The thin trenches which define the apex seal were not completely etched through the wafer because of ARDE.

Figure 4-9. Cross-section of an undercut apex seal.

One method that can be used to overcome this effect would be to utilize a backside etch to help the more narrow trenches overcome ARDE. Since the narrow trenches do not define the exterior of the rotor but rather the apex seal interior, any

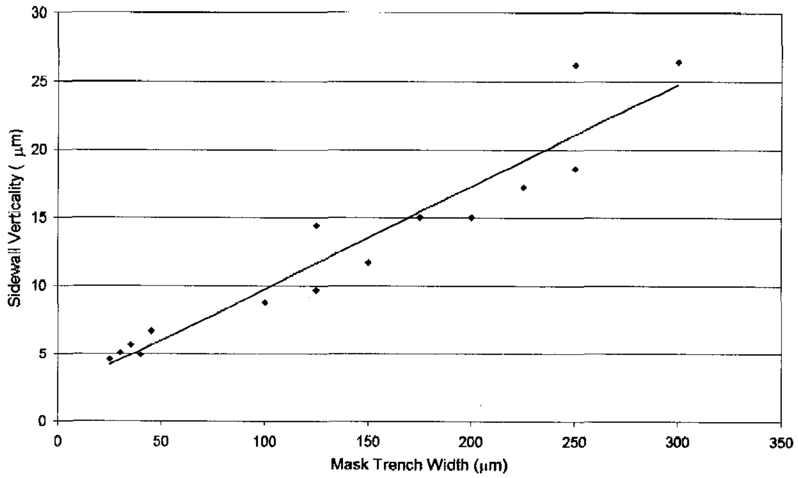

Figure 4-10. Sidewall profile of a series of trenches 25 to 300 µm in width.

backside lithographical misalignment will not cause undue mismatch between the outer portion of the rotor and the epitrochoid housing. However, any alignment error of the backside trench will still affect the stiffness of the apex seal.

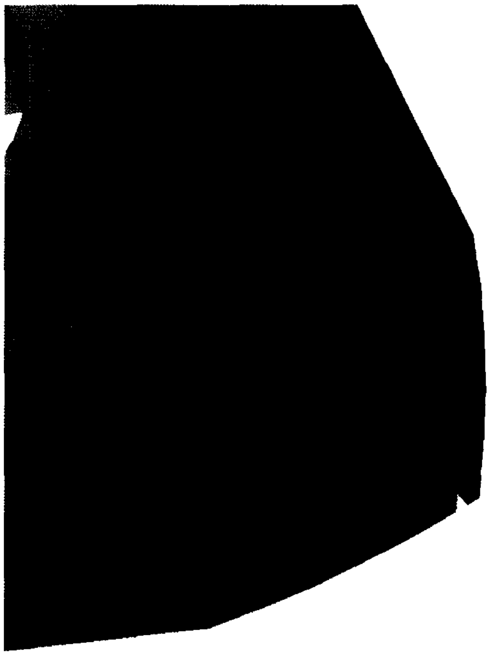

Figure 4-11. Sketch showing the effect of the apex seal tip being "pinched" off from the surrounding trenches.

One of the most important aspects of the apex seal fabrication is maintain a vertical profile of the apex tip since it will be in contact with the epitrochoid housing during engine operation. From a mask design standpoint, the profile of the tip is difficult to maintain because the end of the apex is being attacked from two directions as seen in Figure 4-11. Generally, a point or small surface that is exposed to wide-open area during a DRIE process will tend to have a more reentrant profile because the point or surface sees expansive trenches from multiple angles. Figure 4-12

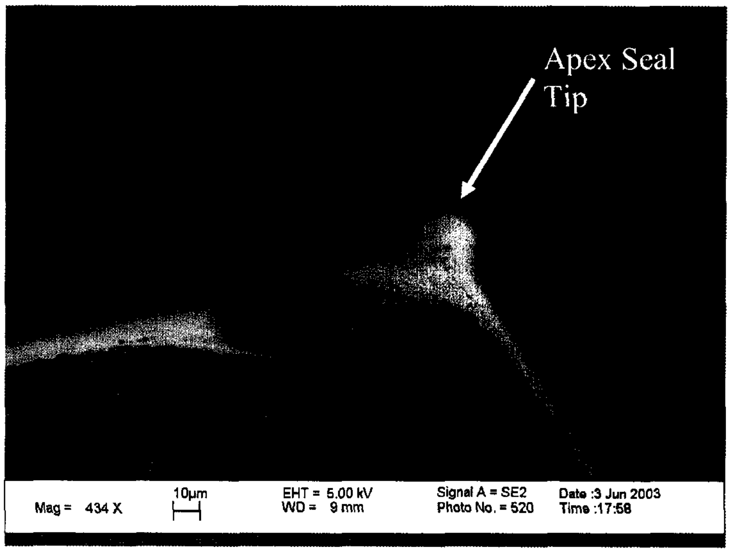

Figure 4-12. Incompletely etched rotor viewed upside down for perspective on reentrant profiles at the apex tip.

shows a rotor viewed upside down which shows how expansive trenches can cause a reentrant profile at the apex tip.

4.1.5 Annular Gear Teeth Analysis

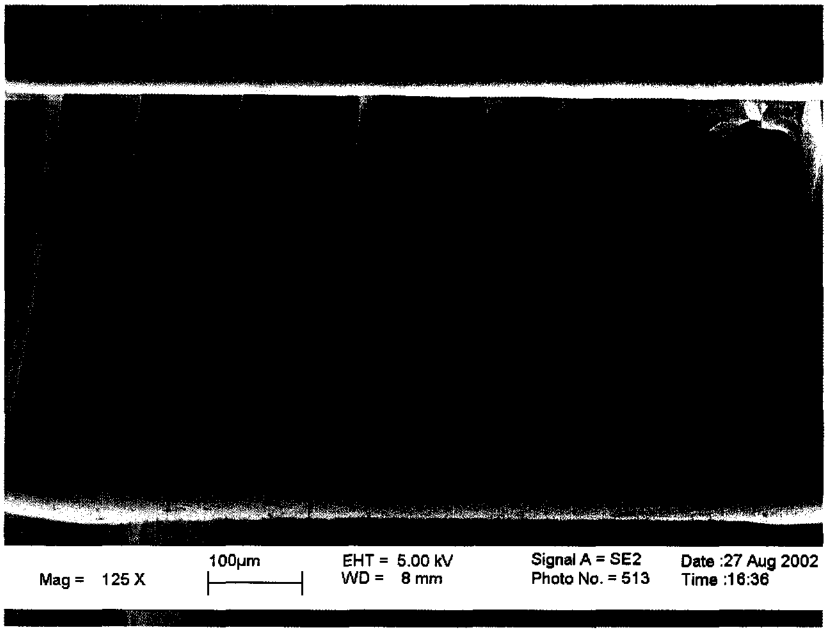

Figure 4-13. Cross-section of an 18-tooth annular gear.

Figure 4-13 shows a cross-section of the annular spur gear from a cleaved rotor. The SEM clearly shows the annular gear teeth becoming more reentrant as the etch is progressing. This is similar to the effect seen at the apex seal tips described in the previous section. Since the addendum circle of the annular gear has a diameter of 620 µm, the top land of the tooth is reentrant due to the expansive trench. The tips of the annular gear teeth are pinched from the two adjoining trenches similar to the effect seen at the apex seal tips. These effects result in a non-uniform contact between the spur gear and annular gear. However, the tightest fit between the two sets of gear teeth will occur at the base of the spur gear and the mask side of the annular gear (upper portion of Figure 4-13). The difference between the spur gear tooth profile and the annular tooth profile increases from this point due to the reentrant trench profile.

In order to examine the accuracy of the upper portion of the annular gear tooth, Figures 4-14 and 4-15 show top views of 24 and 36-tooth annular gear with the corresponding overlaid mask design. There is approximately 95% agreement between the desired involute profile and the annular gear tooth profile at the uppermost portion of the trench for the 24-tooth annular gear tooth. Some error can be found at the very tips of the annular gears due to a limit in the resolution of the thick photoresist. This error becomes more prominent for the 36-tooth annular gear due to its small tooth size.

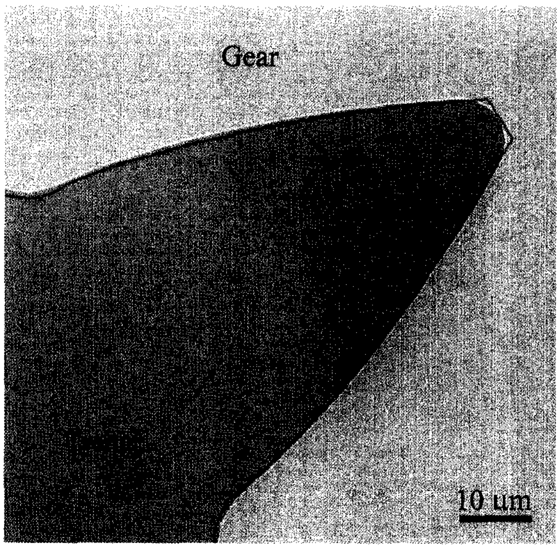

Figure 4-14. SEM of an annular gear tooth of a 36-tooth gear overlaid with the corresponding mask

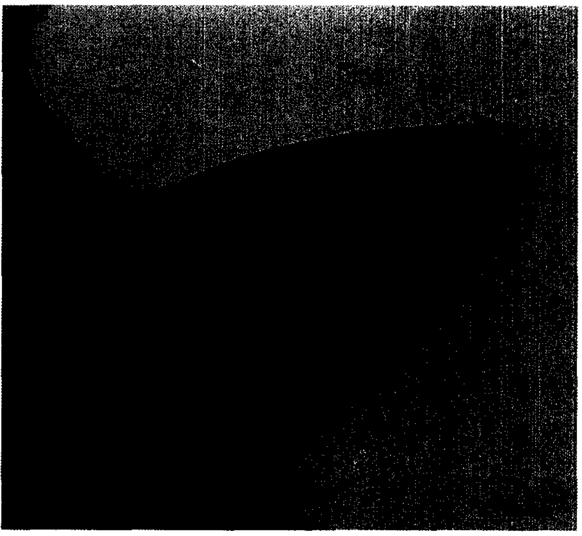

Figure 4-15. SEM of an annular gear tooth of a 24-tooth gear overlaid with the corresponding mask design.

4.2 Spur Gear Plate Fabrication

One novel aspect of the engine design is the assembly of the spur gear plate to the epitrochoid housing. Typically, two die-size silicon components are bonded using an adhesive. However, the high temperature of the engine housing will undoubtedly cause the adhesive to fail. Instead of using an adhesive, the engine assembly process is based on the pre-bond of the spur gear plate to the epitrochoid housing. Normally, the bonding surfaces of both components would be the polished face of the silicon wafer but in this case, the front surface of the spur gear plate must define the spur gear teeth. The technical difficulty of this approach is the frontside etch of the spur gear. In order for the two die-scale components to successfully pre-bond, the frontside of the spur gear plate must have a low surface roughness. Simultaneously, this etch must maintain a vertical sidewall profile for the spur gear teeth with excellent detail transfer of the involute profile while maintaining a sufficient mask selectivity.

4.2.1 DRIE Characterization

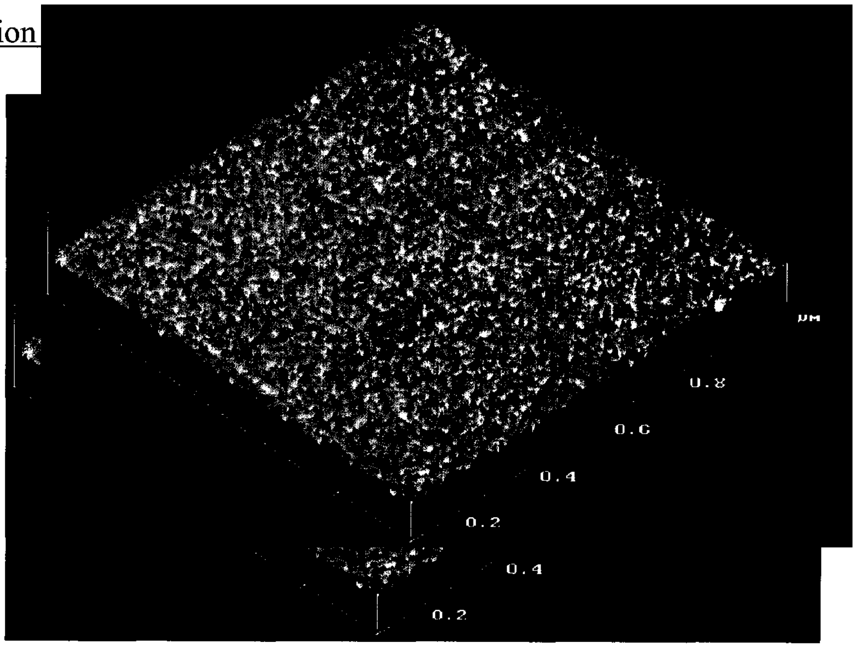

Figure 4-16. Atomic Force Microscope of a 1 µm by 1 µm square area on a clean, polished wafer. The range of the plot in the Z-direction is 100 nm.

There are three main surface forces which can affect to formation of a pre-bond between two Silicon surfaces: Van der Waals, electrostatic, and capillary. These forces can be affected by both the roughness of the bonding surfaces and surface preparation prior to bonding [5]. Figure 4-16 shows a measurement of the surface roughness of a clean, polished 4 inch p-type wafer. The RMS roughness of this area was measured to be 11.3 Angstroms. This wafer is typical of standard polished wafers commonly used for wafer bonding. Other researchers have demonstrated that an RMS roughness of 5 Angstroms or less is adequate for bonding of wafers at room temperature [6].

Typically, lowering pressure for a DRIE recipe will result in smoother, higher quality surfaces at the bottom of trench (Table 4-4). As seen in the housing-rotor fabrication, a higher process pressure can cause grass and other redeposition/micro-masking effects which will result in a jagged trench bottom. Lower pressure etches are characterized by atoms hitting the trench bottom at lower velocities and less frequently. This results in a lower etch rate but better cross wafer uniformity due to a decrease in the bullseye effect. The trade-off of a smoother, more uniform etch at lower pressure is selectivity. A decrease in etch rate results in increased etch duration which increases the amount of ion bombardment on the surface of the masking material. Low process pressures have been used for micro-mirrors for optical switches and DRIE of quartz with 2 nm RMS roughness [7, 8]. It has also been demonstrated that oxygen content either derived from the masking material (such as oxide) or added to the process as diluents can significantly increase the surface roughness [9].

Table 4-7 shows the DRIE process parameters for the frontside etch of the spur gear plate. Table 4-8 summarizes the results of these etches in terms of roughness. Roughness was measured using a Veeco white-light

	Passivation	Etch
Coil Power (W)	600	600
Platen Power (W)	0	12
SF_6 Flow (sccm)	0	130
O_2 Flow (sccm)	0	13
C_4F_8 Flow (sccm)	85	0
APC Angle	52	52
Cycle Time (sec)	7	9

Table 4-7. Process parameters for a low roughness etch.

inferometer and three measurements were made in the center of the wafer and averaged. R_a is defined as the arithmetic mean of the height over the selected area. R_q is defined as the root mean squared roughness of the selected area and generally used for optical surfaces. These two results do not put much weight on any abnormalities on the surface such as bumps or debris. Bumps and other imperfections could prevent bonding of the surface due to voids or lack close contact for the intermolecular forces necessary for bonding.

	Average Roughness, R_a (nm)	RMS Roughness, R_q (nm)	Max Roughness, R_z (nm)	Ten-Point Roughness, R_t (nm)
Unetched Silicon Wafer	4.0	4.9	29	31
Blanket, Etched Silicon Wafer	4.4	5.6	32	34
Patterned, Etched Silicon Wafer	4.6	5.8	57	116

Table 4-8. Comparison of roughness between polished and etched wafers.

On the other hand, R_t and R_z give a better sense on the overall range of heights in a given area. The value of R_t is given by the total maximum height difference of the area of interest while R_z shows the ten-point height of the region which is an average of the five greatest peak to valley separations. While the RMS roughness values for all of the wafers are very similar, the maximum

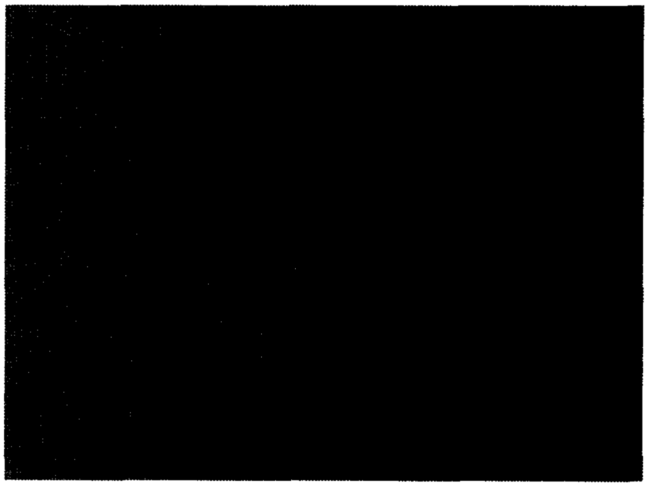

Figure 4-17. Debris from the photoresist patterning process causes local micromasking during the subsequent DRIE. These bumps are up to 1 μm tall.

roughness and the ten-point height show that the wafers with photoresist pattern tended to have more and larger bumps on the surface. Figure 4-17 shows that the debris or redeposition of the masking material during the etch process is causing local bumps on the wafer which can be as high as 1 μm.

Bonding tests were performed for a plain silicon wafer etched with a low pressure recipe. These wafers were hand bonded after a piranha (H_2SO_4:H_2O_2, 5:1) cleaned twice. In comparison to an RCA1 clean, piranha reduces metal contamination while not microroughening the silicon surface which can occur when NH_4OH is in contact with bare Silicon during a standard RCA1 cleaning [5]. Bonding of these wafers and portions of these wafers were successful. In addition, an etched spur gear and epitrochoid housing were manually pre-bonded together in order to prove the validity of the bonding process. However, these pieces were not aligned to one another accurately.

4.2.2 Spur Gear Teeth Analysis

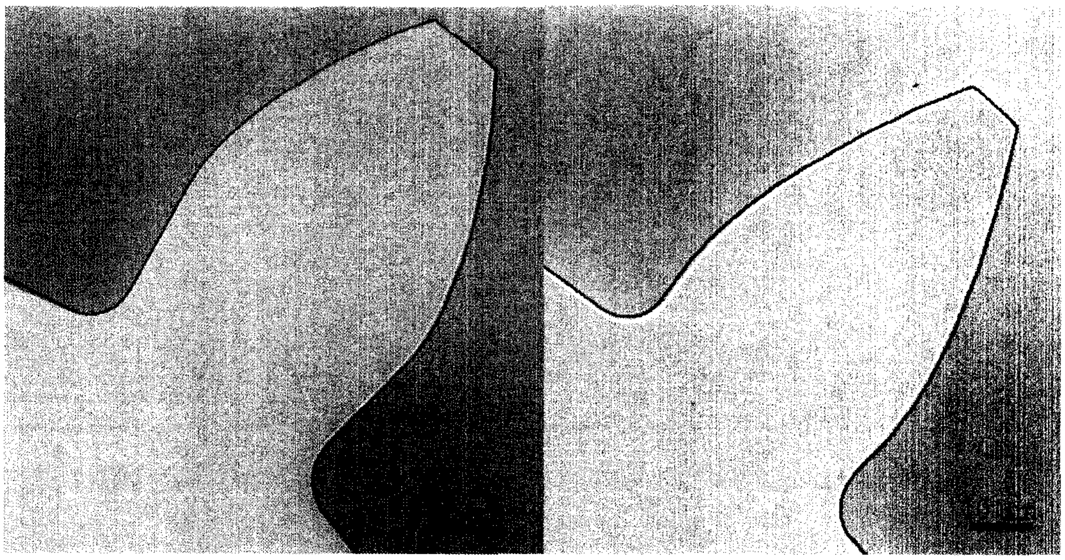

Figure 4-18. Comparison of spur gear tooth involute profile for a 12-tooth spur gear (left) and 24-tooth spur gear (right).

Involute profiles of the spur gear teeth are important for rolling motion without slipping during gear mesh. The profiles of the gear teeth were examined in a Scanning Electron Microscope (SEM) and images of the gear teeth were matched with mask designs used to generate the involute profiles. Figure 4-18 shows an overlay of the mask design on an actual spur gear tooth for both a 12-tooth and a 24-tooth spur gear. As the number of teeth of the spur gear increases, the width of the tooth decreases. The majority of the error between the mask and the actual tooth can be found on the corners at the end of the tooth as seen in Figure 4-19. Spur gear tooth error was determined by comparing the width of the tooth at its widest to that of the mask design. For each design, the error in the involute profile was less than 1%. In addition to the 12, 18, and 24-tooth spur gear designs, a spur gear with 50 teeth each approximately 17 μm wide was also fabricated to examine the limits of spur gear tooth resolution. Figure 4-20 shows one of these teeth with the

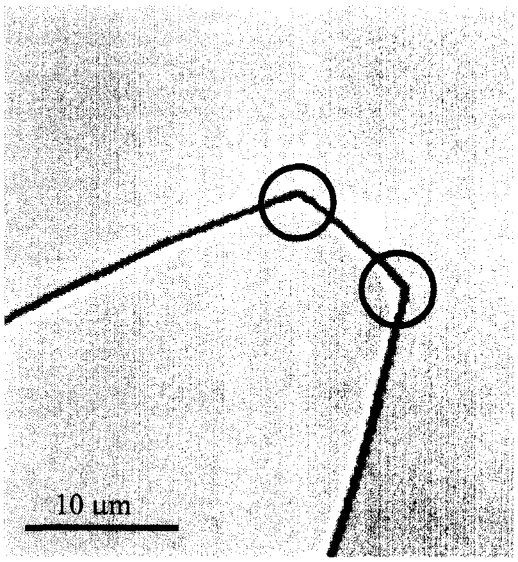

Figure 4-19. Lateral etching at the tip of a 24-tooth spur gear.

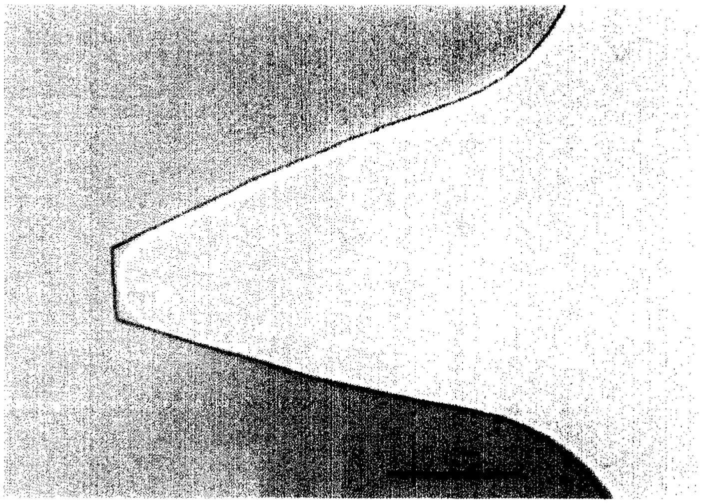

Figure 4-20. A 50-tooth spur gear as compared to its designed involute profile.

overlaid involute mask profile. The top of the gear tooth is laterally etched away 2 μm on either side which could be attributed to lithographical limits of the 1:1 mask aligner and the small tooth topland.

One of the overriding objectives of this fabrication process was to remove footing at the base of the gear and improve the number of teeth that can be fabricated for a MEMS Wankel engine. In addition, Figure 4-21 shows that the "beaching" effect at the base of the spur gear is not existent. This outcome stands in marked contrast to the spur gear results for 1 mm size Wankel engines reported by Fu [10]. This is primarily attributable to the low pressure recipe used to create a smooth, bondable surface on the spur gear plate. Lower pressure during DRIE improves uniformity both across the wafer and locally by reducing the affect of ARDE. Figure 4-21 does show some roughness on the sidewall of the tooth but this roughness changes the involute profile by less than 100 nm.

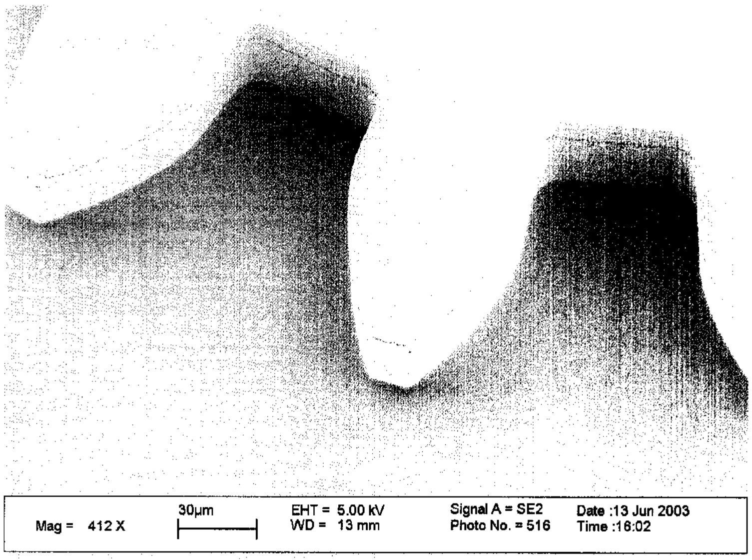

Figure 4-21. Perspective view of 16-tooth spur gear teeth.

4.3 Shaft Fabrication Analysis

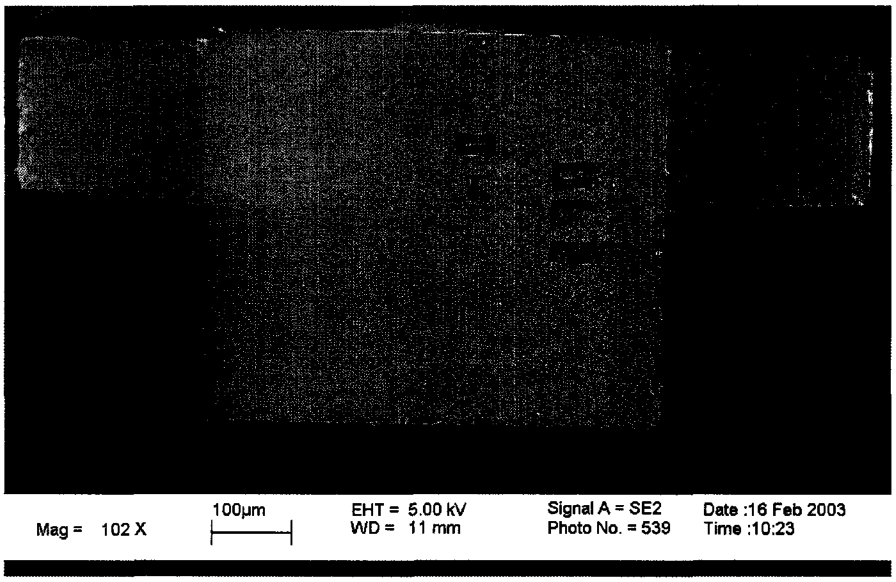

Figure 4-22. Top view of silicon square square shaft.

Fabrication of a 1 mm long, 500 mm thick square shaft was demonstrated in a three mask, two etch process. Initially, the layout for the square shaft design was based on a clear field or emulsion mask. This allowed for a very simple mask making process since the features on the emulsion mask consisted entirely of simple shapes such as squares or polygons. An emulsion or clear field mask removes all photoresist on the wafer except in the area of interest such as the cam or the shaft profile in this case. This exposes almost the entire mask to the SF_6 plasma during the deep reactive ion etching process. Since etch rate is dependent on the amount of area exposed by the mask during the etch process, a very slow etch rate (less than 1.0 μm/min) was observed even for high pressure recipes similar to those used for the epitrochoid housings or rotors. These slow etch rates led to a reduction in the selectivity of the etch process due to the long duration of shaft etch. A chrome mask layout was then designed with a limited number of device dies to protect up to 50% more of the wafer surface during the etch process.

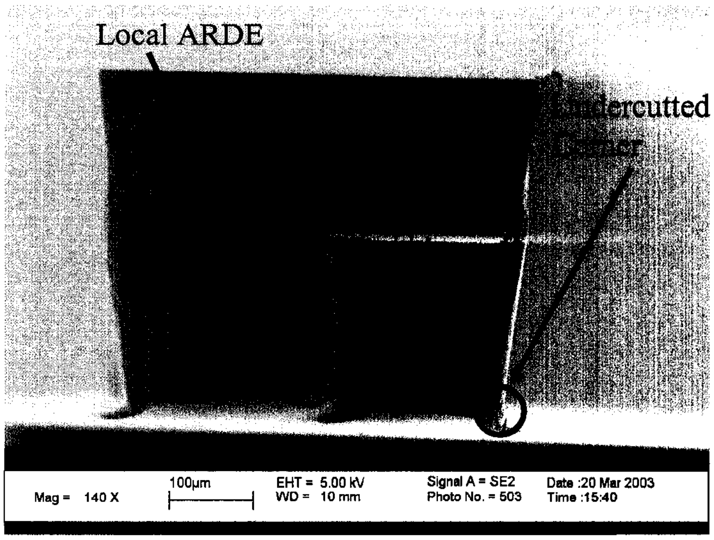

Figure 4-23. Unreleased square shaft exhibiting local non-uniform etching due to ARDE and undercut corners.

Figure 4-22 shows a released square shaft fabricated in a two-step etch process using chrome masks. The shaft fabrication process suffers from poor sidewall straightness, local ARDE effects, and oxide release issues. Figure 4-23 exhibits two of these effects. First, corners at the intersection of the output or input shaft with the cam etch at a slower rate than other portions of the shaft geometry. This is analogous to the difference in etch rate between two trenches of differing width. This effect causes some fillets of silicon to remain in this area even when the shaft is released. Similar to what was seen in the rotor fabrication process, the sharp corners of the shaft become undercut by a reentrant trench due to their exposure to expansive trenches on either side. Finally, as the etch process approaches completion, there is a premature release of the shaft from the underlying oxide films dependent on the degree of non-uniformity across the wafer. The oxide film underneath the shaft, once penetrated or cracked by the SF_6 plasma, peels away from the adhesive used to glue the device wafer to the handle wafer due to the compressive stress of the underlying LTO. The peeled oxide layer generally starts at the outer portion of the wafer due to the “bullseye” effect and lifts the completed shafts up away from the substrate and thermally isolating them from the helium cooling system underneath the chuck. Loss of cooling generally causes photoresist to burn of the device and isotropic etching off of the released structure.

Proper mask design in this process could have a profound effect on the above phenomenon. Guard structures could be employed to improve the straightness of the etch and limit the effect of undercutting around the shaft corners. These guard structures would also have the added limiting the exposure of the underlying oxide layer preventing catastrophic release of shaft during etch processing. Finally, these structures could help minimize the local effects of ARDE around the intersection of the cam with the corresponding output or input shaft.

4.4 Engine Assembly

Preliminary engine assembly was performed with the assistance of Suss Microtec and the FC150 flip chip device bonder. Initial samples of spur gear plates, rotors, and epitrochoid housings were used to examine assembly issues. The follow up report on the alignment can be found in Appendix C. There were two difficulties with the spur gear

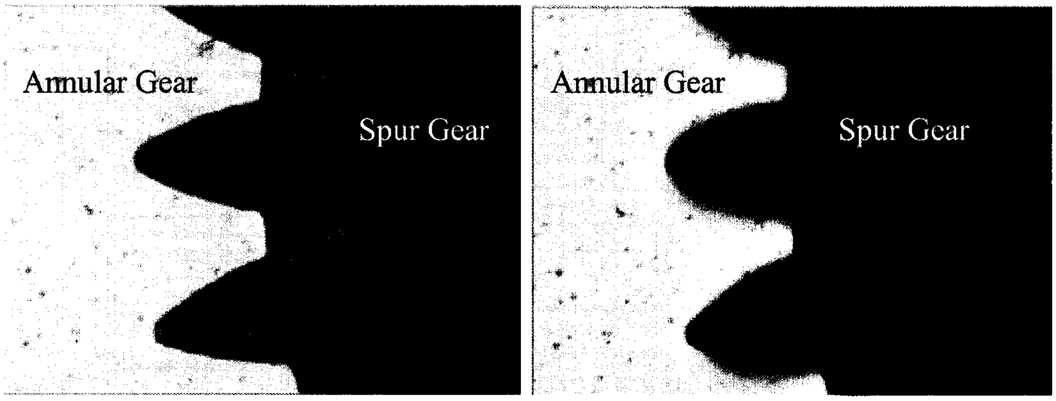

Figure 4-24. Image of the spur gear and annular gear mate during assembly. Left, the gear teeth prior to the mate while the right image shows the teeth mated.

plates used for these assembly tests. First, the alignment verniers used did not have the proper resolution due to poor focus. Instead, the less accurate cross style verniers were used to align the epitrochoid housing to the spur gear plate. Secondly, a small amount of debris was found on the bonding surface of the spur gear plate which prevented a true silicon-silicon bond from being formed. Instead of using a silicon-silicon bond, a thin layer of photoresist 4620 was used in remote spots of the dies as an epoxy.

Pick and place assembly of the rotor within the bonded epitrochoid housing and spur gear plate using the FC150 device bonder showed promising results. Figure 4-24 shows an image the alignment of the spur gear and annular gear teeth during the mating process. Figure 4-24 does not prove that the actual teeth can be mated since the images of the spur and annular gear teeth are superimposed upon one in order to obtain proper alignment. In addition to the alignment of the gear teeth, it is important to note that the rotor must be properly oriented within the epitrochoid as well. That means that in addition to viewing the alignment of the annular and spur gear teeth, the apexes of the

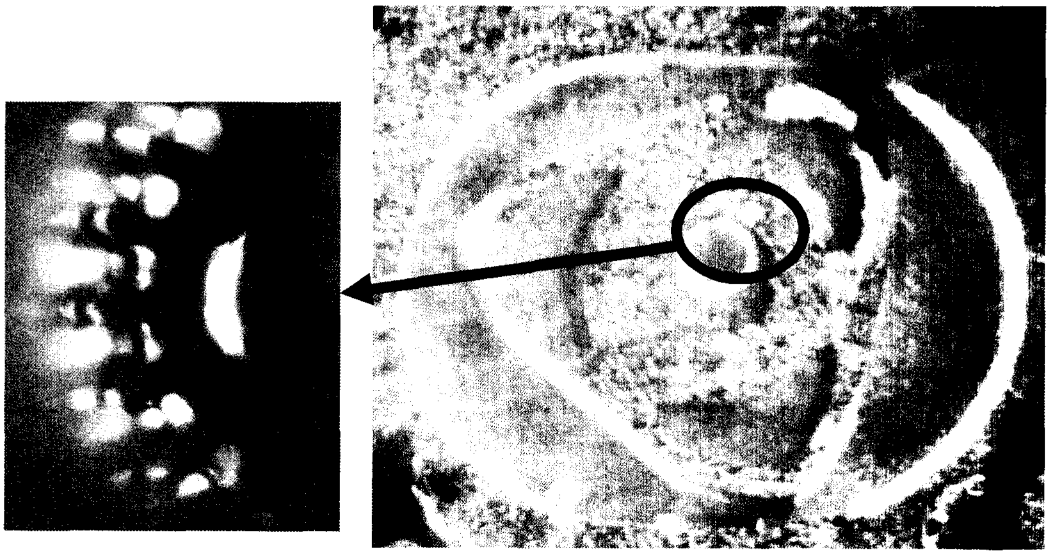

Figure 4-25. Pick and place assembled rotor with highlighted image of the mated spur and annular gear teeth.

rotors must also be viewed in order to align them to the outer wall of the epitrochoid. Figure 4-25 shows an assembled rotor within the mated epitrochoid housing and spur gear plate with a clear top plate. A close-up image in Figure 2-25 shows the mated gear teeth of both the annular and spur gears.

5. Conclusions

This research investigated the design and fabrication of a MEMS-based Wankel internal combustion engine as part of an autonomous, portable power generation system. A comparison of a portable power generation system based on a liquid hydrocarbon fuel to a conventional primary or secondary battery showed a potential for significant advantage in energy density, dependent on the efficiency of the engine and the electrical generator. Additionally, the output of liquid hydrocarbon fueled engine would be tunable and constant. While batteries pose a significant environmental problem in disposal, a MEMS-based combustion engine's emissions compare favorably with a human lung without generating significant NO_X.

An overview of a potential autonomous portable power generation system called MEMS Rotary Engine Power System (MEMS REPS) was presented. The MEMS REPS is based upon a Wankel-type rotary engine fabricated using MEMS fabrication techniques. The overall objective of the 2.4 mm MEMS Wankel engine design is to maximize performance with the greatest degree of manufacturability. Tradeoffs are necessary between different subsystems of the engine in order to achieve the maximum performance. While smaller and/or thinner Wankel engines could be fabricated, an analysis of the electrical generator shows a diminishing return in overall system efficiency (engine efficiency combined with generator efficiency) and generator output as the engine size is scaled down. Similarly, the amount of rotor surface area for soft magnetic pole material is limited by the footprint of the integrated apex tip seals. The subsystem designs presented minimize the amount of energy consumed by ancillary equipment in order to improve the overall power output of the MEMS REPS.

The particular engine design and fabrication process presented separates the 2.4 mm engine into five components: silicon rotor with electrodeposited NiFe material and integrated apex tip seals, epitrochoid housing, spur gear plate, shaft, and top plate. This configuration reduces some of the negative effects of DRIE processing such as beaching which could reduce the accuracy of the final components. Fabrication of a 900 μm thick engine with a combined epitrochoid and spur gear plate would not be possible due to the deleterious effects of beaching, ARDE, and lateral etching due to self masking. Therefore, post-process assembly is a requirement for an engine of this size.

A three mask fabrication process was developed to co-fabricate epitrochoid housings and rotors on the same 900 μm thick wafer. Central to the success of this process is a high pressure Deep Reactive Ion Etch process with high mask selectivity and high etch rate. This etch achieved an oxide selectivity in excess of 350:1 and a photoresist selectivity greater than 150:1. The features generated with this process are 900 μm thick with low sidewall roughness and slightly ballooned sidewall profile. The best sidewall profile achieved a variation of 7-12% of the trench width or 4-26 μm depending on the width of the trench. Generally, smaller trenches gave a more vertical profile. The rotors were fabricated with annular gear teeth accurate to approximately 95% when compared to their designed involute.

Even with a very accurate etch recipe, a 900 μm deep apex seal was not successfully fabricated due to lateral undercutting of the ~30 μm wide in-plane beam. From an analysis of the sidewall profiles of variable width trenches, lateral undercut and non-uniformity of the apex seal can be minimized through proper mask design around the apex seal through the use of guard trenches around the rotor. As trench width is reduced, the amount of lateral undercut due to the bowed profile is also reduced. The width of the guard trenches would be dependent on the selectivity of the process due to the fact that the ARDE effect causes thin trenches to have a slower etch rate. Thinner trenches around the rotor or the epitrochoid will also reduce the difference in etch rate between the outer portion of the rotor and the apex seal trench. A possible solution which would eliminate ARDE of the apex seal would be to implement a backside etch of the apex seal trench. The addition of this step to the overall fabrication process would not significantly affect the tolerance of the rotor outer profile if misaligned. It was observed that in the viscinity of the apex seal tip, extreme undercutting of the apex seal would occur due to its exposure to wide trenches at a variety of different angles. A more advanced mask design will be necessary to reduce undercutting in the area of the apex seal tip.

Spur gear plates were fabricated to form a silicon-silicon prebond to the epitrochoid housing. The frontside of the spur gear plate was defined by a Deep Reactive Ion Etch with a low pressure in order to minimize the surface roughness. This process generated surfaces with a RMS roughness of 4.4 nm which compares favorably with the roughness of a typical polished wafer (4.0 nm). Spur gears with up to 50 teeth were etched in this process. While some erosion at the spur gear tips was observed, spur gear plates with 24 teeth were etched with a 99% degree of accuracy with respect to their involute profile. As spur gear tooth count is increased, the progressively smaller teeth begin to erode at the corners. Beaching, which prevents uneven seating of the rotor within the chamber, was not observed around the teeth of any of the spur gear designs examined. A process for the fabrication of a silicon square shaft is presented. Results indicate local areas of non-uniformity around the corners of the shaft and at the junction between the cam and output shaft. These non-uniformities can be corrected through the use of proper guard structures similar to those of the rotor and epitrochoid housing.

Engine assembly relies upon the smooth surface of the spur gear plate necessary for silicon-silicon prebond and accurate rotor placement within the epitrochoid and with respect to the spur gear teeth. Wafers blanket etched with low pressure DRIE process demonstrated room temperature bonding with polished, unetched wafers. In addition, a set of 8 mm by 8 mm spur gear plate and epitrochoid housing dies were hand aligned and bonded. However, alignment and bonding of spur gear plates to epitrochoid housings through the use of the Suss Microtec FC150 device bonder was not successful. Photoresist micromasking caused 1 μm tall imperfections in the spur gear plate surface. Successful placement of the rotor within the epitrochoid while mating the gear teeth of the rotor to that of the spur gear was achieved.

Fabrication of highly precise and ultra thick silicon structures via Deep Reactive Ion Etching remains a challenging and difficult problem. While integration of the electrical generator and apex sealing within the rotor appears achievable with the processes presented here, further work is necessary to prove successful operation of the components with or without combustion. Nevertheless, this work broadens the upper limit in size for MEMS systems by expanding the width of devices that can be DRIE accurately. This development could potentially open the door for new applications and devices based high aspect ratio, ultra-thick structures fabricated with DRIE.

REFERENCES

Chapter One

[1] "Lithium Batteries," Panasonic, [Online], Available: http://www.actec.dk/Lithium-overview.pdf, 1998.

[2] "Principal Dry Battery Systems and Typical Characteristics," Energizer, [Online], Available: http://data.energizer.com/, 2003.

[3] L. Adams, "Lithium Battery Power Sources for Remote or Portable Sensor Applications," Tadiran Electronic Industries Inc., [Online], Available: http://www.tadiranbat.com/index2.htm, 2003.

[4] S. Oweis, "Lithium-ion Technology for Hybrid ElectricVehicles," presented at Energy Storage Technology for Electric and Hybrid Vehicles: Matching Technology to Design Requirements, Putah Creek Lodge, UC Davis, 1999.

[5] "Energizer No. A91," Eveready Battery Co., [Online], Available: http://data.energizer.com/, 2003.

[6] T. Kanemaru and T. Matsuoka, "General overview of battery waste management in Japan," *Journal of Power Sources*, vol. 57, pp. pp. 23-66, 1995.

[7] G. L. Yender, "Battery recycling technology and collection processes," presented at Proceedings of the 1998 IEEE International Symposium on Electronics and the Environment, New York, NY, USA, 1998.

[8] J. Warnatz, U. Maas, and R. W. Dibble, *Combustion: Physical and Chemical Fundamentals, Modeling and Simulation, Experiments, Pollutant Formation,*, 2nd ed. Berlin: Springer, 1999.

[9] G. J. Tortora, *Introduction to the Human Body*, 2nd ed. New York: Harper Collins Publishers, 1991.

[10] S. Turns, *An Introduction to Combustion: Concepts and Applications*, 2nd ed. Boston: McGraw-Hill, 1996.

[10] K. Fu, A. J. Knobloch, B. Cooley, D. C. Walther, C. Fernandez-Pello, D. Liepmann, and K. Miyaska, "Microscale Combustion Research for Applications to MEMS Rotary IC Engine," presented at 2001 National Heat Transfer Conference, Anaheim, CA, 2001.

[11] A. H. Epstein and e. al., "Micro-Heat Engines, Gas Turbines and Rocket Engines - The MIT Microengine Project," presented at 28th AIAA Fluid Dynamics Conference, 1997.

[12] K. Fu, "Miniature-Scale and Micro-Scale Rotary Internal Combustion Engines for Portable Power Systems," in *Mechanical Engineering*. Berkeley: University of California at Berkeley, 2001.

Chapter Two

[1] "Mazda's 'Renesis' Wins 'International Engine of the Year 2003'," Mazda, Available: http://www.mazda.com/mnl/200306/renesis.html, 2003.

[2] K. Fu, "Miniature-Scale and Micro-Scale Rotary Internal Combustion Engines for Portable Power Systems," in *Mechanical Engineering*. Berkeley: University of California at Berkeley, 2001.

[3] B. Lewis and G. von Elbe, *Combustion, Flames and Explosions of Gases*: Academic Press, 1987.

[4] C. Rossi, E. Scheid, and D. Esteve, "Theoretical and experimental study of silicon micromachined microheater with dielectric stacked membranes," *Sensors & Actuators A-Physical*, vol. A63, pp. 183-9, 1997.

[5] R. Shimizu, H. Okimoto, S. Tashima, and S. Fuse, "The Characteristics of Fuel Consumption and Exhaust Emissions of the Side Exhaust Port Rotary Engine," presented at SAE International Congress and Exposition, Detriot, Michigan, 1995.

[6] S. Turns, *An Introduction to Combustion: Concepts and Applications*, 2nd ed. Boston: McGraw-Hill, 1996.

[7] M. Mehregany, C. A. Zorman, S. Roy, A. J. Fleischman, C. H. Wu, and N. Rajan, "Silicon Carbide for Microelectromechanical Systems," *International Materials Reviews*, vol. 45, pp. pp. 85-108, 2000.

[8] M. B. Wijesundara, D. C. Walther, C. R. Stoldt, K. Fu, D. Gao, C. Carraro, A. P. Pisano, and R. Maboudian, "Low Temperature CVD SiC Coated Si Microcomponents for Reduced Scale Engines," presented at ASME International Mechanical Engineering Congress and Exposition, Washington D.C., 2003.

[9] M. Senesky, Personal Communication, 2002.

[10] J. P. Norbye, *The Wankel Engine: Design, Development, Applications*: Chilton Book Co., 1971.

[11] K. Yamamoto, *Rotary Engine*. Hiroshima, Japan: Toyo Kogyo, 1981.

[12] J. Heppner, D. C. Walther, D. Liepmann, and A. P. Pisano, "Leakage Flow Analysis for a MEMS Rotary Engine," presented at 2003 ASME International Mechanical Engineering Congress and Exposition (IMECE), Washington D.C., 2003.

[13] F. C. Martinez, A. J. Knobloch, and A. P. Pisano, "Apex Seal Design for the MEMS Rotary Engine Power System," presented at 2003 ASME International Mechanical Engineering Congress and Exposition (IMECE), Washington D.C., 2003.

[14] R. M. Bozorth, *Ferromagnetism*. New York: The Institute of Electrical and Electronics Engineers, 1993.

[15] B. Frazier, C. Ahn, and M. G. Allen, "Development of Micromachined Devices using Polyimide-Based Processes," *Sensors and Actuators A*, vol. 45, pp. 47-55, 1994.

[16] J. Judy, "Batch-Fabricated Ferromagnetic Microactuators with Silicon Flexures," in *Electrical Engineering*. Berkeley: University of California at Berkeley, 1996.

[17] S. Leith and D. Schwartz, "High-Rate Through-Mold Electrodeposition of Thick (>200 um) NiFe MEMS Componetns with Uniform Composition," *Journal of Microelectromechanical Systems*, vol. 8, pp. 384-392, 1999.

[18] J. E. Shigley and C. R. Mischke, *Mechanical Engineering Design*, 5th ed. New York: McGraw-Hill, 1989.

[19] K. Pettigrew, J. Kirshberg, K. Yerkes, D. Tebotich, and D. Liepmann, "Performance of a MEMS Based Micro Capillary Pumped Loop for Chip Level Temperature Control," presented at MEMS 2001, Interlaken, Switzerland, 2001.

[20] A. Deshmukh, "Continous Microfluidic Mixing Using Pulsatile Micropumps," in *Mechanical Engineering*. Berkeley: University of California, Berkeley, 2001.

[21] P. Seriburi, D. Kercher, and M. G. Allen, "An Experimental Study of Microfabricated Spark Gaps: Wear and Erosion Characteristics," *Journal of Micromechanics & Microengineering*, vol. 11, pp. 165-174, 2000.

[22] C. Rossi, P. Temple-Boyer, and D. Esteve, "Realization and performance of thin SiO/sub 2//SiN/sub x/ membrane for microheater applications," *Sensors & Actuators A-Physical*, vol. A64, pp. 241-5, 1998.

[23] B. Cooley, "Exploring the Limits of Microscale Combustion," in *Mechanical Engineering*. Berkeley: University of California at Berkeley, 1999.

[24] *Metals Handbook: Volume 1 Properties and Selection: Irons and Steels*, vol. 1. Metals Park: American Society for Metals, 1978.

[25] *2002 SAE Handbook: Volume 1-Metals, Materials, Emmissions, Threads, Fasteners, and Common Parts*, vol. 1: Society of Automotive Engineers, Inc., 2002.

[26] N. Rajan, M. Mehregany, C. A. Zorman, S. Stefanescu, and T. P. Kicher, "Fabrication and Testing of Micromachined Silicon Carbide and Nickel Fuel Atomizers for Gas Turbine Engines," *Journal of Microelectromechanical Systems*, vol. 8, pp. 251-7, 1999.

[27] K. Peterson, “Silicon as a Mechanical Material,” *Proceedings of the IEEE*, vol. 70, no. 5, pp. 420-457, 1982.

Chapter Three

[1] K. Fu, "Miniature-Scale and Micro-Scale Rotary Internal Combustion Engines for Portable Power Systems," in *Mechanical Engineering*. Berkeley: University of California at Berkeley, 2001.

[2] A. Mehra and I. A. Waitz, "Development of a Hydrogen Combustor for a Microfabricated Gas Turbine Engine," presented at 1998 Solid State Sensor and Actuator Workshop, 1998.

Chapter Four

[1] S. Company, "Shipley i-Line Photoresist: Advanced i-Line Materials," Shipley Company, Marlborough, MA AF990014, 1999.

[2] R. B. GmbH, "Patent 4,855,017 and 4,784,720 (USA) and 4241045C1 (Germany)," 1994.

[3] A. A. Ayon, R. Braff, C. C. Lin, H. H. Sawin, and M. A. Schmidt, "Characterization of a Time Multiplexed Inductively Coupled Plasma Etcher," *Journal of the Electrochemical Society*, vol. 146, pp. 339-349, 1999.

[4] M. Wasilik and A. P. Pisano, "Low Frequency Process for Silicon On Insulator Deep Reactive Ion Etching," *SPIE*, vol. 4592, pp. 462-472, 2001.

[5] Q.-Y. Tong and U. Gosele, *Semiconductor Wafer Bonding: Science and Technology*. New York: John Wiley & Sons, Inc., 1999.

[6] T. Abe and J. H. Matlock, "Wafer bonding techniques for Silicon-on-insulator technology," *Solid State Technology*, vol. 39, 1990.

[7] T. Abe and M. Esashi, "One-chip multichannel quartz crystal microbalance (QCM) fabricated by deep RIE," *Elsevier. Sensors & Actuators A-Physical*, vol. A82, pp. pp.139-43, 2000.

[8] C. Marxer, C. Thio, M. A. Gretillat, N. F. de Rooij, R. Battig, O. Anthamatten, B. Valk, and P. Vogel, "Vertical mirrors fabricated by deep reactive ion etching for fiber-optic switching applications," *Journal of Microelectromechanical Systems*, vol. 6, pp. 277-85, 1997.

[9] R. D. Mansano, P. Verdonck, and H. S. Maciel, "Mechanisms of surface roughness induced in silicon by fluorine containing plasmas," *Elsevier. Vacuum*, vol. 48, pp. pp. 677-9, 1997.

[10] K. Fu, "Miniature-Scale and Micro-Scale Rotary Internal Combustion Engines for Portable Power Systems," in *Mechanical Engineering*. Berkeley: University of California at Berkeley, 2001.

Appendix A. Microfabrication Process Flows

A.1 Housing-Rotor Fabrication Procedure

1. Pre-process wafer preparation
    a. 4 inch, 900 μm thick double-polished silicon wafers
    b. Label wafers with appropriate number
    c. Spin dry at Sink 6
2. Mask 1: Wafer and Die level alignment marks
    a. 5 minutes VWR oven 120°C
    b. 5 minutes bubbled HMDS (Sink5)
    c. Spincoat 2 μm thick g-line photoresist (OCG 825) on frontside of wafer (Spin program 4)
    d. 60 second bake at 90°C (Bake program 1)
    e. Expose with Karl Suss 1:1 mask aligner in soft contact mode (I=84mJ/cm2)
    f. Develop wafer with standard g-line develop (OCG 934 2:1, double puddle, 30 sec/puddle), no post-exposure bake
    g. Descum for 1 minute with Oxygen plasma at 50 Watts
    h. Uvbake photoresist, program S
    i. Lam5 HBr/Cl_2 timed silicon etch (150 seconds), program 5003, 1% overetch
    j. Photoresist strip: PRS3000 1-2 hours
3. Low Temperature Oxide Deposition
    a. Pre-oven clean Sink 8

        i. 10 minute piranha dip
        ii. 3 x 2 minute rinse in H_20
        iii. Spindry
    b. Pre-oven clean Sink 6
        i. 10 minute piranha dip
        ii. 3 x 2 minute rinse in H_20
        iii. Spindry
    c. Low Temperature Oxide (LTO) deposition (tystar11 or tystar12)
        i. Run 11sultoa or 12sultoa for 1 hour 30 minutes
        ii. Deposited oxide layer should be 1.5 μm thick (12sultoa) (target thickness=1.2-1.5 μm)

4. Mask 2: Oxide patterning for through wafer features
    a. 5 minutes VWR oven 120°C
    b. 5 minutes bubbled HMDS (Sink5)
    c. Spincoat 2 μm thick g-line photoresist (OCG 825) on frontside of wafer (Spin program 4)
    d. 60 second bake at 90°C (Bake program 1)
    e. Expose with Karl Suss 1:1 mask aligner in soft contact mode (I=84 mJ/cm2)
    f. Develop wafer with standard g-line develop (OCG 934 2:1, double puddle, 30 sec/puddle), no post-exposure bake
    g. Descum for 1 minute with Oxygen plasma at 50 Watts
    h. Uvbake photoresist, program S
    i. Lam2 oxide etch, oxide monitor (recipe p)
        i. Adjust gap to 0.42 cm for 900 μm thick wafers
        ii. 30 sec etch cycles with 90° rotation between cycles
        iii. Visually inspect or measure wafer till oxide completely removed
    j. Photoresist strip: PRS3000 1-2 hours
5. Mask 3: SPR220 pattern for partial thickness features
    a. 5 minutes VWR oven 120°C
    b. 5 minutes bubbled HMDS (Sink5)

- c. Spincoat 10 μm thick SPR220 photoresist on frontside of wafer (Spin program 8 on svgcoat2), no on track bake step performed
- d. Soft Bake for 10 minute at 115°C (Hot plate in Y1 set to 120°C)
- e. Overnight or 6 hour hold time
- f. Expose with Karl Suss 1:1 mask aligner in soft contact mode (I=210 mJ/cm2)
- g. Wait 1 hour
- h. Post-exposure bake for 6.5 min at 115°C (Hot plate in Y1 set to 120°C)
- i. Wait ½ hour for wafer cooling (prevents thermal shock)
- j. Hand develop using LDD-26W for 2.5-3 minutes (if possible visually inspect for completion while developing)
- k. Inspect wafers to determine alignment accuracy
- l. Descum for 1 min in an Oxygen plasma at 50 Watts
- m. 2 hour hard bake in 80°C oven
- n. Measure thick resist with nanospec (SPR220 on 1.3 μm oxide)

6. Handle wafer attachment
   - a. Place oxide encapsulated p-type wafer on 50°C hotplate, rough side up
   - b. Paint on handle wafer surface Cool Grease^{TM} up to 1 mm from the outside edge
   - c. Take wafer off hotplate and bond immediately to backside of device wafer
   - d. Compress for 10 minutes with cooling block
   - e. Bake adhesive for 10 minutes at 70°C
   - f. Check wafer to wafer alignment at flat
7. STS DRIE #1: Through Wafer Features
   - a. Check to be sure that oxide and photoresist thickness are measured with nanospec
   - b. Run COND3 prior to any STS processing (Run prior to any reservation on the STS)
     - i. Heats up chamber
     - ii. Removes contaminate buildup on chamber sidewall
   - c. Load device wafer and run Aaron6C for 15 minutes

   d. Note etch and passivation pressure, HBC, ECU, file name of STS
   e. Measure and record oxide and photoresist thickness with nanospec
   f. Measure and record etch depth with wyko or asiq
   g. Determine etch selectivity and rate
   h. Load and run Aaron6C for a time determined by etch rate for depth such that oxide layer is not breached
   i. Note etch and passivation pressure, HBC, ECU, file name of STS
   j. Measure and record oxide and photoresist thickness with nanospec

8. Oxide Etch Lam2, oxide monitor (recipe p)
   a. Adjust gap to 0.47 cm for 900 μm thick wafers+handle
   b. 20 sec etch cycles with 90° rotation between cycles
   c. Visually inspect or measure oxide thickness between each cycle
9. STS DRIE #2: Drive Down
   a. Load and run Aaron6C for 1 hour increments until etch breakthrough occurs (estimate time to breakthrough from etch rate)
   b. Once breakthrough on the outer edge occurs, run 15 minute intervals until breakthrough is observed over the entire wafer
   c. Note etch and passivation pressure, HBC, ECU, file name of STS
10. Post Process: Release and Clean
   a. Soak in acetone overnight (covered dish) until handle wafer is separated
   b. Remove and discard handle wafer
   c. Clean device wafer and any released components in custom piranha bath for 10 minutes (5:1, Sulfuric Acid:Hydrogen Peroxide)
   d. Rinse thoroughly
   e. Oxide release: 2-3 minute HF dip (concentrated)
   f. Gather components with filter paper and rinse thoroughly

A.2 Spur Gear Plate Fabrication Procedure

1. Pre-process wafer preparation
    a. 4 inch, 400 μm thick double-polished silicon wafers
    b. Label wafers with appropriate number
    c. Spin dry at Sink 6
2. Mask 1: Wafer and Die level alignment marks
    a. 5 minutes VWR oven 120°C
    b. 5 minutes bubbled HMDS (Sink5)
    c. Spincoat 2 μm thick g-line photoresist (OCG 825) on frontside of wafer (Spin program 4)
    d. 60 second bake at 90°C (Bake program 1)
    e. Expose with Karl Suss 1:1 mask aligner in soft contact mode (I=84 mJ/cm2)
    f. Develop wafer with standard g-line develop (OCG 934 2:1, double puddle, 30 sec/puddle), no Post-exposure bake
    g. Descum for 1 minute with Oxygen plasma at 50 Watts
    h. Uvbake photoresist, program S
    i. Lam5 HBr/Cl_2 timed silicon etch (150 seconds), program 5003
    j. Photoresist strip: PRS3000 1-2 hours
3. Mask 2: Backside Ports or Generator Mount
    a. 5 minutes VWR oven 120°C
    b. 5 minutes bubbled HMDS (Sink5)
    c. Spincoat 10 μm thick SPR220 photoresist on frontside of wafer (Spin program 8 on svgcoat2), no on track bake step performed
    d. Soft Bake for 10 minute at 115°C (Hot plate in Y1 set to 120°C)
    e. Overnight or 6 hour hold time
    f. Expose with Karl Suss 1:1 mask aligner in soft contact mode (I=210 mJ/cm2)
    g. Wait 1 hour
    h. Post-exposure bake for 6.5 min at 115°C (Hot plate in Y1 set to 120°C)

i. Wait ½ hour for wafer cooling (prevents thermal shock)
j. Hand develop using LDD-26W for 2.5-3 minutes (if possible visually inspect for completion while developing)
k. Inspect wafers to determine alignment accuracy
l. Descum for 1 min in an Oxygen plasma at 50 Watts
m. 2 hour hard bake in 80°C oven
n. Measure thick resist with nanospec (SPR220 on silicon)

4. STS Backside Etch
    a. Check to be sure that photoresist thickness is measured with nanospec
    b. Run COND3 prior to any STS processing (Run prior to any reservation on the STS)
        i. Heats up chamber
        ii. Removes contaminate buildup on chamber sidewall
    c. Load device wafer and run Aaron1A for 15 minutes
    d. Note etch and passivation pressure, HBC, ECU, file name of STS
    e. Measure and record photoresist thickness with nanospec
    f. Measure and record etch depth with wyko or asiq
    g. Determine etch selectivity and rate
    h. Load and run Aaron1A for a calculated depth of 300 μm (Ports) or 200 mm (Generator Mount-FTIR application)
    g. Note etch and passivation pressure, HBC, ECU, file name of STS
    h. Measure and record photoresist thickness with nanospec
    i. Photoresist strip: PRS3000 1-2 hours
5. Frontside Spur Gear Mask
    a. 5 minutes VWR oven 120°C
    b. 5 minutes bubbled HMDS (Sink5)
    c. Spincoat 2 μm thick g-line photoresist (OCG 825) on frontside of wafer (Spin program 4)
    d. 60 second bake at 90°C (Bake program 1)
    e. Expose with Karl Suss 1:1 mask aligner in soft contact mode (I=80 mJ/cm2)

- f. Develop wafer with standard g-line develop (OCG 934 2:1, double puddle, 30 sec/puddle), no post-exposure bake
- g. Descum for 1 minute with Oxygen plasma at 50 Watts
- h. Uvbake photoresist, program S
- i. Inspect wafer for any remnant photoresist

6. STS Smooth Surface Etch
    - a. Note: handle wafer necessary for porting plate process due to breakthrough
    - b. Check to be sure that photoresist thickness is measured with nanospec
    - c. Run COND3 prior to any STS processing (Run prior to any reservation on the STS)
        - i. Heats up chamber
        - ii. Removes contaminate buildup on chamber sidewall
    - d. Load device wafer and run Aaron1B for 30 minutes
    - e. Note etch and passivation pressure, HBC, ECU, file name of STS
    - f. Measure and record photoresist thickness with nanospec
    - g. Measure and record etch depth with wyko or asiq
    - h. Determine etch selectivity and rate
    - i. Load and run Aaron1B until wafer breakthrough (Ports) or for 100 μm (Generator Mount)
    - j. Note etch and passivation pressure, HBC, ECU, file name of STS
    - k. Measure and record photoresist thickness with nanospec
    - j. Photoresist strip: Acetone dish/covered
7. Photoresist spin on DRIE features/Die Scale Alignment
    - a. 5 minutes VWR oven 120°C
    - b. 5 minutes bubbled HMDS (Sink5)
    - c. Manually spin I-line resist on wafer
        - i. Using eyedropper, coat frontside recess entirely with photoresist
        - ii. 5 sec @ 500 RPM Acceleration 5,000
        - iii. 30 sec @ 2000 RPM Acceleration 10,000 (Spinner2-program 5)
        - iv. 60 sec Soft Bake on 90°C (hot plate in Y1 set for 95°C)

   - d. Measured thickness of this photoresist using nanospec (1.74 μm±225 Ang)
   - e. Expose with Karl Suss 1:1 mask aligner in soft contact mode (I=120mJ/cm2)
   - f. SVGDEV program 1, no post exposure bake
   - g. Descum for 1 minute with Oxygen plasma at 50 Watts
   - h. 30 minute hard bake in VWR 120°C
   - i. Lam5 HBr/Cl_2 timed silicon etch (30 seconds), program 5003, 10% overetch
   - j. No photoresist strip

8. Device preparation and dicing
   - a. Dicing protection
     - i. Spincoat 1.1 μm I-line photoresist (svgcoat program 1) on front of wafer
     - ii. 60 second bake at 90°C (Bake program 1)
     - iii. Inspect to be sure gears are protected with photoresist
   - b. Mount wafer on dicing tape upside down (gears toward tape to prevent slivers or imperfections on the bonding surface at the die's edge)
   - c. Cut wafer using backside features as a guide, do not cut through the wafer thickness but leave 50 μm so that the pieces can be broken apart down the dicing paths
   - d. Remove dies from dicing tape using a Teflon tweezer
   - e. Use an acetone bath to remove photoresist
9. Pre-bond preparation (spur gear plates and epitrochoid housings)
   - a. Clean dies for 10 minutes using a custom piranha bath (5:1, Sulfuric Acid:Hydrogen peroxide)
   - b. Segregate the dies from one another so that they do not touch or scratch which may mean cleaning only 2-4 dies at any one time, Teflon tweezers can be used during cleaning to keep the dies separate
   - c. Rinse thoroughly and dry with air gun

A.3 Square Shaft Fabrication Procedure

1. Pre-process wafer preparation
    a. 4 inch, 523 μm±1 μm thick double-polished silicon wafers
    b. Label wafers with appropriate number
    c. Spin dry at Sink 6
2. Mask 1: Wafer and Die level alignment marks
    a. 5 minutes VWR oven 120°C
    b. 5 minutes bubbled HMDS (Sink5)
    c. Spincoat 2 μm thick g-line photoresist (OCG 825) on frontside of wafer (Spin program 4)
    d. 60 second bake at 90°C (Bake program 1)
    e. Expose with Karl Suss 1:1 mask aligner in soft contact mode (I=84 mJ/cm2)
    f. Develop wafer with standard g-line develop (OCG 934 2:1, double puddle, 30 sec/puddle), no Post-exposure bake
    g. Descum for 1 minute with Oxygen plasma at 50 Watts
    h. Uvbake photoresist, program S
    i. Lam5 HBr/Cl_2 timed silicon etch (150 seconds), program 5003, 1% overetch
    j. Photoresist strip: PRS3000 1-2 hours
3. Low Temperature Oxide Deposition
    a. Pre-oven clean Sink 8
        i. 10 minute piranha dip
        ii. 3 x 2 minute rinse in H_20
        iii. Spindry
    b. Pre-oven clean Sink 6
        i. 10 minute piranha dip
        ii. 3 x 2 minute rinse in H_20
        iii. Spindry

   c. Low Temperature Oxide (LTO) deposition (tystar11 or tystar12)
      i. Run 11sultoa or 12sultoa for 1 hour 30 minutes
      ii. Deposited oxide layer should be 1.5 μm thick (12sultoa) (target thickness=1.2-1.5 μm)

4. Mask 2: Oxide patterning for through wafer features
   a. 5 minutes VWR oven 120°C
   b. 5 minutes bubbled HMDS (Sink5)
   c. Spincoat 2 μm thick g-line photoresist (OCG 825) on frontside of wafer (Spin program 4)
   d. 60 second bake at 90°C (Bake program 1)
   e. Expose with Karl Suss 1:1 mask aligner in soft contact mode (I=120 mJ/cm2)
   f. Develop wafer with standard g-line develop (OCG 934 2:1, double puddle, 30 sec/puddle), no post-exposure bake
   g. Descum for 1 minute with Oxygen plasma at 50 Watts
   h. Uvbake photoresist, program S
   i. Lam2 oxide etch, oxide monitor (recipe p)
      i. Keep standard gap (0.38 cm)
      ii. 30 sec etch cycles with 90° rotation between cycles
      iii. Measure or visually inspect wafers till completion
   j. Photoresist strip: PRS3000 1-2 hours
5. Mask 3: SPR220 pattern for partial thickness features
   a. 5 minutes VWR oven 120°C
   b. 5 minutes bubbled HMDS (Sink5)
   c. Spincoat 10 μm thick SPR220 photoresist on frontside of wafer (Spin program 8 on svgcoat2), no on track bake step performed
   d. Soft Bake for 10 minute at 115°C (Hot plate in Y1 set to 120°C)
   e. Overnight or 6 hour hold time
   f. Expose with Karl Suss 1:1 mask aligner in soft contact mode (I=220 mJ/cm2)
   g. Wait 1 hour

    h. Post-exposure bake for 6.5 min at 115°C (Hot plate in Y1 set to 120°C)
    i. Wait ½ hour for wafer cooling (prevents thermal shock)
    j. Hand develop using LDD-26W for 2.5-3 minutes (if possible visually inspect for completion while developing)
    k. Inspect wafers to determine alignment accuracy
    l. Descum for 1 min in an Oxygen plasma at 50 Watts
    m. 2 hour hard bake in 80°C oven
    n. Measure thick resist with nanospec (SPR220 on 1.3 μm oxide)

6. Handle wafer attachment
    a. Place oxide encapsulated p-type wafer on 50°C hotplate, rough side up
    b. Paint on handle wafer surface Cool Grease™ up to 1 mm from the outside edge
    c. Take wafer off hotplate and bond immediately to backside of device wafer
    d. Compress for 10 minutes with cooling block
    e. Bake adhesive for 10 minutes at 70°C
    f. Check wafer to wafer alignment at flat
7. STS DRIE #1: Through Wafer Features
    a. Check to be sure that oxide and photoresist thickness are measured with nanospec
    b. Run COND3 prior to any STS processing (Run prior to any reservation on the STS)
        i. Heats up chamber
        ii. Removes contaminate buildup on chamber sidewall
    c. Load device wafer and run Shaft1A for 15 minutes
    d. Note etch and passivation pressure, HBC, ECU, file name of STS
    e. Measure and record oxide and photoresist thickness with nanospec
    f. Measure and record etch depth with wyko or asiq
    g. Determine etch selectivity and rate
    h. Load and run Shaft1A for a time determined by etch rate for depth such that oxide layer is not breached
    i. Note etch and passivation pressure, HBC, ECU, file name of STS

   j. Measure and record oxide and photoresist thickness with nanospec

8. Oxide Etch Lam2, oxide monitor (recipe p)
   a. Adjust gap to 0.43 cm for 500 μm thick (wafer + handle)
   b. 20 sec etch cycles with 90° rotation between cycles
   c. Visually inspect or measure oxide thickness between each cycle
9. STS DRIE #2: Drive Down
   a. Load and run Shaft1A for 1 hour increments until etch breakthrough occurs (estimate time to breakthrough from etch rate)
   b. Once breakthrough on the outer edge occurs, run 15 minute intervals till breakthrough is observed over the entire wafer
   c. Note etch and passivation pressure, HBC, ECU, file name of STS
10. Post Process: Release and Clean
   a. Soak in acetone overnight (covered dish) until handle wafer is separated
   b. Remove and discard handle wafer
   c. Clean device wafer and any released components in custom piranha bath for 10 minutes (5:1, Sulfuric Acid:Hydrogen Peroxide)
   d. Rinse thoroughly
   e. Oxide release: 2-3 minute HF dip (concentrated)
   f. Gather components with filter paper and rinse thoroughly

Appendix B. SPR220 Design of Experiments

Raw Data collected as part of determining the proper bake and exposure times for SPR220.

Soft Bake Temperature (degC)	Soft Bake Time (min)	Exposure Time (sec)	Post-Exposure Bake Temperature (degC)	Post-Exposure Bake Time (min)	Differential (um)
115	7.5	13	115	10	5.5
115	7.5	13	115	5	3.3
120	10	8	110	10	5.5
120	10	8	120	5	4
110	10	18	120	5	5
120	5	18	110	10	6
110	5	18	110	5	7
120	5	18	120	5	5.5
120	5	8	110	5	6
115	10	13	115	7.5	9
120	10	18	110	5	7
115	7.5	13	115	7.5	5
110	10	8	110	5	6.5
115	7.5	13	115	7.5	5
110	7.5	13	115	7.5	6
110	10	8	120	10	9
115	7.5	13	120	7.5	6
115	7.5	13	115	7.5	6
115	7.5	13	115	7.5	4.5
110	5	18	120	10	3
115	7.5	13	115	7.5	5
115	5	13	115	7.5	5
120	5	8	120	10	8.5
115	7.5	13	110	7.5	6.5
115	7.5	8	115	7.5	9
120	7.5	13	115	7.5	4.5
110	10	18	110	10	3
110	5	8	120	5	7.5
115	7.5	18	115	7.5	5
110	5	8	110	10	8
115	7.5	13	115	7.5	8
120	10	18	120	10	20

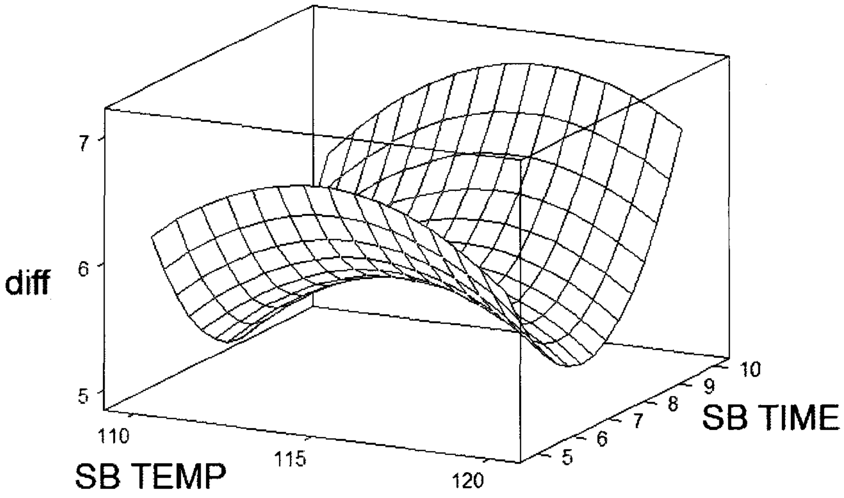

Hold values: EXP TIME: 13.0 PEB TEMP: 115.0 PEB TIME: 7.5

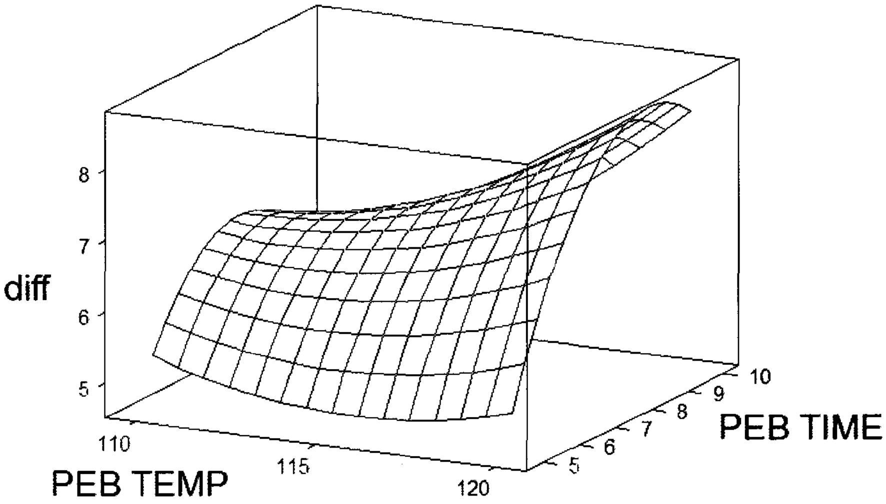

Hold values: SB TEMP: 115.0 SB TIME: 10.0 EXP TIME: 13.0

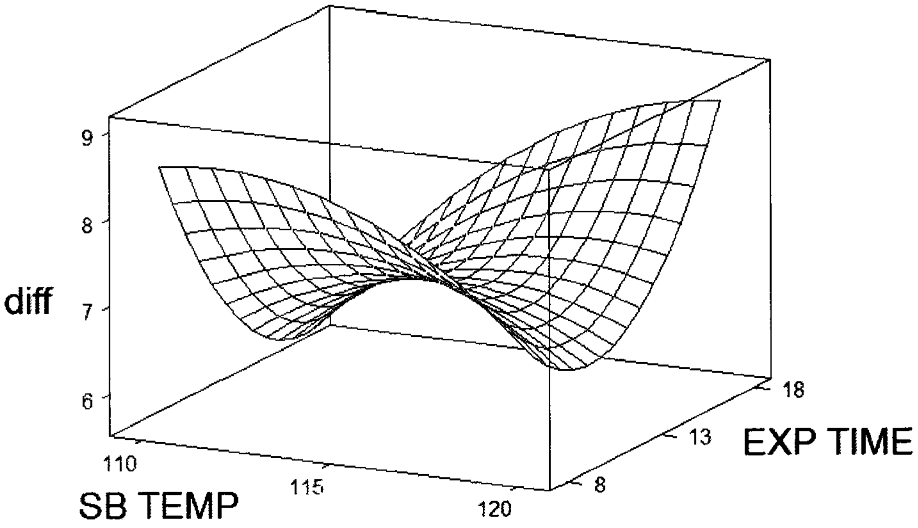

Hold values: SB TIME: 10.0 PEB TEMP: 115.0 PEB TIME: 7.5

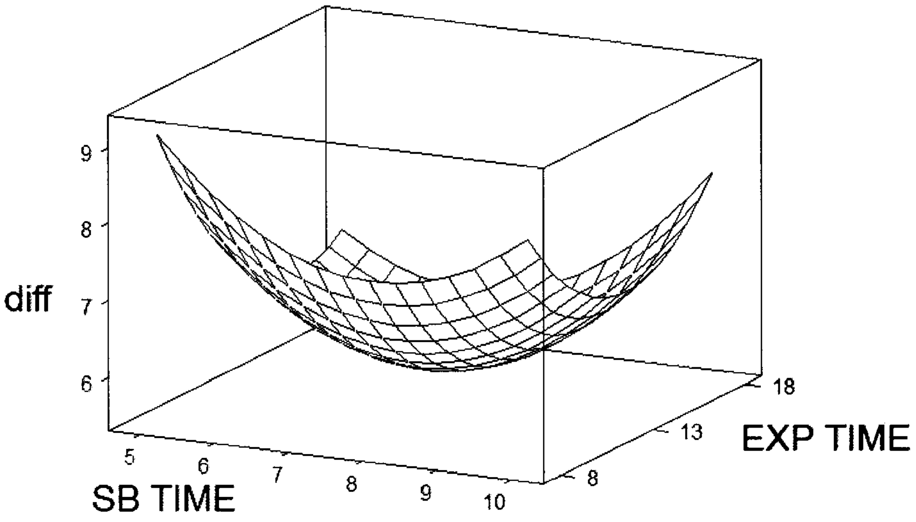

Hold values: SB TEMP: 115.0 PEB TEMP: 115.0 PEB TIME: 7.5

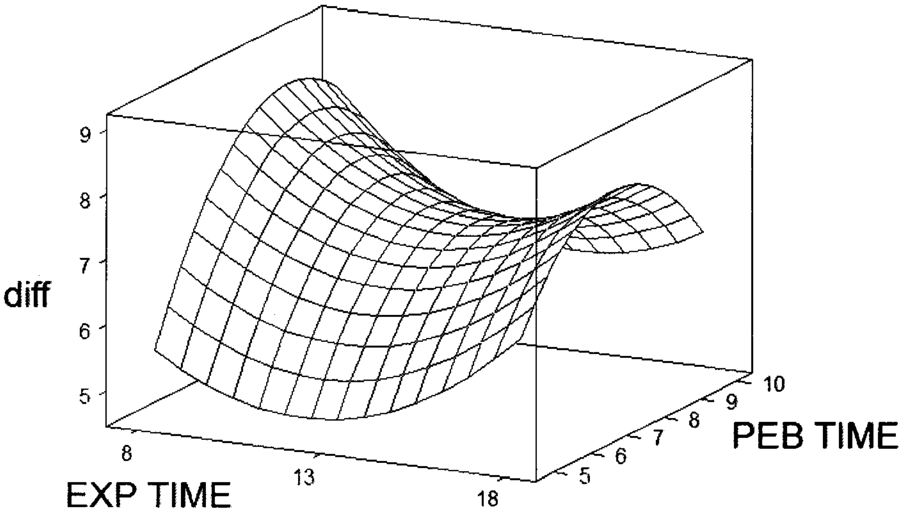

Hold values: SB TEMP: 115.0 SB TIME: 10.0 PEB TEMP: 115.0

Appendix C. Suss Microtec Notes on Assembly

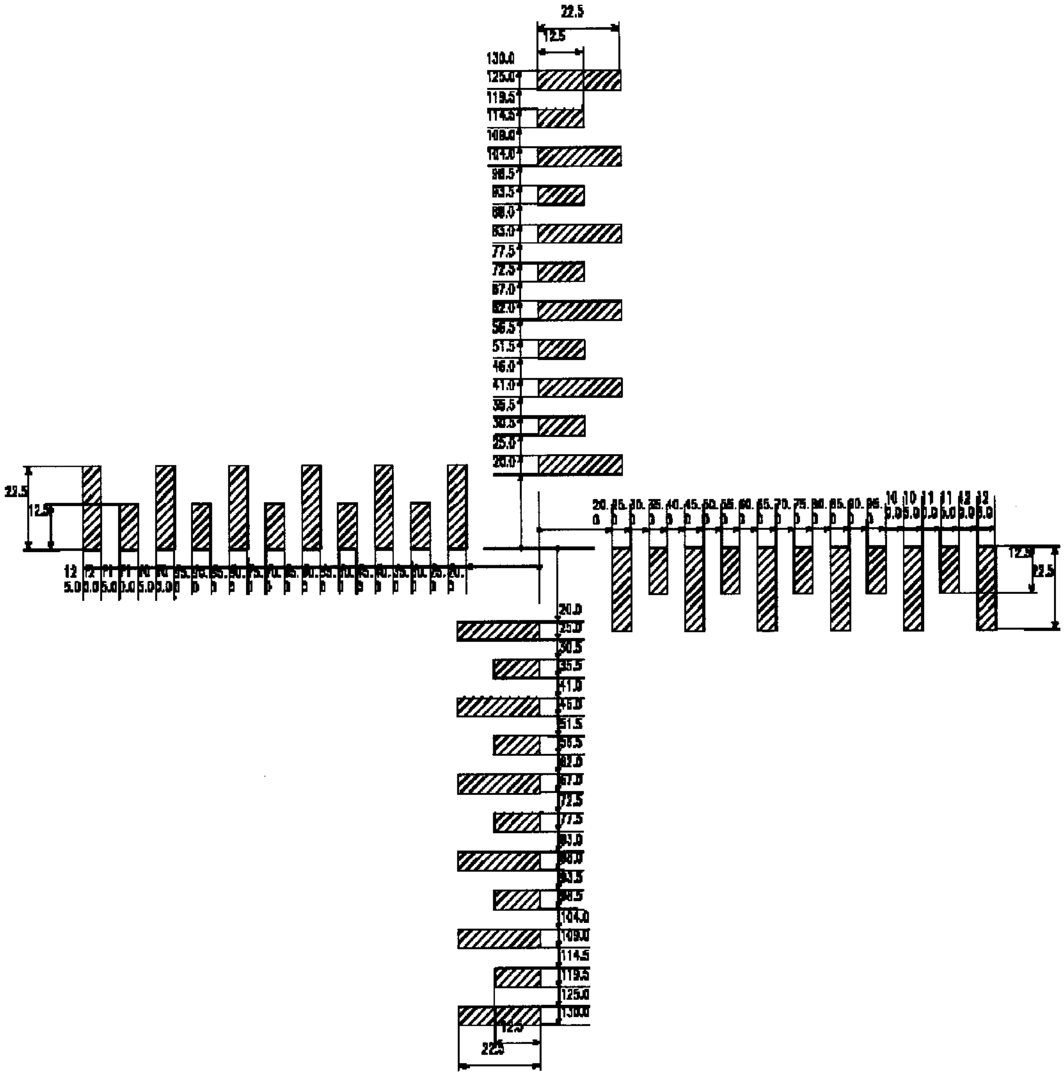

Drawing of vernier scales for die to die alignment. Corresponding verniers should be rotated 90 degrees.

Recommended Alignment Marks for FC150

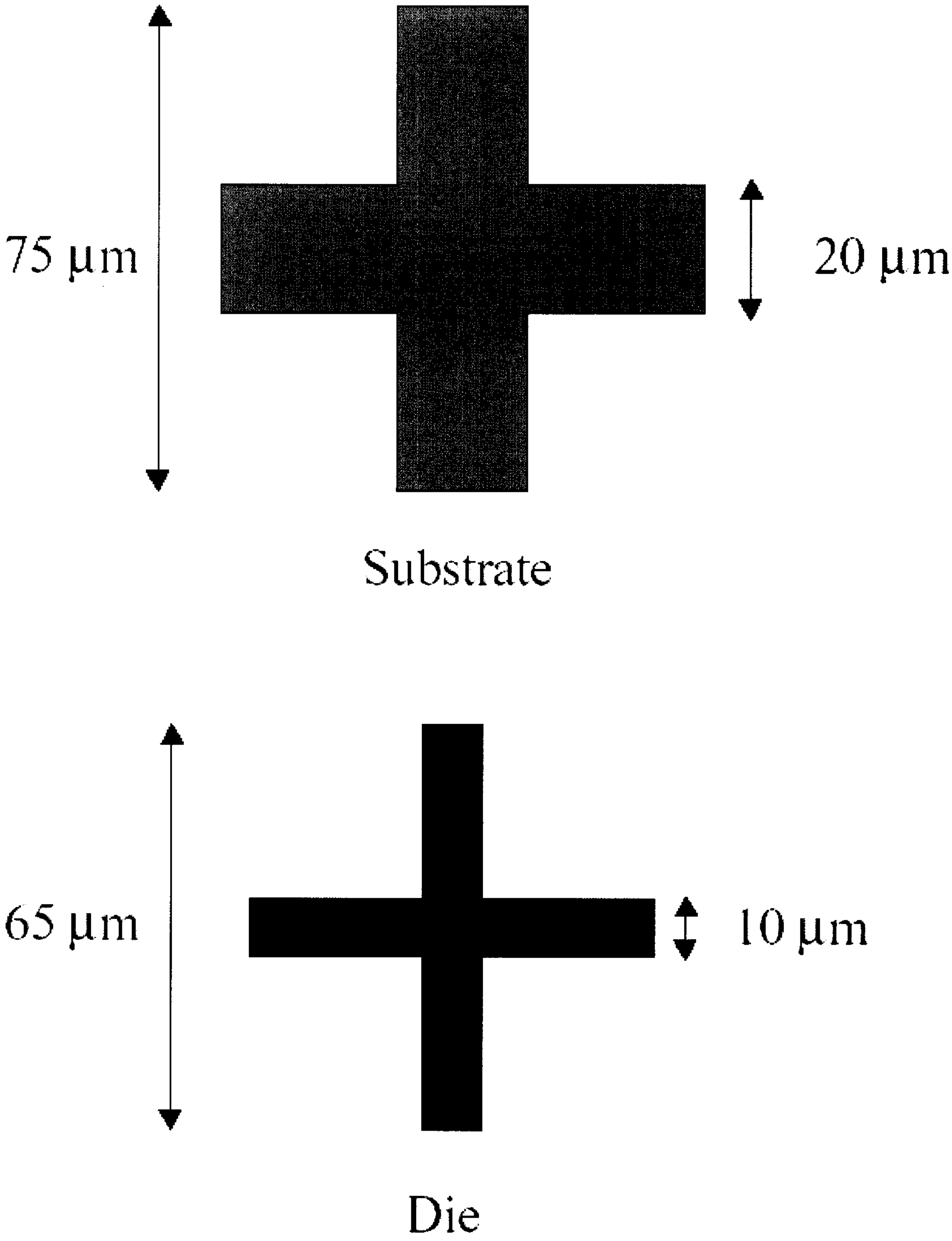

Course alignment marks used for die-to-die alignment in the FC150 flip chip bonder.

Appendix D. DRIE Recipes and Data

Recipe Name	APC Angle	Cycle Time	Cycle Time	Cycle	SF6 Flow	O2 Flow	C4F8 Flow
		Pass (sec)	Etch (sec)	Ratio	(sccm)	(sccm)	(sccm)
Aaron6C	77	7.2(0.5)	12 (0.5)	1.67	90	8	52
Aaron6B	76	6.6 (0.5)	11 (0.5)	1.52	90	8	52
Aaron6A	77	6 (0.5)	10 (0.5)	1.67	90	8	52
Aaron7A	73	6 (0.5)	10 (0.5)	1.67	90	8	52
Aaron8A	68	6 (0.5)	10 (0.5)	1.67	90	8	52
HEXA100	66	7 (0.5)	9 (0.5)	1.29	130	13	85

Recipe Name	Coil Power	Platen Power (W)		Pressure (mT)	Pressure (mT)
	(Watts)	Etch	Pass	Etch	Passivation
Aaron6C	600	10	5	44	24
Aaron6B	600	10	5	40	22
Aaron6A	600	12	5	43	23
Aaron7A	600	12	5	34	18
Aaron8A	600	12	5	25	13
HEXA100	600	12	0	[redacted]	[redacted]

	Min	Max	Average	
Recipe Name	Etch Rate	Etch Rate	Etch Rate	Grass
	um/min	um/min	um/min	(Y/N)
Aaron6C	1.75	2.42	2.09	Y
Aaron6B	2.09	2.78	2.43	Y
Aaron6A	2.57	3.39	2.98	Y
Aaron7A	2.84	3.37	3.10	N
Aaron8A	3.10	3.40	3.25	N

	Min	Max	Min	Max
Recipe Name	Oxide	Oxide	PR	PR
	Selectivity	Selectivity	Selectivity	Selectivity
Aaron6C	308.82	426.47	105.00	145.00
Aaron6B	259.71	345.60	106.72	142.02
Aaron6A	342.51	422.02	162.18	214.51
Aaron7A	243.75	289.84	85.01	101.09
Aaron8A	240.93	264.25	85.71	94.01